

DYNAMICS OF DRIVEN DISSIPATIVE HEISENBERG SPINS WITH INERTIA

Thesis submitted in

Partial Fulfilment of the

Degree of Doctor of Philosophy (Ph.D.)

by

Jayajit Das

Institute of Mathematical Sciences

Madras

UNIVERSITY OF MADRAS

MADRAS 600 005

OCTOBER 2000

DECLARATION

I declare that the thesis entitled "Dynamics of Driven Dissipative Heisenberg Spins with Inertia" submitted by me for the Degree of Doctor of Philosophy is the record of work carried out by me during the period from November 1996 to September 2000 under the guidance of Prof. M. V. N. Murthy and has not formed the basis for the award of any degree, diploma, associateship, fellowship, titles in this or any other University or other similar Institution of Higher Learning.

(Jayajit Das)

CERTIFICATE FROM THE SUPERVISOR

I certify that the thesis entitled "Dynamics of Driven Dissipative Heisenberg Spins with Inertia" submitted for the Degree of Doctor of Philosophy by Mr. Jayajit Das is the record of research work carried out by him during the period from November 1996 to September 2000 under my guidance and supervision, and that this work has not formed the basis for the award of any degree, diploma, associateship, fellowship or other titles in this University or any other University or Institution of Higher Learning.



7.10.2000

(M. V. N. Murthy)

Professor, Theoretical Physics.
Institute of Mathematical Sciences.

Acknowledgments

to my parents

First and foremost I want to thank my parents for their love and support throughout my life. Without their encouragement and belief in me, I would not have been able to pursue my dreams.

I am grateful to my mother for her unconditional love and support. Her belief in me has been a constant source of strength and motivation. I am also grateful to my father for his wisdom and guidance.

Thanks to Y. Harada for his helpful comments and suggestions. I am indebted to him for his advice and support. I also thank my friends for their encouragement and support.

Discussing my work with my friends and colleagues has been a great help. I am grateful to them for their advice and support. I am also grateful to my friends for their love and support.

Reading physics and mathematics books has been a great help. I am grateful to the authors for their advice and support. I am also grateful to my friends for their love and support.

Physics and mathematics are my favorite subjects. I am grateful to my teachers for their advice and support. I am also grateful to my friends for their love and support.

I had a very nice time during my stay in Japan. I am grateful to my hosts for their advice and support. I am also grateful to my friends for their love and support.

It is a pleasure to acknowledge the help and support of my friends and colleagues. I am grateful to them for their advice and support. I am also grateful to my friends for their love and support.

Acknowledgements

First and foremost I would like to thank Madan. Working with him had been great fun. Innumerable discussions with him taught me to ask the right questions, to understand the problems in simple but insightful ways and to be critical about the work. I am grateful to him for his encouragement, patience and generosity.

I am grateful to Prof. M.V. N. Murthy for his advice, help and kindness. I owe a lot to him for being able to complete my thesis without any hassle.

Thanks to Y. Hatwalne for many interesting discussions on physics, which helped me to clear many doubts. I am indebted to him for a very careful reading of the manuscript and his suggestions in preparing the thesis.

I should thank Sriram for the stimulating discussions I had with him for the work on Driven Heisenberg magnets.

Discussing my work with Abhishek, especially on the problem of heat conduction has benefitted substantially my understanding of the problem. I thank him for his prompt and critical reading of some portions of my thesis.

Talking physics and my work with Sarasij has always been delightful. His apparently simple questions helped significantly in making my conceptions clear. I am grateful to Sunil for the discussions I had with him. Also for his suggestions and advice on various matters (physics and non-physics) at different stages of my research work. I thank Surajit Sengupta for teaching me various tricks of the trade in numerics.

I had a very nice time at RRI. I sincerely thank everyone for their kind help, generosity and for providing an excellent atmosphere for research. Thanks to G. Manjunath and K. Raju for their help in various official matters.

It is a pleasure to acknowledge the help and enjoyable discussions I had with the students

and faculties of IMSc. Murugesh and Pushan deserve special thanks for helping me out in various critical situations. I sincerely thank Usha Devi, Shankar, Ahmed and other official staff members in IMSc for their help in various official matters. I thank IMSc for providing excellent facilities and an atmosphere congenial to research work.

I owe a lot for getting into physics research to Prof. Shaymal Sengupta, and the Presidency College Seminar Group (1991 batch and seniors). The long discussions in the corridors, classrooms and the portico during that period still remain as a source of inspiration.

And thanks to everyone I have interacted academically or non-academically in my Ph.D years – I always learnt something new from them.

I am grateful to my parents and raka for their constant support and encouragement.

Lastly, thanks to the lovely city of Bangalore where you can never be bored.

Contents

1	Introduction	2
1.1	Phase Ordering Kinetics of Heisenberg magnets	8
1.2	Dissipative Dynamics of Driven Heisenberg magnets	14
1.3	Dynamics of Heisenberg magnets in the presence of a Temperature gradient .	17
1.4	Note on Format	19
2	Dynamics of Ordering in Heisenberg magnets	23
2.1	Dynamics at $T = 0$	24
2.1.1	Langevin Simulation	26
2.1.2	Perturbation about $g \neq 0$ fixed point: The Pure Torque Model	42
2.1.3	Perturbation about $g = 0$: The Gaussian Closure Scheme	48
2.2	Dynamics at $T = T_c$	63
2.3	Conclusions and Future Work	68
2.4	Appendix IIA	70
2.5	Appendix IIB	72
2.6	Appendix IIC	76
3	Dissipative Dynamics of Driven Heisenberg magnets	87
3.1	Derivation of the Dynamical Equations	87
3.2	Dynamics at High Drive-Temperatures, $v > 0$	92
3.3	Dynamics in the Critical Phase, $v = 0$	92
3.4	Dynamics at Low Drive-Temperatures, $v < 0$	100
3.5	Conclusions and Future Work	111

3.6	Appendix IIIA	112
3.7	Appendix IIIB	120
4	Dynamics of Heisenberg magnets driven by a Temperature gradient	124
4.1	Model of Heat Conduction	124
4.2	Conserved Dynamics, $\vec{\mu}_1 = \vec{\mu}_2$	128
4.2.1	Dynamics in one dimension	129
4.3	Conclusions and Future Work	135
4.4	Appendix IVA	137

Chapter 1

Introduction

A many-body system (with say 10^{23} particles) which is closed and ergodic will, given sufficient time, reach a unique equilibrium configuration. The approach to such an equilibrium configuration is by and large fairly well understood [1, 2, 3]. However the vast majority of systems observed in nature are *open* and subject to external forces which *drive* it far from equilibrium. Being dissipative such systems evolve over long times to settle into complex steady state behaviours. A variety of phenomena in Atmospheric Sciences (cyclonic patterns [4]), Geology (glaciation, mountain ranges [5], river networks [6]) and Biology (pattern formation in embryonic cells, morphogenesis of cellular structures [7]) constitute examples of such behaviour (Fig. 1.1). The classification of generic behaviour exhibited by such systems is currently a subject of intense research and very far from complete.

An important step in the classification program was the construction of the simplest possible dynamical model, the 'hydrogen atom' of many-body interacting systems, which is both driven and diffusive — the so called Driven Diffusive Lattice Gas (DDLG) models [8]. Several studies, using a variety of theoretical techniques like numerical simulations, mean field approximations and dynamical renormalisation group, have been devoted to understanding its 'dynamical phase diagram' under different external conditions.

The DDLG models studied so far are purely diffusive and driven and do not possess any inertia. Most systems of N particles however obey, in the absence of dissipation and external driving, a dynamics which is inertial, *i.e.*, they are governed by Newton's laws. Inertial dynamics of course conserves energy, as opposed to dissipative dynamics (which results in energy loss) and external driving (which results in energy gain). This thesis is a

study of the interplay between inertia, dissipation and driving on the dynamics of many-body systems in d -dimensions.



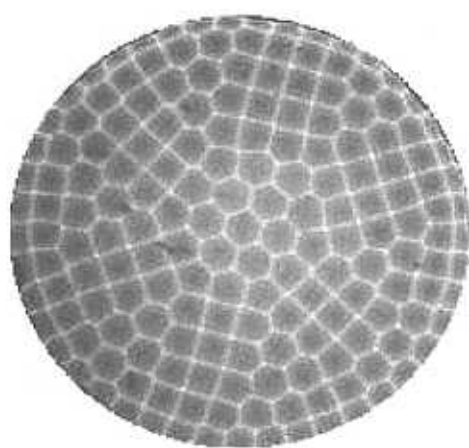
(a)



(b)



(c)



(d)

Figure 1.1: Examples of driven, dissipative systems with inertia. (a) Hurricane 'Bonnie' photographed over the western Atlantic from a space shuttle (courtesy: <http://www-paoc.mit.edu/~emanuel/geosys/node1.html>). (b) Himalayas mountain range viewed from the top of Mt. Everest. (c) Trails of a meandering river in the flood plain in Alaska (courtesy: <http://www.geology.uiuc.edu/~hsui/classes/geo116/lectures/wk4folder/WaterActn.html>). (d) Pattern formation in surface tension driven Benard convection (courtesy: <http://chaos.ph.utexas.edu/research/schatz/home.html>).

Let us start with a text book example of a driven, dissipative single particle system [9]. Consider a particle in a potential $V(x) = \frac{1}{2}r x^2 + \frac{1}{4}u x^4$, where r can have arbitrary sign and

$u > 0$ (Fig. (1.2)).

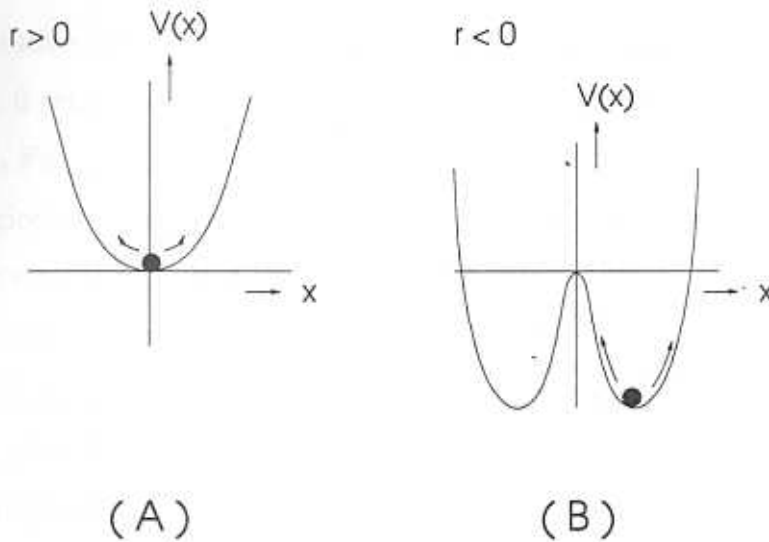


Figure 1.2: Particle in a potential $V(x)$.

The dynamics, given by Newton's equation $\ddot{x} = -V'(x) = -rx - ux^3$, conserves energy (*inertial dynamics*). The 'phase-trajectory' $(x(t), v(t) \equiv \dot{x}(t))$ is an ellipse signifying periodic motion with constant amplitude, Fig. (1.3a). Introducing dissipation in the form of a frictional force $-\zeta\dot{x}$, will dampen the particle motion leading to a loss in energy (*inertia + dissipation*). The oscillations have a decaying amplitude, Fig.(1.3b), and eventually the particle will cease to move. We now drive the system with a periodic external force $A \cos(\omega t)$, thus $\ddot{x} + \zeta\dot{x} + rx + ux^3 = A \cos(\omega t)$. The equations of motion may be rewritten as three autonomous equations

$$\begin{aligned}\dot{x} &= v, \\ \dot{v} &= -\zeta v - rx - ux^3 + A \cos \Omega, \\ \dot{\Omega} &= \omega,\end{aligned}\tag{1.1}$$

making it convenient to analyse the $(x(t), v(t))$ 'phase-portraits' of this 3-dimensional dynamical system. For $r > 0$ and small $x(t) < 1$ (harmonic), the external driving dominates after a short transient, and the particle oscillates with frequency ω and an amplitude given by A , Fig. (1.3c). When $x(t) > 1$ (anharmonic), the particle still oscillates with a frequency

ω but with an amplitude which depends on the initial conditions, Fig. (1.3d). When $r = 0$, the nature of the phase-portrait changes significantly. For a certain range of ζ and A values, the time evolution becomes aperiodic and *chaotic*, Fig. (1.3e). This chaotic dynamics persists when $r < 0$ (provided $x > 1$ so that it hops to the other well) for a special range of values of ζ and A , Fig. (1.3f) [10]. Note that in this chaotic regime, the trajectories densely fill a bounded region in phase space. We introduce an additional diagnostic of chaos, one which is more convenient to portray for the many-particle systems we shall encounter later than these phase space plots. In the chaotic regime, the power spectrum computed from the time series $x(t)$, i.e., $P(\omega) = |\hat{x}(\omega)|^2$, should decay as a power law or remain constant. Figure (1.3g) is a plot of $P(\omega)$ for the single-particle example, showing that it is roughly a constant (the fit improves with better data). This chaos may be ‘controlled’ by applying a perturbation which prevents x from becoming large [11]. If the motion is restricted to small x (so as to neglect the x^3 term in Eq. (1.1)), the chaotic motion ceases resulting in the usual forced oscillations, Fig. (1.3h). Thus we see that the interplay between inertia, dissipation and driving leads to a rich ‘phase diagram’ even in this simple 1-particle system.

Leaving this driven single particle system behind, we ask for examples of many-body systems where the joint action of inertia, dissipation and driving can lead to complex behaviours. There have been several beautiful studies of such systems which include complex fluids (e.g., liquid crystals, polymers and surfactant aggregates) subject to constant shear rates, driven interfaces (flux-lines in super-conductors and domain walls in magnets), and Rayleigh-Benard convection of fluids sandwiched between two plates held at different temperatures. In the spirit of DDLG models, we search for the simplest model many-body system which exhibits these three features. It is clear that Ising-like systems do not satisfy these requirements, since their dynamics is purely dissipative (being generated by contact with a heat bath). The simplest example of a many-body spin system possessing inertial dynamics is the Heisenberg model in which the spins precess in response to the local magnetic field.

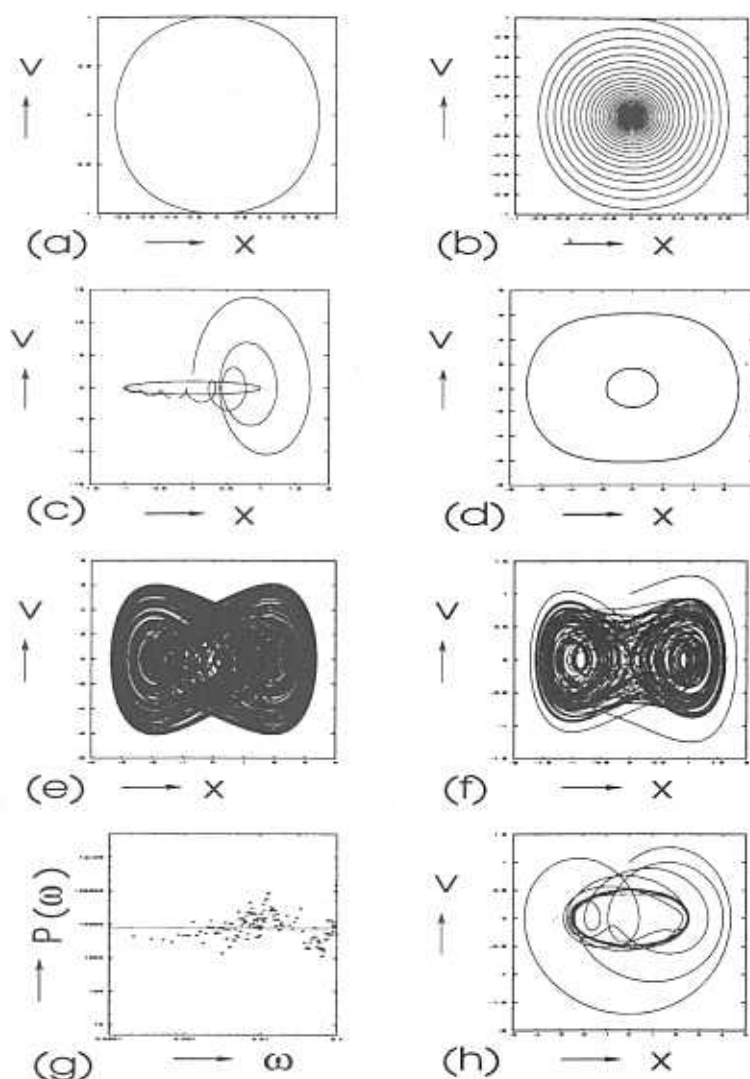


Figure 1.3: Plots of $v \equiv \dot{x}$ vs x . (a) Inertial dynamics without dissipation ($\zeta = 0$) and driving ($A = 0$) for $r = 1$ and $u = 1$. (b) Introduction of dissipation ($\zeta = 0.04$) slows down the particle which eventually ceases to move. (c) Particle is driven with a periodic force ($A = 256$ and $\omega = 1$) and the motion is restricted to small amplitudes ($u = 0$). Here $r = 256$ and $\zeta = 3.2$. (d) Large amplitude ($u = 0.01953$) motions are allowed and after the transient dies down, the particle chooses one of the two amplitudes depending on the initial condition. Plot is for $r = 0.3906$, $\zeta = 0.125$, $\omega = 1$ and $A = 1.024$. (e) At the *critical point* ($r = 0$), chaotic motion arises when, $u = 1$, $\zeta = 0.05$, $\omega = 1$ and $A = 7.5$. (f) Chaos persists for negative values of r ($= -0.2$), when $u = 0.533$, $\zeta = 0.04$, $\omega = 0.2$ and $A = 0.8$. (g) Plot of the power spectrum $P(\omega)$ for the example (f). $P(\omega)$ is roughly a constant over 3 decades, which indicates chaos. (h) Restricting the motion to small amplitudes (keeping only the linear terms in the dynamics) results in periodic motion. Plot shown for, $r = 0.2$, $\zeta = 0.04$, $\omega = 0.2$ and $A = 0.8$.

In the classical Heisenberg model, spins \mathbf{S}_i are arranged on the sites i of a regular lattice in d -dimensions. Each spin is a vector with three components and each component can assume continuous values. The energy of a configuration is given by,

$$E = -J \sum_{\langle i,j \rangle} \mathbf{S}_i \cdot \mathbf{S}_j, \quad (1.2)$$

where J is the strength of the exchange coupling between the nearest neighbour spins i and j . At high temperatures, the equilibrium phase is a paramagnet with the equilibrium magnetisation $\mathbf{M} \equiv \langle \sum_i \mathbf{S}_i \rangle = 0$. At temperatures below the critical point T_c ($T_c > 0$ when $d > 2$), the equilibrium phase of the system is a spontaneously broken symmetry phase which is ferromagnetic ($M \neq 0$) if $J > 0$, or anti-ferromagnetic if $J < 0$. Since we will be interested in physics at length scales much larger than any microscopic length (typically of order lattice spacing $a \sim 10 \text{ \AA}$), it is convenient to work with 'coarse-grained' magnetisation variables $\vec{\phi}(\mathbf{r}, t)$ which is an average of \mathbf{S}_i over a coarse-graining length l , where $a \ll l < \xi$, the spin correlation length. A systematic way of realising the coarse-graining is by using the Hubbard-Stratonovich transformation [12], and then taking a continuum limit to obtain the Landau-Ginzburg free-energy functional,

$$F[\vec{\phi}] = \int d^d x \left[\frac{\sigma}{2} (\nabla \vec{\phi})^2 + \frac{r}{2} (\vec{\phi} \cdot \vec{\phi}) + \frac{u}{4} (\vec{\phi} \cdot \vec{\phi})^2 \right]. \quad (1.3)$$

The parameters σ , r and u are related to T , J , a , d and z (the coordination number). The parameter r is proportional to $T - T_c^{MF}$ ($T_c^{MF} \equiv$ mean field critical temperature) and so when $r < 0$, the minima of the above free-energy density are at a nonzero magnitude of $\vec{\phi}$ and infinitely degenerate. As in the single particle example, we arrive at equations of motion for the spin starting with a Heisenberg spin model interacting with a heat bath (consisting of phonons or electrons) — the resulting equations of motion have both inertia and dissipation and ofcourse thermal noise. We first analyse the interplay between dissipation and inertia by studying the ordering dynamics of this spin model as it approaches equilibrium following a quench from the high temperature phase [13, 14, 15]. Next we study the effect of external driving on a Heisenberg magnet in the presence of both dissipation and inertia

[16, 17]. In the last problem we drive the Heisenberg spins by an external thermal current generated by sandwiching the spin system between two different heat sources [18]. Note that in the last two problems the spin system is driven far from its equilibrium configuration.

1.1 Phase Ordering Kinetics of Heisenberg magnets

Consider a regular lattice of Heisenberg spins in a d -dimensional box in contact with a heat bath at temperature T . We start with an equilibrium configuration at $T > T_c$, given by an average magnetisation $\langle \vec{\phi}(\mathbf{r}) \rangle = 0$ and a spin correlation function $\langle \vec{\phi}(\mathbf{r} + \mathbf{x}) \cdot \vec{\phi}(\mathbf{x}) \rangle \sim \exp(-r/\xi(T))$, where the bulk correlation length $\xi(T)$ is of the order of a few lattice spacings. The spin system is quenched from this paramagnetic phase to a temperature $T < T_c$, as shown in Fig. (1.4). The spins now evolve very slowly towards equilibrium, since the infinitely degenerate equilibrium states with broken continuous symmetry compete with each other to establish order. How do we mathematically describe this dynamics towards equilibrium?

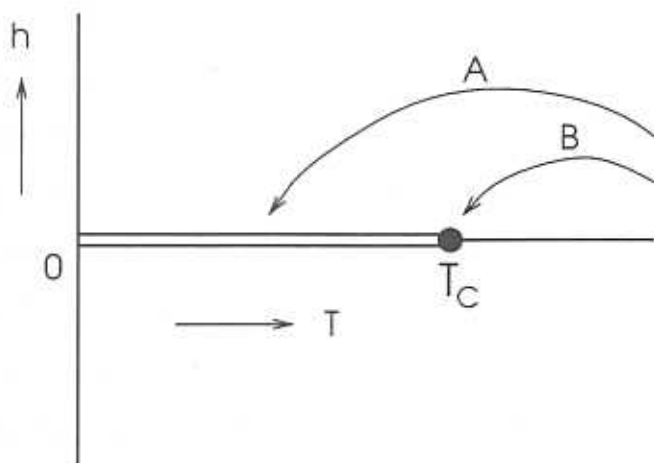


Figure 1.4: T - h phase diagram of the Heisenberg model for $d > 2$. Arrows show quenches to (A) $T < T_c$ and (B) $T = T_c$ starting from the paramagnetic phase.

It would seem that the derivation of the coarse-grained equations of motion for the spin density starting from a microscopic Hamiltonian describing the coupling of the spin system with the heat bath, is a hopeless task (this program has nevertheless been successfully carried out in a few simple cases such as (a) a two-level system coupled to a heat bath of harmonic

oscillators [19] and (b) an Ising system coupled to a heat bath of phonons [20, 21]). Instead of going through a tedious calculation, we shall provide an impressionistic derivation of our final coarse-grained equations based mainly on symmetry and simplicity.

The heat bath which may consist of either a collection of electrons or phonons interacting with the local spin is a source of dissipation and noise. In general the Hamiltonian can be written as $H = H_{spin} + H_{bath} + H_{int}$, where H_{spin} , H_{bath} are the spin system and heat bath contributions to H respectively, while H_{int} arises from the interaction of the heat bath with the spin system. To arrive at the effective equations of motion for the spin system, we need to make assumptions on the nature of the heat bath; the heat bath variables are assumed 'fast' with relaxation time scales well separated from those of the slower spin system variables. This allows one to integrate out the heat bath variables (for calculational convenience represented as an assembly of simple harmonic oscillators linearly coupled to the local spins) to arrive at effective equations of motion for the spin variables. This has the form of a generalised Langevin equation

$$\frac{\partial \phi_\alpha(\mathbf{r}, t)}{\partial t} = \text{Inertia} + \text{Dissipation} + \text{Noise}, \quad (1.4)$$

where $\alpha = 1, 2, 3$ denotes the vector components of the spin. The first term (Inertia) describes the Hamiltonian dynamics of the spins; thus $\dot{\phi}_\alpha \equiv \{\phi_\alpha, H_{spin}\} = \int \{\phi_\alpha, \phi_\beta\} \delta F / \delta \phi_\beta$ where the curly brackets denote the Poisson Bracket between two classical variables defined on phase space [2, 19]. In the last identity we have identified H_{spin} with the continuum free-energy functional Eq. (1.3). With the usual Poisson Algebra for the spins ϕ_α , the inertial term may be easily evaluated to obtain the well known Larmour precession formula $\dot{\vec{\phi}} = \vec{\phi} \times \vec{H}_{mol}$, where the molecular field $\vec{H}_{mol} \equiv -\delta F / \delta \vec{\phi}$.

Both Dissipation and Noise originate from the coupling of the spin system to the heat bath, and serve to guarantee that the spin configuration approaches equilibrium at late times. The form of the interaction between the spins and the heat bath variables depends on the nature of the heat bath. For instance, the heat bath could be a collection of phonons; in this case the interaction between the local spins and the phonon bath (at low enough temperatures [22]) does not effect the total spin. On the other hand, if the heat bath were a collection of electrons, then the spin of the electron could couple to the local spins. This

would result in a change in the total magnetisation of the spin system. Thus depending on the nature of the heat bath - spin system interaction, the total spin may be conserved or not conserved during the dynamics. A reasonable choice for the dissipation, which ensures that the spin system evolves towards equilibrium, is $\Gamma \nabla^2(\delta F[\vec{\phi}]/\delta\phi_\alpha)$ when the total spin is conserved or $-\Gamma \delta F[\vec{\phi}]/\delta\phi_\alpha$ when the total spin is not conserved. Here Γ is the spin mobility obtained on integrating out the heat bath variables.

The heat bath is also a source of Noise, whose statistics is simplified if we make an additional assumption (First Markov Approximation [19]); the future time evolution of the spin system will depend solely on the values of the spin variables in the present. This makes the noise term local in time. We make the further simplifying assumption that the noise is a random variable taken from a Gaussian distribution, independent and uncorrelated in space and time, with zero mean and a variance equal to D . To ensure that the spin system approaches equilibrium at late times we need to make $D \propto \Gamma$ (Fluctuation-Dissipation Theorem) [23, 24].

Starting from the paramagnetic phase, the generalised Langevin equation (Eq. (1.4)) describes how the local spin density evolves in time following a quench across T_c . The paramagnetic configuration can be shown to be linearly unstable; the spin configuration at a later time consists of large patches of the nearly ordered degenerate phases separated by regions where the spins deviate strongly from the ordered phases. Such spin excitations may in general be decomposed into two parts – a smooth part $\vec{\phi}_{sm}$ coming from spin-wave configurations (Fig. 1.5) and a singular part $\vec{\phi}_{sing}$ coming from topological defects. Spin-waves are low energy excitations with a dispersion $\epsilon_{\mathbf{k}} \sim k^2$, where the wavelength is $2\pi/k$. Any smooth spin excitation can be written as a superposition of spin-waves of different wavelengths. On the other hand, topological defects in Heisenberg spin systems in $d = 3$ are hedgehog or monopole configurations (Fig. (1.5)), where $\vec{\phi} \sim \hat{r}$ except in a core region of size ξ_{core} (order of a lattice spacing) surrounding the centre of the defect, where the order parameter is undefined. These are massive excitations and cannot be destroyed by smooth local changes in the spins.

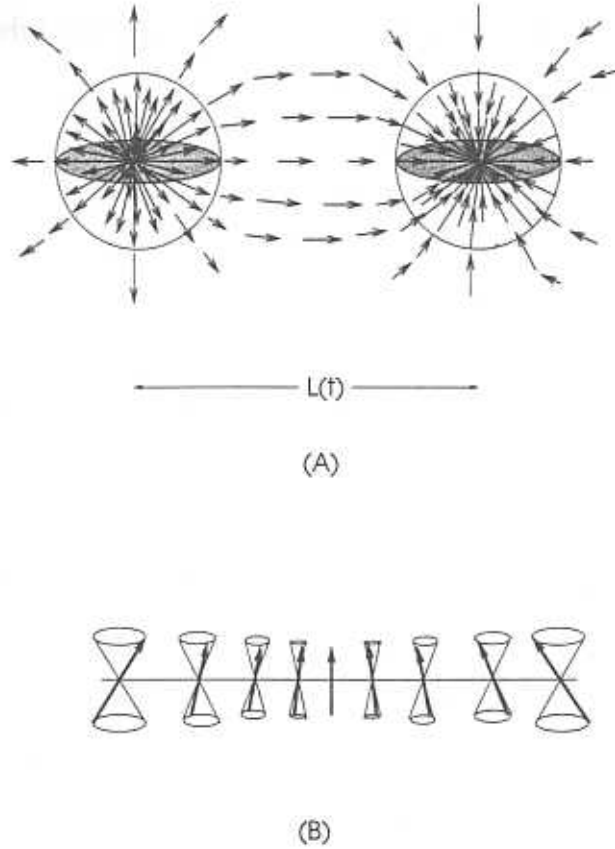


Figure 1.5: (A). Topological defects in the Heisenberg model – a monopole and anti-monopole pair is separated by a distance $L(t)$. (B). Spin-waves which represent low energy excitations in the Heisenberg system.

The Heisenberg spins relax via a variety of scattering mechanisms — spin-wave-spin-wave scattering, spin-wave-defect scattering and the mutual annihilation of defect-anti-defect pairs. In the purely dissipative systems with no inertia studied so far [1], the lifetime of spin-waves is short and so at late times the only surviving spin excitations are defects dressed by their interaction with spin-waves. At late times the dressed defects organise in a statistically self similar spatial pattern, which in most systems is characterized by a single length scale ($L(t) \gg \xi(T)$) which typically grows algebraically in time $L(t) \sim t^{1/z}$. The dynamical exponent z can be derived for various models using scaling arguments [25] — for the Heisenberg model, $z = 2$ (purely dissipative, nonconserved dynamics) and $z = 4$ (purely dissipative, conserved dynamics) in dimensions three or higher. A simple scaling argument can be used to determine the z exponent for the conserved model; the extension to

nonconserved dynamics is not straight forward since the mobility picks up a scale dependence demanding a more careful analysis [26, 25]. The conserved dynamics can be written as a continuity equation

$$\frac{\partial \vec{\phi}}{\partial t} + \vec{\nabla} \cdot \vec{j} = 0 \quad (1.5)$$

where

$$\vec{j} = -\Gamma \vec{\nabla} \frac{\delta F}{\delta \vec{\phi}} = \Gamma \vec{\nabla} \vec{\mu}, \quad (1.6)$$

is the spin current. The chemical potential, $\vec{\mu}$ scales as L^{-2} which follows from the Gibbs-Thompson relation [1] for vector order parameters when there is local equilibrium. Since the current \vec{j} is proportional to the ‘velocity’ (dL/dt), it follows readily from Eq. (1.6) that $L(t) \sim t^{1/4}$ or $z = 4$. We will make use of similar arguments later when we include inertia in the dynamics.

The statistically self similar spatial distribution of domains is reflected in the scaling behaviour of the equal-time correlation function $C(r, t) = \langle \vec{\phi}(\mathbf{r} + \mathbf{x}, t) \cdot \vec{\phi}(\mathbf{x}, t) \rangle \sim f(r/L(t))$, where $\langle \dots \rangle$ denotes an average over initial configurations and thermal noise [1, 3]. The system also exhibits a slow decay of memory of the initial configurations which shows up as an algebraically decaying autocorrelation function, $A(t) = \langle \vec{\phi}(\mathbf{x}, t) \cdot \vec{\phi}(\mathbf{x}, 0) \rangle \sim L(t)^{-\lambda}$. These observations imply that viewed over a length scale $L(t)$, the physics is statistically self-similar. Over this length scale microscopic details are irrelevant; this gives rise to the notion of *universality* characterised by the exponents z, λ and the scaling function $f(x)$ [1]. Some of the aspects of the system that define a universality class are spatial dimension, conservation laws (spin, energy) and symmetries of the order parameter. Most other microscopic details and system parameters are irrelevant. In particular, as long as the system is quenched to below T_c , the temperature is an irrelevant parameter, merely modifying the values of surface tension σ and equilibrium magnetisation M . This is best pictured schematically as a Renormalisation Group flow diagram [26] showing fixed points at $T = 0, T_c$ and ∞ (Fig. (1.6)). The universal characteristics of the dynamics following a quench to low temperatures is therefore controlled by the zero temperature fixed point (ZFP).

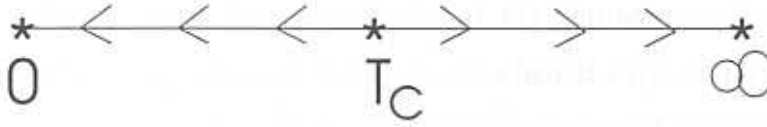


Figure 1.6: Flow diagram showing the fixed points and flows on the temperature line.

As mentioned above, this scenario works when the spin-waves relax fast leaving behind slowly moving defects. It is conceivable that the situation may be altered when we include inertia in the dynamics of the spins, giving a longer life span to spin-waves. We therefore ask if the inertial (precession) terms are relevant and whether the above picture is still valid. This is the subject of the first chapter. Our results are summarized below.

In the *Nonconserved case*, we find that the precession does not affect the asymptotic growth laws and scaling functions, and is therefore irrelevant at the ZFP. However preasymptotic correlation functions show features coming from the precession. We argue that these preasymptotic features can be understood as arising from the interaction of the long lived spin-waves with slowly evolving defects [13, 14].

In the *Conserved case*, we find that the precession dominates the dynamics after a crossover time $t_c \sim 1/g^2$ (where g is the coefficient of the Larmour term). Inertial terms are therefore relevant, driving the dynamics to a new ‘torque-driven’ fixed point with $z = 2$ and $\lambda \approx 5.05$. Crossover scaling forms describe physical quantities at late times (like the inter defect distance $L(t, g)$ and correlation functions $C(r, t, g)$ and $A(t, g)$) for all values of g [15].

To understand these features analytically, we attempt a perturbative expansion about the $g = 0$ (purely dissipative) and the $g = \infty$ (purely inertial) fixed points. From an analysis of the approximate Gaussian Closure Scheme [1], we argue that the crossover features cannot be understood by a theory which does not include the interaction between spin-waves and defects. The crossover phenomena leads to another question — if the torque dominates the asymptotic dynamics when the order parameter is conserved, then can one drop the dissipation and consider the ordering dynamics due to spin precession alone? We find that there is a close analogy between this *Pure Torque* model and the dynamics of the Random Field Ising model. We argue that dissipation is a dangerously irrelevant variable at the ‘torque-driven’ fixed point and therefore should not be set to zero apriori.

For quenches to the *Critical Point*, we find that the torque is irrelevant when the dynamics is nonconservative, but relevant below $d = 6$ when the dynamics is conservative. In the latter case, a diagrammatic perturbation calculation shows that $z = 4 - \varepsilon/2$ and $\lambda = d$ (where $\varepsilon = 6 - d$) at the new fixed point. The result $\lambda = d$ is more general and can be seen to hold to all orders in perturbation [15].

1.2 Dissipative Dynamics of Driven Heisenberg magnets

In our next chapter, we introduce an external driving to the inertial and dissipative dynamics of the Heisenberg model. External driving may give rise to steady states, very different from equilibrium configurations distributed as $\exp(-\beta H)$ [8], where H is the Hamiltonian and $\beta \equiv 1/k_B T$ the inverse temperature. Consider a driven diffusive lattice gas model (DDLG) [8] in one dimension, where particles interacting via hard core repulsion can hop from a site to the nearest neighbour sites if vacant with probability p to the right and q to the left, at every time step Δt (Fig. 1.7) (assume periodic boundary conditions).

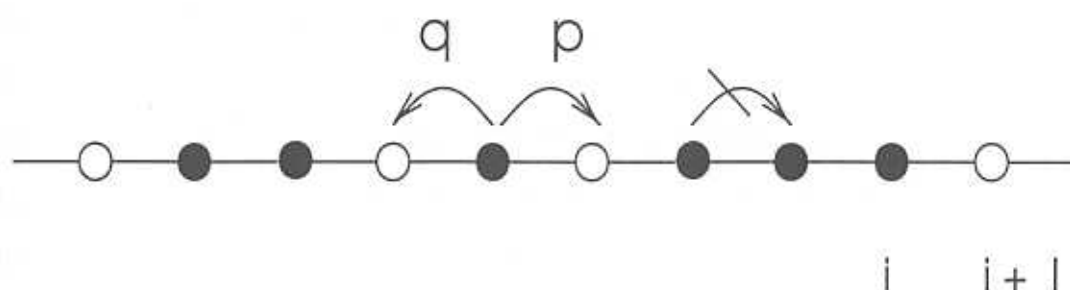


Figure 1.7: Hopping rules for the model. Black spheres indicate particles and white spheres are the vacant sites.

The probability that a particle is at site i at time t can be described by a master equation. However to understand the long time and long wave-length behaviour, it is convenient to derive a coarse-grained equation for the densities from the master equation and study it in the continuum limit. The time evolution of the local density $\rho(x, t)$ (or to use the Ising

language, the local magnetisation defined by $\phi(x, t) = 2\rho(x, t) - 1$, will have the form of a continuity equation

$$\frac{\partial \phi}{\partial t} + \frac{\partial j}{\partial x} = \frac{\partial \eta}{\partial x}, \quad (1.7)$$

since the total number of particles is conserved. We have included as part of the current, a conserved gaussian white noise η whose correlator is,

$$\langle \eta(x, t) \eta(x', t') \rangle = 2k_B T D \delta(x - x') \delta(t - t'). \quad (1.8)$$

In the absence of driving ($p = q$), the current j has the form

$$j = j_{diss} = \Gamma \frac{\partial \mu}{\partial x}, \quad (1.9)$$

where $\mu = -\delta F / \delta \phi$ is the chemical potential and F is a coarse-grained free-energy functional. The resulting continuity equation breaks time reversal invariance and is therefore dissipative. The Fluctuation-Dissipation Theorem (FDT) demands that the dissipation and noise should be related, *i.e.*, $\Gamma = D$, to ensure that the system reaches equilibrium at late times. This can be seen by writing the associated Fokker-Planck equation for the probability distribution of ϕ [24],

$$\frac{\partial P}{\partial t} = T \int dx \Gamma \frac{\delta}{\delta \phi} \left(\frac{1}{T} \frac{\delta F}{\delta \phi} + \frac{D}{\Gamma} \frac{\delta}{\delta \phi} \right) P. \quad (1.10)$$

It is clear that canonical distribution $P_{eq} \propto \exp(-\beta F)$ is a stationary solution of the equation.

The presence of the drive ($p \neq q$) gives rise to an extra piece j_{drive} in the total current. The form of j_{drive} can be obtained starting from the microscopic rules, but the route is cumbersome in general. Most often the form of the current can be derived by appealing to symmetry principles and conservation laws. The drive explicitly breaks (i) $x \longleftrightarrow -x$ (reflection) symmetry. However the dynamics should respect (ii) a joint inversion symmetry, $\phi \longleftrightarrow -\phi$ and $x \longleftrightarrow -x$, which means that a particle ($\phi > 0$) moving to the right is equivalent to a hole ($\phi < 0$) moving to the left. Invoking (i) we can write down a general form for the current

$$j_{drive} = a_{mn} \partial_x^m \phi^n + b_n \phi^n, \quad (1.11)$$

where repeated indices are summed over. Dropping the derivative terms in j_{drive} as being irrelevant in the ‘hydrodynamic’ limit, we find that to lowest order in nonlinearity $j_{drive} =$

$b_1\phi + b_2\phi^2$. Now invoking symmetry (ii) we see immediately that there can be no linear contribution. This can be seen even without using (ii), since we can get rid of this linear term by making a Galilean shift, $x \rightarrow x - b_1t$ and $t \rightarrow t$. Thus the coarse-grained Langevin equation takes the form

$$\frac{\partial\phi}{\partial t} = \Gamma\partial_x^2\frac{\delta F}{\delta\phi} + \lambda\partial_x\phi^2 + \eta. \quad (1.12)$$

The corresponding Fokker-Planck equation reads,

$$\frac{\partial P}{\partial t} = T \int dx \Gamma \frac{\delta}{\delta\phi} \left(\frac{1}{T} \frac{\delta F}{\delta\phi} + \frac{D}{\Gamma} \frac{\delta}{\delta\phi} \right) P - \frac{\lambda}{T\Gamma} \int dx \frac{\delta}{\delta\phi} (\partial_x \phi^2 P). \quad (1.13)$$

Clearly $\exp(-\beta F)$ is not a stationary solution of Eq. (1.13); the steady state is no longer an equilibrium configuration. Therefore the FDT relation which ensures that the stationary distribution is the canonical distribution need not hold, implying that the presence of the external drive will in general result in a breakdown of the FDT.

Our aim is to introduce inertia in the above driven dynamics. To bring in effects of inertia in the dynamics we attach a Heisenberg spin \mathbf{S}_i to each particle in the DDLG model. The external driving produces a particle current which feeds into the dynamics of the spins via the inertial term $\mathbf{S} \times \mathbf{H}_{mol}$, where \mathbf{H}_{mol} is the local molecular field. Our analysis for an arbitrary d -dimensional system, where the external drive is along say the x direction, shows that the driving appears as $\lambda \mathbf{S} \times \partial_x \mathbf{S}$ in the coarse-grained Langevin equation for the spins. In addition the Langevin equation possesses a ‘temperature-like’ parameter v . At late times we study the ‘non-equilibrium phase diagram’ of final states at ‘high temperature’ ($v > 0$), ‘critical temperature’ ($v = 0$) and ‘low temperature’ ($v < 0$). The high temperature phase is paramagnetic with zero magnetisation $\langle \mathbf{S} \rangle = 0$ and exponentially decaying spin-spin correlation functions. At the critical temperature, the dynamics exhibits scale invariance and the universal behaviour of the system may be determined by the fixed points of the dynamical renormalisation group equations. For instance, the spin-spin correlator obeys the anisotropic scaling form $C(x, t) = x_{\parallel}^{2\chi} F(t/x_{\parallel}^z, x_{\perp}/x_{\parallel}^{\zeta})$. The exponents χ, z, ζ and the scaling function $F(x, y)$ may be evaluated within an ϵ -expansion about the upper critical dimension of the driving term, $d_c = 4$. For $d < 4$ there is a nontrivial, driving induced, stable fixed point, and the exponents to $O(\epsilon)$ are given by $z = 2 - 16\epsilon/35$, $\zeta = 1 - 2\epsilon/15$ and $\chi = 1 - d/2$. The low temperature behaviour of this model turns out to be most interesting. The system

is driven to a chaotic attractor by the external current which manifests in a scale invariant $1/\omega^\alpha$ (ω is the frequency) behaviour of the power-spectrum of the total magnetisation and the energy density. This spatio-temporal chaos may be 'controlled' by fixing the projection of the spins along the anisotropy axis. Furthermore we may target [11] this helical steady state; the spins then settle into an inhomogeneous helical configuration which is dynamically stable. This chiral configuration possesses a massless Goldstone mode, generated by continuous global rotations of the spins about the helical axis which destabilises the chiral steady state configuration when $d \leq 2$.

1.3 Dynamics of Heisenberg magnets in the presence of a Temperature gradient

In the last chapter we investigate the nonequilibrium dynamics of Heisenberg spins driven by a temperature current — the phenomenon of heat conduction where all three effects, namely, dissipation, driving and inertia are present. To introduce the problem let us start with an experiment Fig. (1.8). Place a rod of size L in between two heat baths of temperatures, T_1 and T_2 (with $T_1 > T_2$).

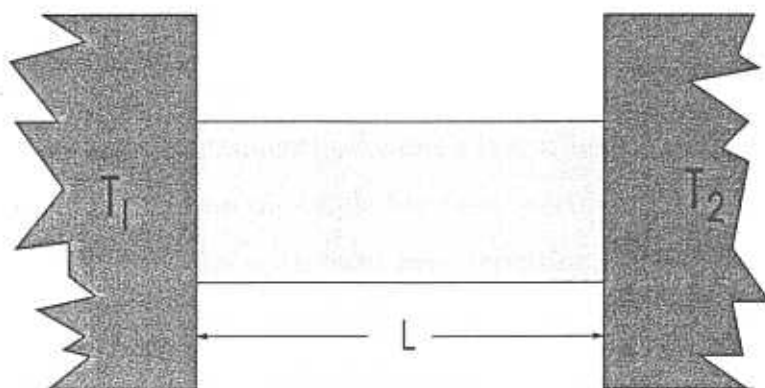


Figure 1.8: Typical heat conduction experiment

After some time a steady state will set in the rod, characterised by a decreasing temperature profile from the side 1 to side 2. The local temperature $T(\mathbf{x}, t)$ satisfies a phenomenological

equation known as the Fourier equation [27, 24],

$$\begin{aligned}\frac{\partial T(\mathbf{x}, t)}{\partial t} &= \frac{1}{\rho c} \vec{\nabla} \cdot (\kappa(T) \vec{\nabla} T(\mathbf{x}, t)) \\ &= -\frac{1}{\rho c} \vec{\nabla} \cdot \vec{J}(\mathbf{x}, t)\end{aligned}\quad (1.14)$$

where ρ is the density, c is the specific heat per unit mass, $\kappa(T)$ is the conductivity and $\vec{J}(\mathbf{x}, t) = -\kappa(T) \vec{\nabla} T(\mathbf{x}, t)$ is the local heat current. In the steady state the temperature field $T(\mathbf{x}, t)$ becomes time independent, which implies $\vec{\nabla} \cdot \vec{J} = 0$ or $\vec{J} = \text{const}$. If the conductivity κ is finite in the thermodynamic limit, then $J \sim (T_1 - T_2)/L$. Extensive experimental studies carried out over the years are in agreement with all the above facts [28, 29]. The theoretical challenge is to understand how one arrives at these facts starting from microscopic equations, like Newton's laws. To date there has been no satisfactory explanation. Since there are some excellent reviews [30] on this topic, we mention only the salient features here. To derive Eq.(1.14) one may start from the Boltzmann transport equation [27] along with two basic standard assumptions, (i) molecular chaos, (ii) presence of local equilibrium. With these one can derive Fourier's law in the low density limit. The thermal conductivity proportional to \sqrt{T} can then be obtained from the Kubo formula [31] within linear response at a fixed temperature. The validity of the basic assumptions may be checked by studying simple models either numerically or (if lucky) exactly. The study of such simple models would tell us what are the basic ingredients needed to achieve local equilibrium and Fourier's law. However, most simple models studied so far fail to yield such essential properties as local thermal equilibrium (LTE). Consequently Fourier's law of heat conduction is not realised in 1-dimensional systems like a chain of simple harmonic oscillators [32] or Fermi-Pasta-Ulam (FPU) oscillators [33] or particles with hard core repulsion. Most of these models are integrable; for such systems there exist an infinite set of conserved quantities apart from the energy, which break the phase space into isolated pockets preventing LTE [34]. In all these models the order parameter is scalar, an extension of such a study to vector order parameters might allow for faster equilibration and may give a better understanding of the origin of LTE and Fourier's law. We therefore investigate the dynamics of Heisenberg spins held between two different temperature baths, T_1, T_2 at the boundaries [18]. The spin dynamics in the bulk is reversible precession (inertia), while the boundary spins are allowed to dissi-

pate energy at the temperature of the bath. The temperature gradient drives the system to a nonequilibrium steady state. The nature of the steady state depends on the boundary conditions ; (i) non-zero spin flux across the boundaries (*non-conserved*) or (ii) no spin flux across the boundaries (*conserved*). In the conserved case, the temperature gradient sets up an energy current which drives the spin system to a steady state configuration. In the non-conserved case, the energy current couples to the spin current leading to novel steady state configurations. We discuss whether LTE holds and determine the scaling of the thermal conductivity with system size.

1.4 Note on Format

Each chapter starts with a short Introduction and a chapter wise break-up. After this follows a detailed analysis to the problem. Details of the calculations have been relegated to the Appendices for ease of reading. Every chapter ends with a summary of results, experimental implications, directions for future work and a bibliography. We therefore do not have a 'thesis summary' at the end.

Bibliography

- [1] A. J. Bray, *Adv. Phys.* **43**, 357 (1994).
- [2] P. C. Hohenberg and B. I. Halperin, *Rev. Mod. Phys.* **49**, 435 (1977).
- [3] J. D. Gunton, M. San Miguel and P. S. Sahni in *Phase Transitions and Critical Phenomena*, Vol. 8, eds. C. Domb and M. Green (Academic Press, NY, 1983).
- [4] J. T. Houghton in *The Physics of Atmospheres* (Cambridge University Press, Cambridge, 1977).
- [5] B. Mandelbrot in *The Fractal Geometry of Nature* (Freeman, San Francisco, 1982).
- [6] D. R. Montgomery and W. E. Dietrich, *Science* **255**, 826 (1992).
- [7] B. Alberts, D. Bray, M. Ruff and J. D. Watson in *Molecular Biology of the Cell*, 3rd ed. (Garland Publishing, NY, 1995).
- [8] B. Schmittmann and R. K. P. Zia in *Phase Transitions and Critical Phenomena*, Vol. 17, eds. C. Domb and J. L. Lebowitz (Academic Press, NY, 1995).
- [9] J. M. T. Thompson and H. B. Stewart in *Nonlinear Dynamics and Chaos* (John Wiley and Sons, NY, 1987).
- [10] R. Seydel, *Physica D* **17**, 308 (1985).
- [11] T. Shinbrot, C. Grebogi, E. Ott and J. A. Yorke, *Nature* **363**, 411 (1993).
- [12] N. Goldenfeld in *Lectures on Phase Transitions and the Renormalisation Group* (Addison Wesley Publishing Co., Reading, 1992).

- [13] J. Das and M. Rao, Phys. Rev. E **57**, 5069 (1998).
- [14] J. Das and M. Rao, Physica A **270**, 253 (1999).
- [15] J. Das and M. Rao, Phys. Rev. E **62**, 1601 (2000).
- [16] J. Das, M. Rao and S. Ramaswamy, submitted.
- [17] J. Das, M. Rao and S. Ramaswamy, in preparation.
- [18] J. Das and M. Rao, in preparation.
- [19] C. W. Gardiner in *Quantum Noise* (Springer-Verlag, Berlin, 1991).
- [20] H. Mori, Prog. Theor. Phys. **33**, 423 (1961).
- [21] R. Zwanzig in *Lectures in Theoretical Physics*, Vol. III, eds. W. E. Brittin, B. W. Downs and J. Downs (Interscience Publishers Inc., NY, 1961).
- [22] C. Kittel in *Introduction to Solid State Physics*, 3rd ed. (Wiley Eastern Pvt. Ltd., New Delhi, 1971).
- [23] N. G. Van Kampen in *Stochastic Processes in Physics and Chemistry* (North Holland Physics Publishing, Amsterdam, 1985).
- [24] P. M. Chaikin and T. C. Lubensky in *Principles of Condensed Matter Physics* (Cambridge University Press, Cambridge, 1995).
- [25] A. J. Bray and A. D. Rutenberg, Phys. Rev. E **49**, R27 (1994).
- [26] A. J. Bray, Phys. Rev. B **41**, 6724 (1990).
- [27] K. Haug in *Principles of Statistical Mechanics*, 2nd ed. (John Wiley & Sons, NY, 1987).
- [28] Ezer and Griffiths, Proc. Phys. Soc. (Lond.) **41**, 151 (1928).
- [29] M. N. Saha, and B. N. Srivastava in *A Treatise on Heat* (The Indian Press Ltd., Calcutta, 1950).

- [30] F. Bonetto, J. L. Lebowitz and L. Rey-Bellet, math-ph/0002052 (2000).
- [31] W. M. Visscher, Phys. Rev. A **10**, 2461 (1974) ; D. Forster in *Hydrodynamic Fluctuations, Broken Symmetry and Correlation Functions* (W. A. Benjamin Inc., London, 1975).
- [32] Z. Reider, J. L. Lebowitz and E. Lieb, J. Math. Phys. **8**, 1073 (1967).
- [33] S. Lepri, R. Livi and A. Politi, Physica D **119**, 140 (1998).
- [34] A. Dhar, *Studies of Nonequilibrium Steady States of Driven Systems*, Ph.D thesis (University of Bombay, 1998).

Chapter 2

Dynamics of Ordering in Heisenberg magnets

In this chapter we study the dynamics of phase ordering of a Heisenberg magnet when the spins precess around a local magnetic field (inertial dynamics) and dissipate into a heat bath (dissipative dynamics). The dynamics may either allow the total magnetisation to change in time (*nonconserved model*) or conserve the total magnetisation (*conserved model*). In Section 2.1 we investigate the phase ordering dynamics following a quench to zero temperature by numerically simulating the Langevin equation (2.1). This is done for both the nonconserved model (Section 2.1.1 A) and the conserved model (Section 2.1.1 B). Next we propose a study of the dynamics using a perturbative analysis about two different limits — (i) we treat dissipation as a *singular* perturbation over the purely reversible torque dynamics, and (ii) we treat the torque as a perturbation over the purely dissipative dynamics. The latter perturbation scheme reveals the importance of the interaction between spin-waves and defects in the late stages of the dynamics. In the last section we study the dynamics following a quench to the critical point using a Dynamical Renormalisation Group. Technical details are presented in the three appendices that follow.

As discussed in the Introduction, the generalised Langevin equation [1] for the dynamics of Heisenberg spins including inertia is given by,

$$\begin{aligned} \frac{\partial \phi_{\alpha}(\mathbf{r}, t)}{\partial t} = & \int_{\mathbf{r}', t'} \{ \phi_{\alpha}(\mathbf{r}, t), \phi_{\beta}(\mathbf{r}', t') \} \frac{\delta F}{\delta \phi_{\beta}(\mathbf{r}', t')} \\ & - \Gamma (-i\nabla)^{\mu} \frac{\delta F}{\delta \phi_{\alpha}(\mathbf{r}, t)} + \eta_{\alpha}(\mathbf{r}, t) , \end{aligned} \quad (2.1)$$

where ϕ_α is a 3-component spin order parameter, F is a coarse-grained free-energy functional as in Eq. (1.3), $\{\cdot, \cdot\}$ is the Poisson bracket, and η_α is the noise. The first term on the right hand side describes inertia, while the second is the usual dissipation, with $\mu = 2$ or 0 according as whether the order parameter is conserved or not. The noise η_α has mean zero, and the correlator $\langle \eta_\alpha(\mathbf{r}, t) \eta_\beta(\mathbf{r}', t') \rangle = 2 \Gamma k_B T \delta_{\alpha\beta} (-i\nabla)^\mu \delta^d(\mathbf{r} - \mathbf{r}') \delta(t - t')$ is proportional to the temperature T of the heat bath, a requirement of FDT. The spin components ϕ_α ($\alpha = 1, 2, 3$) satisfy the usual Poisson algebra [1, 2],

$$\{\phi_\alpha(\mathbf{r}, t), \phi_\beta(\mathbf{r}', t')\} = \Omega_L \epsilon_{\alpha\beta\gamma} \phi_\gamma(\mathbf{r}, t) \delta(\mathbf{r} - \mathbf{r}') \delta(t - t'), \quad (2.2)$$

where $\epsilon_{\alpha\beta\gamma}$ is the completely antisymmetric unit tensor in three 'spin-space' dimensions and Ω_L is the Larmour frequency.

It is convenient to scale space \mathbf{r} , time t , the order parameter $\vec{\phi}$ and the noise $\vec{\eta}$ as (we apologise for this choice of notation; in this section vector \mathbf{r} will denote the spatial position vector while r will denote the coefficient of the quadratic term in the free-energy functional F (Eq. (1.3)), we hope this will be clear from the context.),

$$\mathbf{r} \rightarrow \sqrt{\frac{|r|}{\sigma}} \mathbf{r}, \quad t \rightarrow \Gamma |r| \left(\frac{|r|}{\sigma}\right)^\mu t, \quad \vec{\phi} \rightarrow \sqrt{\frac{|r|}{u}} \vec{\phi}, \quad \vec{\eta} \rightarrow \left(2k_B T \Gamma \left(\frac{|r|}{\sigma}\right)^{(d+\mu)/2} |r|\right)^{-1/2} \vec{\eta},$$

to obtain the Langevin equation in dimensionless form,

$$\frac{\partial \vec{\phi}}{\partial t} = (-i\nabla)^\mu \left(\nabla^2 \vec{\phi} - \text{sgn}(r) \vec{\phi} - (\vec{\phi} \cdot \vec{\phi}) \vec{\phi} \right) + g \left(\vec{\phi} \times \nabla^2 \vec{\phi} \right) + \sqrt{\alpha} \vec{\eta}, \quad (2.3)$$

with the noise correlator,

$$\langle \eta_\alpha(\mathbf{r}, t) \eta_\beta(\mathbf{r}', t') \rangle = \delta_{\alpha\beta} (-i\nabla)^\mu \delta(\mathbf{r} - \mathbf{r}') \delta(t - t'). \quad (2.4)$$

The dimensionless parameter $g = (\Omega_L/\Gamma) \sqrt{|r|/u}$ is the ratio of the precession frequency to the relaxation rate and $\alpha = 2k_B T u (|r|/\sigma)^{d/4} / \Gamma r^2$. To get a feel for the values assumed by g , let us set $\Omega_L \sim 10^7$ Hz, $\Gamma \sim 10^6 - 10^{10}$ Hz, which gives a range of $g \sim 10^{-3} - 10$.

2.1 Dynamics at $T = 0$

Let us now prepare the system initially in its paramagnetic phase $T > T_c$ and quench to zero temperature. This fixes $\alpha = 0$; the noise drops out, making the equations of motion

completely deterministic. The initial conditions taken from paramagnetic configurations are, however, random. As we discussed in Sect. 1.1, the universal features of the dynamics following a quench to any $T < T_c$ is controlled by the zero temperature ($T = 0$) fixed point (ZFP), so it suffices to study this limit. Note that for quenches below T_c , r should be taken to be negative.

From the solutions of Eq. (2.3), we calculate the equal-time correlator,

$$C(\mathbf{r}, t) \equiv \langle \vec{\phi}(\mathbf{x}, t) \cdot \vec{\phi}(\mathbf{r} + \mathbf{x}, t) \rangle, \quad (2.5)$$

and the autocorrelator,

$$C(\mathbf{0}, t_1 = 0, t_2) \equiv \langle \vec{\phi}(\mathbf{r}, t_1 = 0) \cdot \vec{\phi}(\mathbf{r}, t_2) \rangle, \quad (2.6)$$

where the angular brackets are averages over the random initial conditions and space. These correlators can be measured in experiments like neutron scattering [3] or video micrography [4].

We shall show explicitly in Appendix IIA, that the late time dynamics obeys standard scaling, suggesting the existence of a single growing length scale $L(t)$. This implies that at late times these correlators attain their scaling form

$$C(\mathbf{r}, t) \sim f(r/L(t)) \quad (2.7)$$

$$C(\mathbf{0}, t_1 = 0, t_2) \sim L(t_2)^{-\lambda}. \quad (2.8)$$

Here $L(t)$ is the length scale over which spins are correlated; this grows with time as $L \sim t^{1/z}$ where z is the universal growth exponent. The dynamical exponent z can also be determined from the scaling behaviour of the energy density. Since the magnitude of the order parameter saturates to its equilibrium value very fast, most of the contribution to changes in energy comes from the derivative term in the free-energy expression Eq.(1.3). Thus the energy density scaling may be computed from the time dependence of

$$\varepsilon = \frac{1}{V} \int d\mathbf{r} \langle (\nabla \vec{\phi}(\mathbf{r}, t))^2 \rangle. \quad (2.9)$$

For vector order parameters, the energy of a domain of size L scales as L^{d-2} , which immediately gives $\varepsilon \sim L(t)^{-2}$ at late times (this may also be seen by using Eq. (2.7)).

The existence of a single length scale implies that the dynamical exponent calculated from these two different quantities are the same. Since the smooth spin-wave fluctuations (see Sect. 1.1) relax faster than the typical time scale for defect-antidefect annihilation, the length scale measured by both the correlator and the energy density is also a measure of the distance between defects. Our analysis of the dynamics is based on computations of the scaling function $f(x)$, the growth exponent z and the autocorrelation exponent λ . Since Eq. (2.3) is a nonlinear partial differential equation, we are forced to use numerical or approximate methods.

2.1.1 Langevin Simulation

We discretise Eq. (2.3) both for the nonconserved ($\mu = 0$) and conserved ($\mu = 2$) dynamics on a simple cubic lattice (with size N ranging from 40^3 to 60^3) adopting an Euler scheme for the derivatives [5, 10]. The space and time intervals have been chosen to be $\Delta x = 3$ and $\Delta t = 0.01$ in the nonconserved case and $\Delta x = 2.5$ and $\Delta t = 0.2$ in the conserved case. With this choice of parameters, we have checked that the resulting coupled map does not lead to any instability. We have also checked that the results remain unchanged on slight variations of Δx and Δt . Unless otherwise specified, all calculated quantities are averaged over 30 uncorrelated initial configurations taken from an ensemble where each component of $\vec{\phi}$ is distributed uniformly between $[-1, 1]$ with zero mean (we have found that our conclusions are insensitive to the choice of initial conditions as long as one does not introduce any long-range correlations). Throughout our simulation we have used periodic boundary conditions.

A. Nonconserved Dynamics, $\mu = 0$

We begin our simulation of the Langevin equation for the nonconserved case [7, 8] by first calculating the time dependence of the energy density of the spins. Figure 2.1 shows a log-log plot of the energy density as a function of t for $g = 0, 0.5, 1, 2$ on a 60^3 lattice. The error bars are smaller than the size of the symbols. Upto these times ($t = 16000$), there is no evidence of finite size effects. The slight curvature seen in the data (especially for larger g) is due to finite time corrections. The bold line corresponds to $A/(t + t_0)$ where A and t_0 are varied to give the best fit to the data. This shows that the data gathered over 1.5-decades

gives a $z = 2$, independent of g .

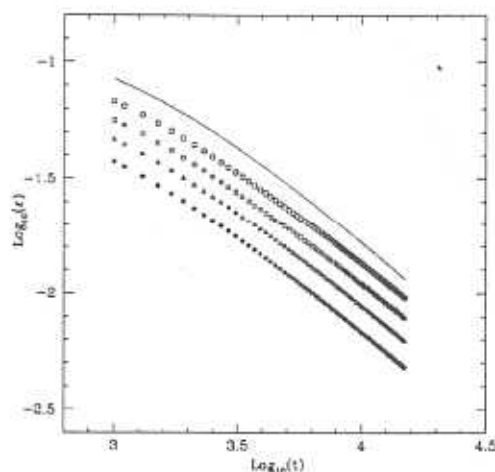


Figure 2.1: log-log plot of the energy density ε versus t for $g = 0(\circ)$, $g = 0.5(\square)$, $g = 1(\triangle)$, $g = 2(\star)$. The straight line fit (see text) gives $z = 2$.

We next calculate $C(r, t)$ at these late times for different values of g . Figures 2.2a-c are scaling plots of $C(r, t)$ versus $r/t^{1/2}$ (see Eq. (2.7)) for $g = 0$ and $g = 1$ on a 40^3 lattice (finite size effects manifest at $t > 12000$). The domain size $L(t)$, extracted from $C(r = L(t), t) = C(0, t)/2$, scales as $t^{1/z}$ where the exponent is again $z = 2$ (within statistical errors) and independent of g . Fig. 2.2a shows that the scaling function $f(x)$ is also independent of g , for $g = 0, 0.5, 1, 2$. This scaling function compares very well with an analytical scaling form for $g = 0$ (the bold line in Fig. 2.2c) calculated using an approximate theory due to Bray, Puri and Toyoki (BPT) [9] which has the form $f(x) = (3\gamma/2\pi) [B(2, 1/2)]^2 F(1/2, 1/2, 5/2; \gamma^2)$ where $\gamma = \exp(-x^2/8)$ and B and F are the beta and the hypergeometric functions respectively.

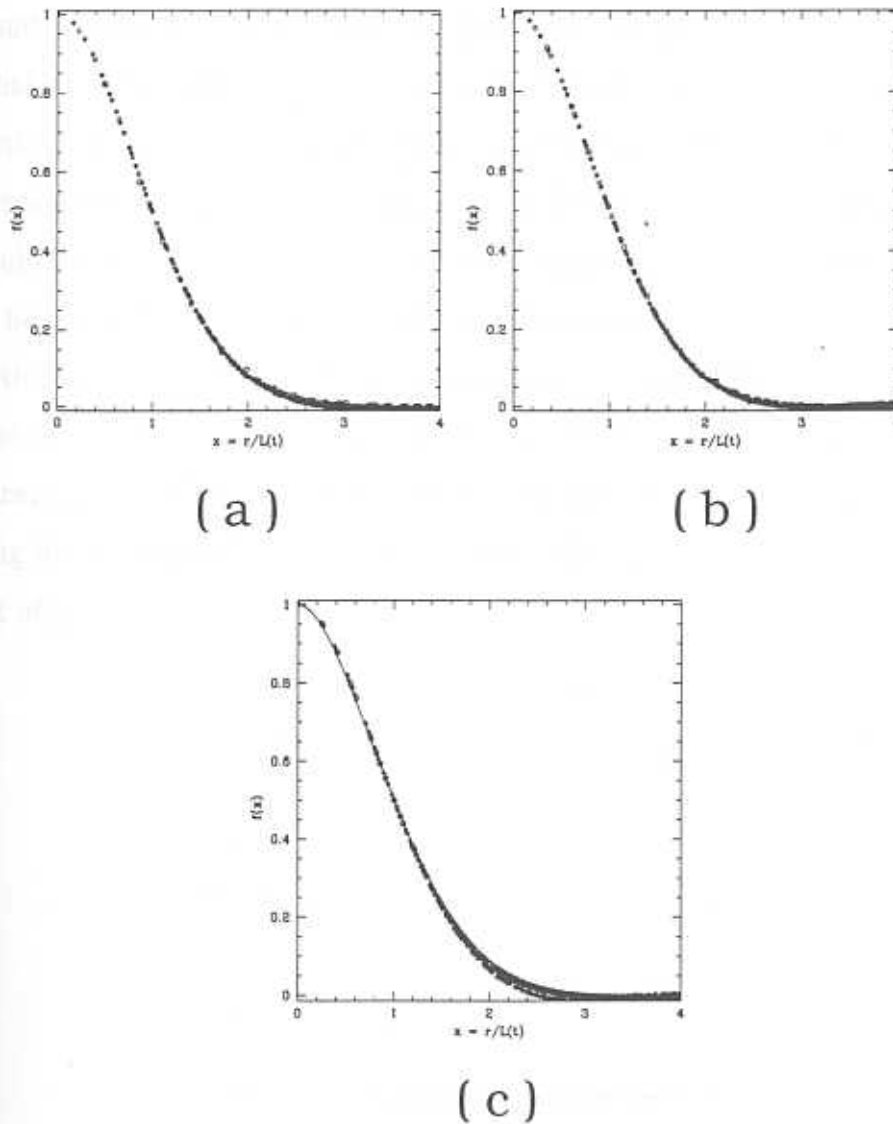


Figure 2.2: (a) The scaling function $f(x)$ versus $x \equiv r/t^{1/2}$ for $g = 0$. Data taken at $t = 1000$ (\circ), $t = 5000$ (\triangle) and $t = 10000$ (\star). Error bars are smaller than the size of symbols. (b) $f(x)$ versus $x \equiv r/t^{1/2}$ for $g = 1$. Data taken at $t = 2000$ (\circ), $t = 5000$ (\triangle) and $t = 10000$ (\star). Error bars as in Fig. 2.2a. (c) $f(x)$ versus $x \equiv r/t^{1/2}$ for different values of g ($g = 0$ (\circ), 0.5 (\square), 1 (\triangle), 2 (\star)). The data for $g = 2$ was obtained from a simulation on a 50^3 lattice averaged over 7 configurations. The continuous curve is the approximate analytical form described in the text [9].

At larger values of g , finite size effects become very prominent. This can be seen from the form of the late time $C(r, t)$ for $g = 5$ (Fig. 2.3), simulated on a 50^3 lattice averaged over 7 initial configurations. The correlation function crosses zero at large r , dips through a

minimum, and then asymptotically goes to zero (ofcourse $\int dr C(r, t) > 0$). It is clear from the figure that at these times, $C(r/L(t))$ for $g = 5$ would be qualitatively different from the scaling function of Fig. 2.2c. However notice that the dip decreases with increasing time. This would suggest that the dip might disappear at late times, and that the resulting scaling function would be identical to Fig. 2.2 c. We note that in order to make such a claim, great care should be taken to avoid finite size effects. The tail of the autocorrelation function gets affected by the finite size of the lattice, earlier than the part of $C(r, t)$ used to calculate z . The decrease in the dip at $g = 5$ can only be perceived when the system size is large. In the next paragraph we will argue that this dip is a pre-asymptotic feature and disappears in the scaling limit. This will allow us to conclude that the scaling function $f(x)$ is indeed independent of g .

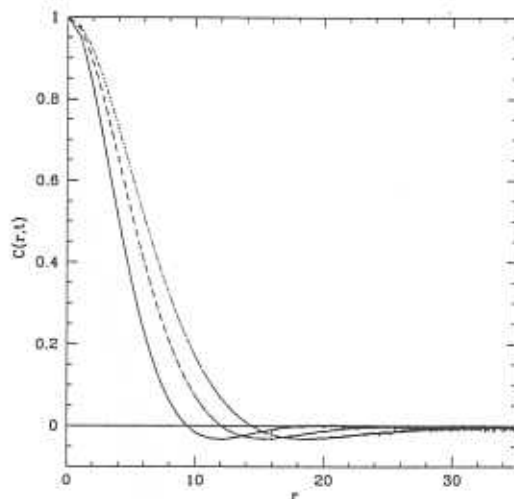


Figure 2.3: The correlation function $C(r, t)$ versus r for $g = 5$ at various times ($t = 3000$ (—), $t = 5000$ (- · -), $t = 7000$ (···)). Note that the dip gets smaller as time progresses. Error bars as in Fig.2.2 a.

At very late times, the order parameter field has totally relaxed with respect to defect cores. Pre-asymptotic configurations typically consist of spin-wave excitations interspersed between slowly moving defects separated by a distance $L(t) \gg \xi_{core}$, the size of the defect core. Decomposing $\vec{\phi}$ into a singular (defect) part $\vec{\phi}_{sing}$ and a smooth (spin-wave) part $\vec{\phi}_{sm}$, we calculate the pre-asymptotic correlation function within a perturbative analysis

(Appendix IIB). The computed correlation function exhibits a dip at $r^2/t \sim (1 + g^2)/g$, which disappears algebraically in time. The amplitude of this dip increases with increasing g . The dip eventually goes away with a relaxation time that scales as,

$$\tau(g) = t_*(1 + g^2), \quad (2.10)$$

where t_* is the time at which the $g = 0$ correlation function first exhibits scaling. The crossover time $\tau(g)$ is estimated to be (taking $t_* = 1000$ for the 40^3 system) — $\tau(g = 1) = 2000$, $\tau(g = 2) = 5000$ and $\tau(g = 5) = 26,000$. The crossover times for $g \geq 5$ are much larger than the largest time reached in our simulation ! Figure 2.4 is a plot of pre-asymptotic $C(r, t) = C_{sing} + C_{sm}$ at a fixed time, where C_{sing} is given by the BPT form [9] and C_{sm} takes the form derived in Appendix IIB. Two adjustable parameters related to the length scale and the amplitude of the spin-wave have been tuned to obtain excellent fits to the numerical data. Based on these arguments we conclude that the scaling function $f(x)$ is independent of g .

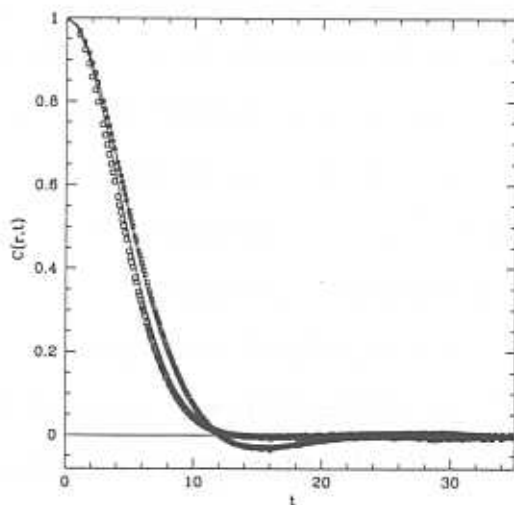


Figure 2.4: Pre-asymptotic $C(r, t)$ for $g = 1$ and 5 (bold lines) calculated in Appendix IIB. Note the excellent fit to the simulation data for $g = 1$ (\circ), $g = 5$ (\square).

We now compute the autocorrelation function $C(0, 0, t)$ and extract the exponent λ (see Eq. (2.8)). The time t ranges from 4000 – 16000 for the 60^3 lattice (averaged over 50 initial configurations), well into the scaling regime for the equal-time correlator.

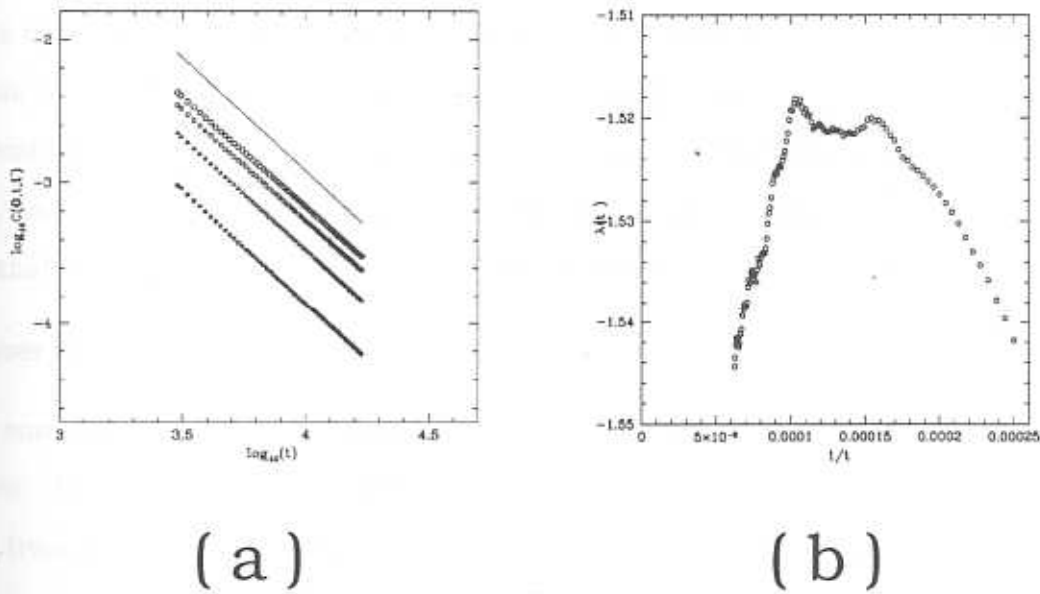


Figure 2.5: (a) log-log plot of the autocorrelation function $C(0,0,t)$ versus t for $g = 0$ (\circ), 0.5 (\square), 1 (\triangle), 2 (\star). The straight line is a fit $A(t+t_0)^{-\lambda/2}$, where λ has been chosen to be the Mazenko value 1.587. (b) Effective λ as a function of $1/t$ for $g = 0$.

Figures 2.5a are log-log plots of $C(0,0,t)$ versus t for various values of $g = 0, 0.5, 1, 2$. It is difficult to give a precise value of the decay exponent λ , since as can be seen from Fig. 2.5b, the “effective” λ varies by about 3% over half a decade. However it is evident from the bold line in Fig. 2.5a, which corresponds to $A(t+t_0)^{-\lambda/2}$ (A and t_0 are varied to give the best fit to the overall data), that the value of λ is independent of g . A fit to each data set for a given g , obtains the following values for the exponent λ — $\lambda(g=0) = 1.526 \pm 0.007$, $\lambda(g=0.5) = 1.521 \pm 0.008$, $\lambda(g=1) = 1.55 \pm 0.01$, and $\lambda(g=2) = 1.55 \pm 0.02$. The numerical values listed above can be compared to the theoretically estimated value of 1.587 [10] when $g=0$ using the approximate closure scheme due to Mazenko [11] (we will discuss this approximation in great detail in Sect. 2.1.3. We see that to within error bars the values of λ are independent of g and equal to the value at $g=0$. Note that these values obey the precise lower bound $\lambda > d/2$ derived in Ref. [12].

Before ending this section, we comment on finite size effects which clearly set in at later times. As discussed in [12], finite size effects will be relevant when the spread in

$C(0,0,t)$ (given by $\Delta C(0,0,t) \sim N^{-3/2}$) is of order $C(0,0,t)$ itself. This will happen when $L^{-\lambda} \sim N^{-3/2}$. The fact that the numerically computed λ increases marginally with g , indicates that finite size effects are more apparent for larger g . This is consistent with our discussion on the effects of finite size on equal-time correlators.

We end this section with a firm conclusion based on our careful numerics. The exponents z and λ and the scaling function $f(x)$ are seen to be independent of the torque g . This implies that the torque is irrelevant for the nonconserved dynamics at the $T = 0$ fixed point.

B. Conserved Dynamics, $\mu = 2$

We now turn our attention to a numerical solution of the Langevin equation for the conserved dynamics. As usual we evaluate the correlation functions Eqs. (2.5), (2.6) for values of g ranging from 0 to 1. The simulation is done on a 50^3 simple cubic lattice and measured quantities are averaged over 5 – 10 initial configurations. The initial configurations of spins in the disordered phase are chosen such that $\vec{\phi}(t = 0)$ is uniformly distributed within the volume of a unit sphere centered at the origin. $\vec{\phi}$ at different spatial points are uncorrelated. As stated earlier, standard scaling with a single length scale $L(t)$ holds at late times. We demonstrate the existence of a single length scale explicitly in Appendix IIA.

Figure 2.6 is a scaling plot of $C(r,t)$ versus $r/L(t)$ for various values of the parameter g , where $L(t)$ is extracted from the first zero of $C(r,t)$. Note that the scaling function for $g = 0$ is very different from those for $g > 0$; further the $g > 0$ scaling functions do not seem to depend on the value of g . This suggests that the dynamics crosses over to a new ‘torque-driven’ ZFP. This is also revealed in the value of the dynamical exponent z . In Fig. 2.7a, a plot of $L(t)$ versus t gives the expected value of $z = 4$ when $g = 0$ (see Sect. 1.1). For $g > 0$, we see a distinct crossover from $z = 4$ when $t < t_c(g)$ to $z = 2$ when $t > t_c(g)$. The crossover time $t_c(g)$ decreases with increasing g . The same z exponent and crossover are obtained from the scaling behaviour of the energy density ε defined by Eq. (2.9) (Fig. 2.7 b).

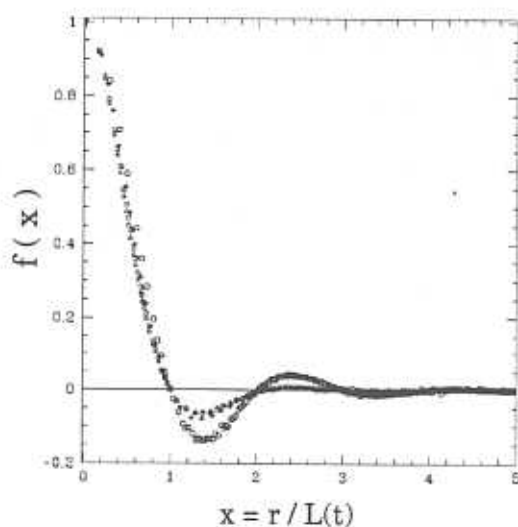
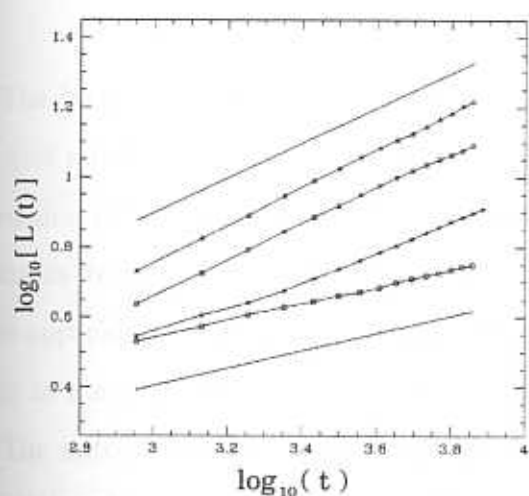
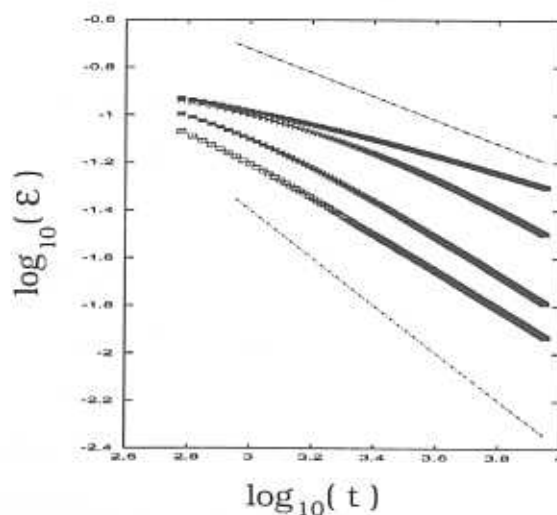


Figure 2.6: Scaling plot of $C(r, t)$ for $N = 50^3$. The scaling function $f(x)$ changes as g is varied from $g = 0$ (\circ) to $g \neq 0$ ($g = 0.1$ ($*$), 0.3 (\triangle), 0.5 (\square)).



(a)



(b)

Figure 2.7: (a) log-log plot of $L(t)$. At $g = 0$ ($+$) we find that $z = 4$ (line of slope 0.5 drawn at the top for comparison). At $g \neq 0$ ($g = 0.1$ (\times), 0.3 ($*$), 0.5 (\square)), z crosses over from 4 to 2 (line of slope 1.0 drawn at the bottom). (b) log-log plot of $L(t)$. At $g = 0$ ($+$) we find that $z = 4$ (line of slope 0.5 drawn at the top for comparison). At $g \neq 0$ ($g = 0.1$ (\times), 0.3 ($*$), 0.5 (\square)), z crosses over from 4 to 2 (line of slope 1.0 drawn at the bottom).

To ensure that our results are not affected by finite size, we compute 3 relevant time scales (shown in Table 1 below) — (1) $t_c(g)$, the crossover time from a $t^{1/4}$ to a $t^{1/2}$ growth, (2) $t_s(g)$, the time at which asymptotic scaling begins, (3) t_{fs} , the time at which finite size effects become prominent. It is clear from the table that $t_c < t_s < t_{fs}$, as it should be if our data is to be free of finite size artifacts. A general rule-of-thumb is that finite size effects start becoming prominent when the domain size gets to be of order 1/3 the system size, and we see from Table 1 that L_{max}/N is comfortably less than 1/3.

Table 1

g	$t_c(g)$	$t_s(g)$	t_{fs}	L_{max}/N	f_{min}
0	—	900	> 7650	1/10 at $t = 7650$	-0.14
0.1	3150	≥ 7650	> 7650	1/6 at $t = 7650$	-0.08
0.3	900	1350	> 7650	1/4 at $t = 7650$	-0.06
0.5	450	900	4950	1/3.7 at $t = 4950$	-0.06

The last column in Table 1 shows f_{min} , the value of the scaling function evaluated at the first minimum as a function of g . It is easy to see why $f_{min}(g) < f_{min}(g = 0)$, since the precession of the spins about the local molecular field would cause spins from neighbouring 'domains' to be less anti-correlated. This is borne out by computing the spin-wave correction to an approximate form of $C(r, t; g = 0)$ (given in Eq. (2.31); more on this later) to quadratic order in the spin-wave amplitude (see Appendix IIB).

The autocorrelation function $A(t)$ is calculated for $g = 0, 0.2$ and 0.3 (Fig. 2.8a). The simulations have been done on a lattice of size 60^3 and averaged over 10 initial configurations (we have to average over a large number of initial configurations for smoother data). The λ exponent extracted from the asymptotic decay of $A(t)$ clearly suggests a crossover from $\lambda = 2.2$ to $\lambda \approx 5.05$. The numerical determination of λ is subject to large errors [12, 7] and is very sensitive to finite size effects, and so we have to go to very late times and hence large system sizes to obtain accurate results.

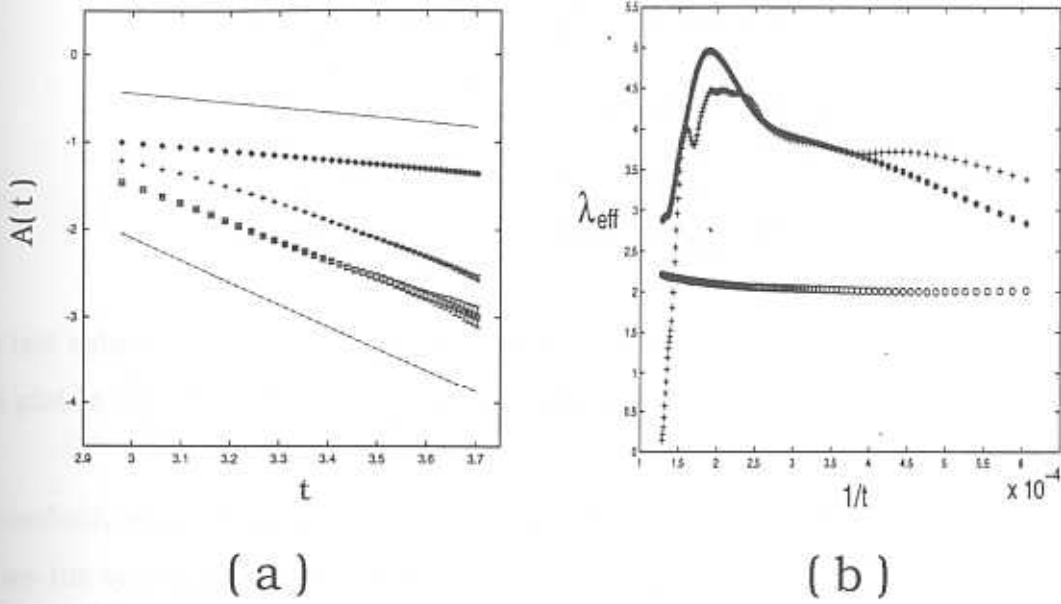


Figure 2.8: (a) log-log plot of $A(t)$ vs t for $g = 0(\diamond)$, $0.2(+)$, $0.3(\square)$. Solid line on top has the form $a/t^{\lambda/z}$ where $\lambda = 2.19$ and $z = 4$ (corresponding to the $g = 0$ fixed point) while the one below has a $\lambda = 5.05$ and $z = 2$ (corresponding to the 'torque-driven' fixed point). (b) λ_{eff} versus $1/t$ for $g = 0.0(\circ)$, $0.2(*)$, $0.3(+)$. Finite size effects set in when λ_{eff} starts becoming a decreasing function of time. For $g = 0$ we do not see any finite size effects in λ within our simulation times.

To make sure that we collect asymptotic data untainted by finite size, we compute two time scales (Table 2) — (i) $t_{fit}(g)$, the time beyond which $A(t)$ can be fit with a power law $a(t+t_0)^{-\lambda/z}$, (ii) t_{fs} , the time at which finite size effects on $A(t)$ become prominent. The crossover time t_c is displayed in Table 1.

To determine t_{fs} we plot an effective exponent $\lambda_{eff} = -td(\log A(t))/dt$ as a function of $1/t$. The derivative is calculated numerically with a $\delta t = 15$ (in units of the time discretisation Δt). We see from Fig. 2.8b, that at late times $t > t_{fs}$, λ_{eff} crosses over to being a decreasing function of time, clearly a finite size effect. This estimate of t_{fs} is not very sensitive to the choice of δt , changing by 1% (for $g = 0.2$) or 3.5% (for $g = 0.3$) as δt changes by 5 units. Note that finite size effects in $A(t)$ appear earlier than in $C(r, t)$.

It is seen from Table 2 that $t_{fit} < t_{fs}$, as it should if we are to have an accurate determination of λ .

Table 2

g	$t_{fit}(g)$	t_{fs}	λ
0.0	900	> 9000	$2.199 \pm 7.5 \times 10^{-3}$
0.2	1500	5376	$5.100 \pm 6.1 \times 10^{-3}$
0.3	900	5181	$5.010 \pm 2.3 \times 10^{-3}$

The last column of Table 2 lists the value of λ as a function of g . The data presented and the plot in Fig. 2.8a clearly support a crossover from $\lambda = 2.2$ at $g = 0$ to $\lambda = 5.05$ at $g \neq 0$.

To conclude, we have just seen that the torque term is relevant for the conserved dynamics and drives the system to a new $g \neq 0$ fixed point characterised by $z = 2$, $\lambda \approx 5$ and a new scaling function $f(x)$.

• Crossover Scaling Phenomenon

It is clear from the last section, that though the asymptotic dynamics is governed by the new ‘torque-driven’ fixed point, the dynamics at earlier times $t \ll t_c$ follows the $g = 0$ behaviour. This suggests that the dynamics for arbitrary g may be analysed as a crossover from the $g = 0$ fixed point, characterized by $z = 4$ and $\lambda \approx 2$, to the torque-driven fixed point where $z = 2$ and $\lambda \approx 5$.

A simple scaling argument encourages us to think of such a crossover scenario. On restoring appropriate dimensions, the (noiseless) dynamical equation Eq.(2.3) can be rewritten as a continuity equation,

$$\partial \vec{\phi}(\mathbf{r}, t) / \partial t = -\nabla \cdot \vec{j} \quad (2.11)$$

where the “spin current” is

$$\vec{j}_\alpha = -\Gamma \left(\nabla \frac{\delta F[\vec{\phi}]}{\delta \phi_\alpha} + \frac{\Omega_L}{\Gamma} \epsilon_{\alpha\beta\gamma} \phi_\beta \nabla \phi_\gamma \right). \quad (2.12)$$

From a dimensional analysis where we replace j_α by the ‘velocity’ dL/dt , we find

$$\frac{dL}{dt} = \Gamma \frac{\sigma}{L^3} + \Omega_L \frac{\sigma M}{L}, \quad (2.13)$$

where M , σ and Γ are the equilibrium magnetisation, surface tension and spin mobility respectively. Beyond a crossover time given by $t_c(g) \sim (\Gamma/M_0\Omega_L)^2 \sim 1/g^2$, simple dimension counting shows that the dynamics crosses over from $z = 4$ to $z = 2$ in conformity with our numerical simulations.

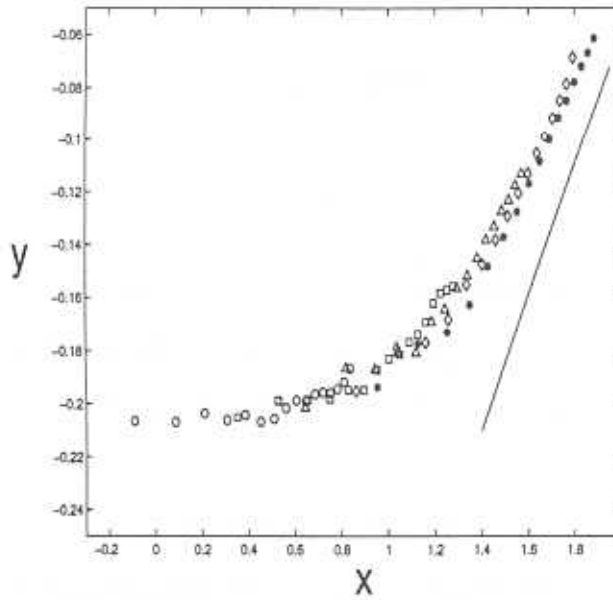


Figure 2.9: Scaling plot of $y = L(t, g)/t^{1/4}$ versus $x = tg^2$ for $g = 0.03(\circ)$, $0.05(\square)$, $0.07(\triangle)$, $0.09(\diamond)$, $0.10(*)$. The solid line of slope 0.25 is the theoretical estimate of the asymptotic form of the scaling function as $x \rightarrow \infty$ (see text).

The crossover physics is best highlighted by numerically demonstrating crossover scaling of the domain size $L(t, g)$ and the correlation functions $C(r, t, g)$ and $A(t, g)$.

For instance, the *mean field* Eq. (2.13) suggests that the domain size obeys the scaling form $L(t, g) = t^{1/4} s_m(tg^2)$ where the crossover function $s_m(x)$ is determined from the transcendental equation,

$$x^{1/2} s_m(x) - \ln(1 + x^{1/2} s_m^2) - 2x = 0. \quad (2.14)$$

We shall now argue (and then confirm numerically) that the above scaling form holds in general. Scaling $r \rightarrow r/b$, $t \rightarrow t/b^z$ and $g \rightarrow g/b^{y_g}$, scales the domain size by

$$L(t, g) = b s(t/b^z, g/b^{y_g}), \quad (2.15)$$

where y_g is the scaling dimension of g . We choose b such that $t/b^z = 1$, which implies

$$L(t, g) = t^{1/z} s(g/t^{y_g/z}). \quad (2.16)$$

Setting $g = 0$ gives $L(t, g = 0) = t^{1/z} s(0)$, telling us that $z = 4$. Thus the scaling form Eq. (2.16) is governed by the $g = 0$ fixed point. We therefore need to evaluate y_g at this $g = 0$ fixed point. We determine y_g by noting that the g contribution to Eq. (2.3) is given by,

$$\begin{aligned} \frac{d\vec{\phi}}{dt} &\sim g\vec{\phi} \times \delta F[\vec{\phi}]/\delta\vec{\phi} \\ &= g\vec{\phi} \times \vec{\mu} \\ &\sim g/L^2, \end{aligned} \quad (2.17)$$

where the last relation is obtained by requiring local equilibrium (Gibbs-Thompson) on the chemical potential $\vec{\mu}$. Thus equating dimensions, $[g] = [t^{-1}][L^2] = [L^{-z+2}] = [L^{-2}]$ leads to $y_g = -2$. The crossover scaling form for the domain size can now be read out from Eq. (2.16),

$$L(t, g) = t^{1/4} s(g^2 t). \quad (2.18)$$

The $x \rightarrow \infty$ asymptote of $s(x)$ can be obtained by demanding that we recover the ‘torque-driven’ fixed point behaviour; this forces $s(x \rightarrow \infty) \sim x^{1/4}$.

We will now check whether this crossover scaling form emerges from our Langevin simulation. If the above proposal is true, then we should expect a data collapse onto the scaling curve $s(x)$ when $L(t, g)/t^{1/4}$ is plotted against tg^2 . Figure 2.9 shows the results of the numerical simulation — the data collapse is not good away from the asymptotic regimes. To see a better collapse of the data away from either fixed point, it is necessary to include corrections to scaling.

Corrections to scaling come from two sources — (i) finite time effects and (ii) nonlinear corrections to the scaling fields [13]. Finite time corrections can be incorporated by introducing finite-time shift factors $t \rightarrow t - t_0$, which can be neglected in the $t \rightarrow \infty$ limit. Nonlinear corrections to scaling are incorporated by constructing a nonlinear, analytic function $\tilde{g}(g)$ of the physical fields g , such that it reduces to g in the limit $g \rightarrow 0$. The simplest choice for such a function is

$$\tilde{g}(g) = \frac{g + cg^2}{1 + cg^2}, \quad (2.19)$$

leading to a nonlinear scaling variable

$$\tilde{x} = (\tilde{g}(g))^2(t - t_0). \quad (2.20)$$

The data plotted with respect to this nonlinear scaling variable shows a much better collapse (Fig. 2.10) when c is chosen to be around -1.5 (in the Figs. 2.10 - 2.12, the finite time shift t_0 was taken to be 0). The simple 'mean-field' estimate $s_m(\tilde{x})$ plotted for comparison (Eq. (2.14)), is exact only at the asymptotes.

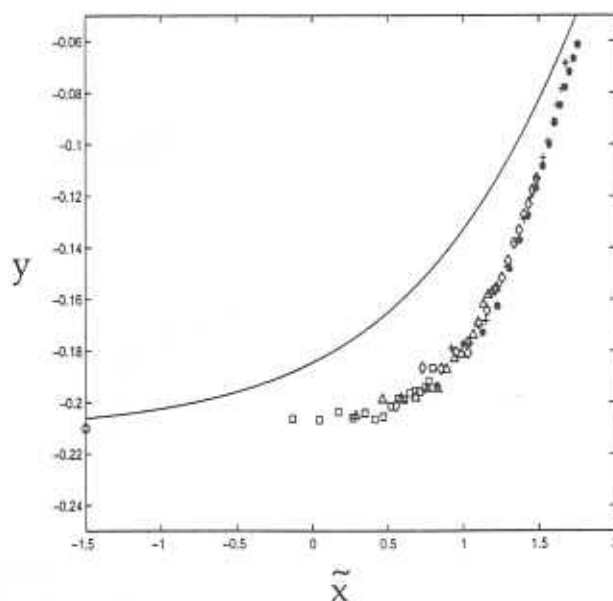


Figure 2.10: Plot of $y = L(t, g)/(t - t_0)^{1/4}$ versus \tilde{x} for $c \approx -1.5$. The point \circ on the y axis, represents the value of y as $\tilde{x} \rightarrow 0$.

We have seen from the discussion in the last section that the numerically computed equal-time correlation function $C(r, t, g)$ is unaltered when scaled with the domain size L — this suggests the following scaling behaviour

$$C(r, t, g) = f(r/L, t/L^z, g/L^{y_g}), \quad (2.21)$$

where z is the dynamical exponent at the $g = 0$ fixed point and y_g is the scaling dimension of g . The domain size L is given by the scaling form Eq. (2.18). This readily leads to a two variable scaling [14],

$$C(r, t, g) = f\left(\frac{r}{t^{1/4}}, tg^2\right), \quad (2.22)$$

with scaling variables $\rho = r/t^{1/4}$ and $x = tg^2$. When $x = 0$ and $x \rightarrow \infty$ then $f(\rho, x) = f_0(\rho)$ and $f(\rho, x) = f_T(\rho)$ respectively, where $f_0(\rho)$, $f_T(\rho)$ are the asymptotic scaling functions at $g = 0$ and $g \neq 0$. Again in terms of the nonlinear scaling variables \tilde{x} and $\tilde{\rho} = r/(t - t_0)^{1/4}$, we find a very good collapse of the data when c is chosen to be around -1.2 (Fig. 2.11).

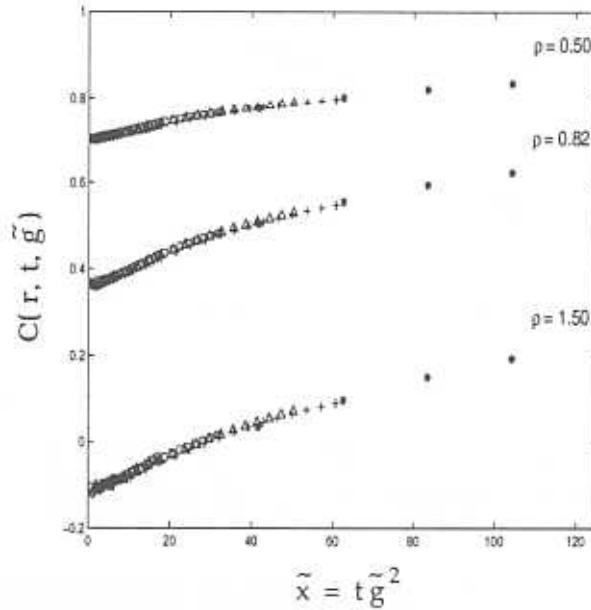


Figure 2.11: $C(r, t, g)$ versus \tilde{x} at $\tilde{\rho} = 0.50, 0.82$ and 1.50 for $g = 0.03(\circ), 0.05(\diamond), 0.07(\square), 0.09(\triangle), 0.1(+), 0.3(*)$ showing data collapse for $c \approx -1.2$.

Similar arguments suggest that the autocorrelation function satisfies the scaling form

$$A(t, g) = t^{-\lambda_0/4} a(tg^2), \quad (2.23)$$

where $a(x = 0) = a_0$ is a constant, and $\lambda_0 \approx 2.2$ is the value of the autocorrelation exponent at $g = 0$. As $x \rightarrow \infty$, the scaling function $a(x)$ should asymptote to $a(x) \sim x^{\lambda_0/4 - \lambda_T/2}$, where $\lambda_T \approx 5.05$ is the exponent at the 'torque-driven' fixed point. This expectation is borne out by the numerical simulation (Fig. 2.12), where we have again used the nonlinear scaling variable \tilde{x} for better collapse.

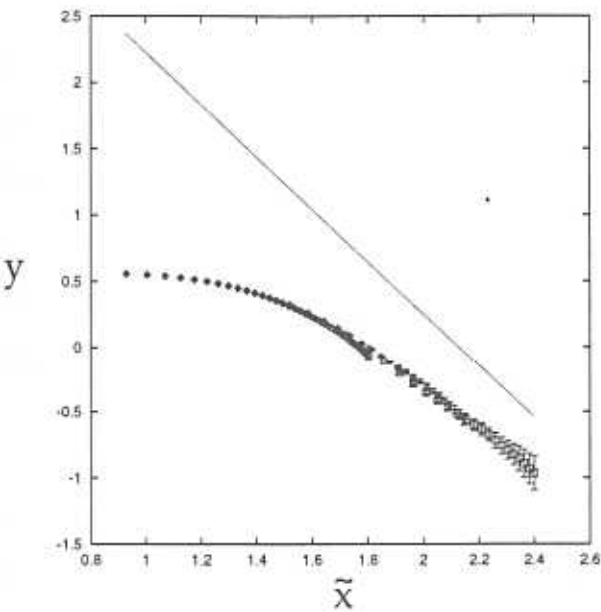


Figure 2.12: log-log plot of $y = A(t, \tilde{g})/t^{-\lambda_0/4}$ versus \tilde{x} for $g = 0.1(\diamond)$, $0.2(+)$, $0.3(\square)$ showing data collapse for $c \approx -1.1$. The scaling function asymptotes to a line of slope $\lambda_0/4 - \lambda_T/2 = -1.95$ as $\tilde{x} \rightarrow \infty$.

Our discussion on the crossover phenomenon clearly indicates that for times $t \ll t_c(g) \sim 1/g^2$, the dynamics is affected by the $g = 0$ fixed point while for $t \gg t_c(g) \sim 1/g^2$, it follows the ‘torque-driven’ fixed point. A nonlinear scaling form connects the unstable $g = 0$ fixed point to the stable one. The crossover scaling analysis suggests the following renormalisation group flow diagram :



Figure 2.13: Flow diagram showing fixed points and flows on the $\tilde{x} = t\tilde{g}^2$ line.

To understand the crossover and to arrive at an analytical theory for finite g , we ask whether we could *perturb* about either the $g = 0$ or $g \neq 0$ fixed points. In the next section we investigate the latter.

2.1.2 Perturbation about $g \neq 0$ fixed point: The Pure Torque Model

Our study suggests that the late time dynamics of the conserved model is dominated by precession, and consequently the dissipation term is irrelevant at the new fixed point. Does this imply that we could drop the dissipation term from the equations of motion and still recover the same late-time behaviour? If so, can we use dissipation as a small parameter to perturb about this new fixed point? To answer this we study the dynamics of the pure torque model (inertial dynamics) given by

$$\frac{\partial \vec{\phi}}{\partial t} = g \vec{\phi} \times \nabla^2 \vec{\phi}. \quad (2.24)$$

This equation of motion has the following conserved quantities — (a) total energy, $\varepsilon = V^{-1} \int d\mathbf{r} (\nabla \vec{\phi})^2$ (unless there is a contribution coming from the surface term $S_t = V^{-1} \int d\sigma \vec{\phi} \cdot (\nabla^2 \vec{\phi} \times \nabla \vec{\phi})$ due to a choice of boundary conditions); (b) total spin, since the right hand side can be written as a divergence of a current; and (c) magnitude of the local spin $\vec{\phi} \cdot \vec{\phi}$.

Since the dynamical equation conserves energy (microcanonical evolution), it would be impossible to arrive at an ordered state starting from a disordered one. Therefore our strategy is to *prepare an initial configuration* with a nonzero correlation length. This we do in the following way — we start with an initial paramagnetic configuration (as in Sect. 2.1.1 B) and quench to zero temperature; the spins evolve via Eq. (2.3) upto a time τ ($\tau \ll t_*$, the time when asymptotic scaling begins). The resulting spin configuration has a finite correlation length. This is the initial configuration for our microcanonical dynamics. In our numerical simulations we have computed the spatial correlation length of this initial configuration to be $\xi \sim 3$.

Since the initial configuration is taken from a paramagnetic state, it will contain a large number of defects and anti-defects. Energetics forces the magnitude of $\vec{\phi}$ to vanish at defect (anti-defect) cores [2]. Since the dynamical equation Eq. (2.24) conserves the magnitude of the local spin, the locations of defects defined by $|\vec{\phi}| = 0$ remain static under time evolution.

The resulting inertial dynamics is very different from the dynamics which includes dissipation. Defects do not move, spin-waves merely scatter off these stationary defects which are located randomly in space. Apart from this “quenched” random scattering, spin-waves

scatter off each other. A field theoretic analysis of this problem is hard; we therefore resort to a numerical solution with a discretisation scheme as discussed below.

Any kind of discretisation needed to numerically solve Eq. (2.24) will affect the conservation laws, especially the conservation of the magnitude of the local spin. We employ a second order discretisation scheme, with $\Delta x = 2.5$ and $\Delta t = 0.2$, to ensure that the magnitude of $\vec{\phi}$ remains unchanged to $O((\Delta t)^2)$. We have computed the boundary contribution S_t and have found it to be of order 10^{-7} (zero in our single precision calculation!). As we verify in Fig. 2.14, the second order numerical scheme ensures the constancy of the energy density ε to $O((\Delta t)^2)$.

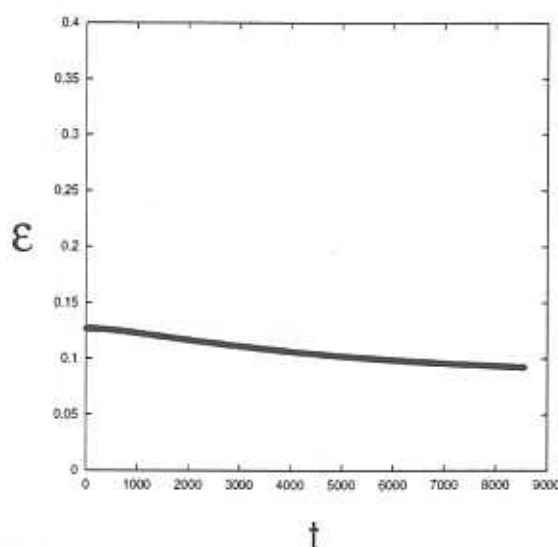


Figure 2.14: Plot of ε vs t to show that ε changes only to order $(\Delta t)^2$ over the timescale.

We solve Eq. (2.24) numerically on a 50^3 lattice for a single value $g = 0.05$. This will suffice to illustrate our point. We first compute the equal time correlation function $C(r, t)$ averaged over 5 initial configurations. The first zero of $C(r, t)$ provides a length scale $L(t)$, which we find grows as $t^{1/2}$ after $t \geq 3150$. However $C(r, t)$ does not seem to exhibit dynamical scaling within our simulation times $t \leq 8550$. The scaling violations occur in the range $0 < x < 1$, where $x \equiv r/L(t)$ (Fig. 2.15). The violation of scaling in $C(r, t)$ at small r is a consequence of the conservation laws [15]. The value of the correlator at the origin,

$C(0, t)$, cannot change with time, since $\vec{\phi} \cdot \vec{\phi}$ is a constant of motion. Further, the curvature at the origin, $\nabla^2 C(0, t)$ cannot change with time, since this is essentially the negative of the energy density $-\langle(\nabla\vec{\phi})^2\rangle$ (as can be seen on Fourier transformation), again a constant of motion.

Since both the value of $C(r, t)$ and its curvature are fixed at $r = 0$, conventional scaling of the form $C(r, t) = f(r/L(t))$ cannot hold at small r . However at large r (i.e. $x > 1$) we recover scaling and the scaling form is the same as the scaling function when both dissipation and torque are present in the conserved dynamics.

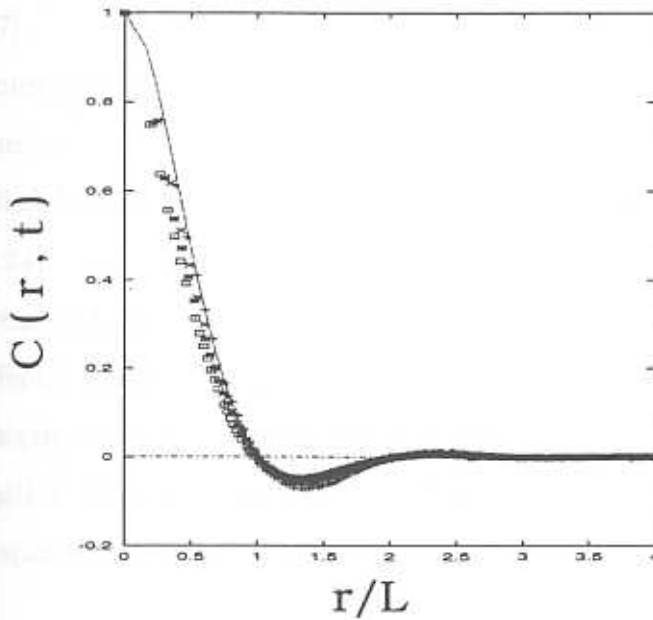


Figure 2.15: $C(r, t)$ plotted against $r/L(t)$ at times $t = 4050(\diamond)$, $4950(+)$, $6750(\square)$ and $8550(\times)$. The scaling function $f(x)$ (connected line with \triangle) for the conserved dynamics with dissipation and torque is shown for comparison. Error bars are of the order of symbol sizes. It is seen that the data for $x < 1$ do not show scaling but for $x > 1$ we recover scaling and the scaling function is same as $f(x)$.

This suggests that over these large length scales, the spins become more and more ordered as time progresses. Thus 'coarsening' occurs in spite of the dynamics being microcanonical where the energy is conserved ! Since the dissipative dynamics with torque (canonical dynamics) ensures that the system will approach equilibrium, this correspondence of the scaling function suggests that the long wave-length spin waves $\vec{\phi}_{\mathbf{k}}$ for $|\mathbf{k}| \ll 2\pi/L$ will eventually equilibrate under the pure torque dynamics. The higher wave-vector modes $\vec{\phi}_{\mathbf{k}}$ for

$|\mathbf{k}| > 2\pi/L$ act as a 'heat bath' – the nonlinear coupling between various $|\mathbf{k}|$ modes gives rise to a flow of energy from the higher length scales to lower. This is analogous to the microcanonical ordering dynamics of a quenched Bose Gas [16]. The 'heat bath' provided by the high \mathbf{k} modes are a source of dissipation and 'noise' (whose statistics may be non-trivial). In our problem we have tentatively identified the mechanism of 'noise' generation with the multiple scattering of the high \mathbf{k} spin-waves off the randomly placed but stationary defects. At length scales much larger than the typical separation between defects, these multiple scattering events mimic a 'noise' (examples of such multiple scattering events giving rise to a 'non-thermal' noise at large length scales can be found in, for example, sedimentation of colloidal particles [17]).

We perform two numerical tests to vindicate the above claim (many more tests are needed to establish this rigorously) :

(i) We remove all defects from the initial configurations and then allow the spin-waves to evolve via Eq. (2.24).

Our numerical study (Fig. 2.16) suggests that starting from an initial smooth spin configuration (no defects) $C(r, t)$ obtained by solving Eq. (2.24), does not show any signs of coarsening at any length scale. The spins settle into some stationary state which is not an equilibrium configuration. We therefore conclude that the quenched defects are responsible for equilibration of spin-waves whose wavelength $k^{-1} \gg L$, the typical distance between defects.

(ii) We study the pure torque dynamics in one dimension (1D) where there are no topological defects.

We solve Eq. (2.24) in 1D on a regular lattice of size $L = 200$ starting from a paramagnetic configuration (*i.e.* total magnetisation is zero and total energy is E_0) with a spatial correlation length $\xi \sim 4$. Plots of $C(r, t)$ at different times (Fig. 2.17 a) show that after coarsening for a short while, the spins settle into a steady state with a correlation function $C_s(r, E_0)$. Comparison of this steady state correlation function with the equilibrium correlation function $C_{eq}(r, E_0)$ evaluated at E_0 in the constant magnetisation ensemble, shows that they are very different (Fig. (2.17)).

The fact that the $d = 1$ pure torque dynamics does not lead to equilibration should come as no surprise, since the equation of motion allows for solitonic solutions [8, 9] which give rise to infinite number of conserved quantities [9] (we will return to this aspect in Chapter 4).

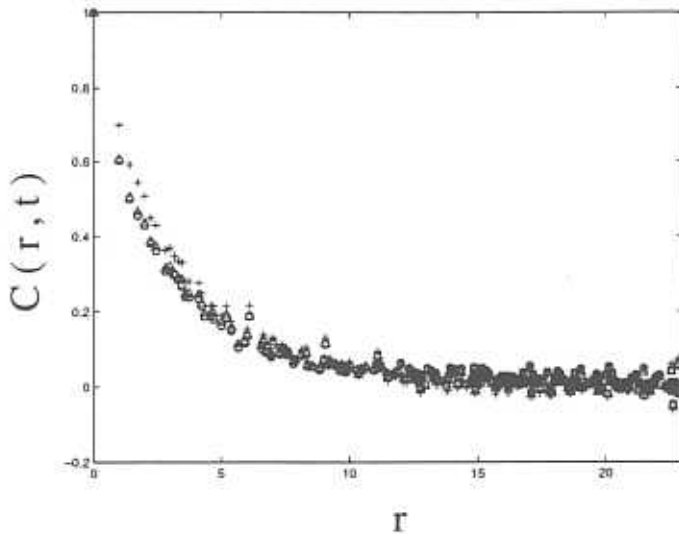


Figure 2.16: $C(r, t)$ vs r at different times following the dynamics (Eq. (2.24)) starting with initial configurations without defects and a correlation length $\xi \sim 5$. Simulations are done on a $(50)^3$ lattice averaged over 5 initial configurations. Plots are displayed for $t = 0(+)$, 5400(Δ), 7200(\square) and 9000(\circ) showing clearly that the spins settle into a stationary state after $t \geq 5400$. There is no sign of coarsening unlike the dynamics in the presence of defects (Fig. 2.15).

It is therefore clear that not all $\vec{\phi}_{\mathbf{k}}$ modes reach the scaling regime of the ‘torque-driven’ fixed point. Dissipation, though irrelevant, seems necessary for the spin system to access the ‘torque-driven’ fixed point. One can understand this intuitively in the following way. Starting from a paramagnetic configuration, where defects and anti-defects are seeded randomly in space, the pure torque dynamics ensures that these defect cores (located by the zeroes of $\vec{\phi}$) remain stationary under time evolution; *i.e.* the defect mobility $\Gamma_D = 0$. The resulting dynamics consists of spin-waves scattering off these randomly distributed immobile defects and off each other. This picture changes dramatically even if a minute amount of dissipation is present, the defects now move slowly and annihilate each other allowing the spin system to reach its true asymptotic configurations. Hence a nonzero defect mobility Γ_D (proportional

to Γ) is necessary to reach the scaling regime. Only *after* the spin system has reached the scaling regime, we may set $\Gamma_D = 0$. Such an irrelevant variable is known as a dangerously irrelevant variable [20, 21].

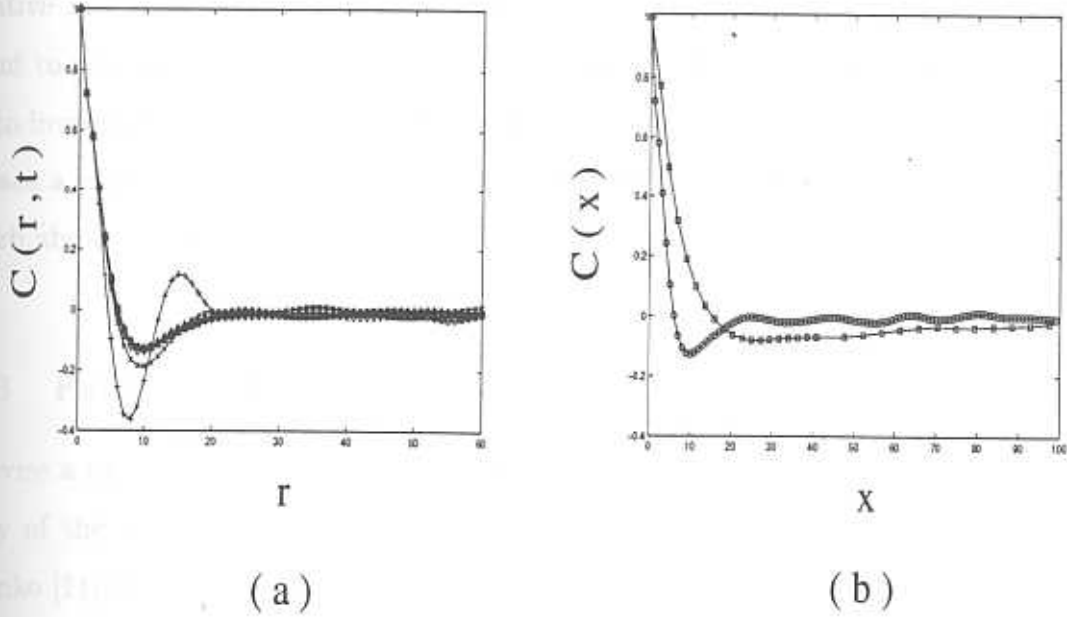


Figure 2.17: (a) Plot of $C(r, t)$ vs r at different times when the system evolves according to a pure torque dynamics (Eq. (2.24)) in $d = 1$. Simulation is done on a regular lattice of size $L = 200$ with $\Delta x = 1$, $\Delta t = 0.001$ and $g = 0.1$. Data are averaged over 100 initial configurations. Plots of $C(r, t)$ at $t = 0(+)$, $20 \times 10^4(\times)$, $50 \times 10^4(\diamond)$, $70 \times 10^4(\Delta)$, $75 \times 10^4(\square)$, $80 \times 10^4(\circ)$ show that after some initial ordering the system gets into a stationary state for times $t \geq 70 \times 10^4$. (b) The stationary correlation function $C_s(r, E_0)$ at $t = 75 \times 10^4(\circ)$ is compared with the equilibrium correlation function $C_{eq}(r, E_0)$.

An analogous situation occurs in the quenched dynamics of the random field Ising model (RFIM) [21]. Here, temperature is an irrelevant variable. However if we set $T = 0$ a priori, the domain walls which are pinned by the quenched field will be immobile, thus preventing coarsening. A finite temperature is needed for the domain walls to surmount the pinning energy barrier, this gives a nonzero wall mobility. Temperature, in the RFIM, is thus a dangerously irrelevant variable [22]. Therefore in the absence of thermal fluctuations (at $T = 0$) the interfaces remain immobile, very much like the defects in the pure torque model, where dissipation plays the role of temperature.

It is clear from the above discussion that a naive perturbation in terms of the defect

mobility Γ_D as a small parameter would be invalid. For a nonzero defect mobility breaks the conservation laws of the pure torque dynamics, *viz.* total conservation of total energy and the local spin magnitude. This suggests that the $\Gamma_D \neq 0$ dynamics cannot be obtained as a smooth continuation of the $\Gamma_D = 0$ case. It is also clear that Γ multiplies the highest derivative in the equation of motion (Eq. (2.1)), therefore a perturbation in Γ_D would amount to performing a singular perturbation theory [23] on the pure torque dynamics. We plan to investigate this aspect in a future study.

Since a perturbation about the $\Gamma = 0$ limit is far from simple, we ask whether we may perturb about the $g = 0$ fixed point. This is discussed in the next section.

2.1.3 Perturbation about $g = 0$: The Gaussian Closure Scheme

To devise a perturbation theory about $g = 0$, we would need to have a reasonably accurate theory of the purely dissipative dynamics. The Gaussian Closure Scheme introduced by Mazenko [11] has been considered a very successful approximate theory to compute scaling functions and dynamical exponents arising from purely dissipative Langevin equations.

Inspiration for this method draws from the fact that at late times the order parameter relaxes to its equilibrium value everywhere except at interfaces and defect cores. At late times, the distance between these defects cores (interfaces) gets to be much larger than the screening length, consequently the defects can be assumed to be weakly interacting. This suggests that if we change variables from the strongly interacting order parameter fields to the weakly interacting defect fields, a systematic approximation scheme might emerge. It should be emphasized that the approximation formulated by Mazenko is *non-perturbative* and not a perturbative expansion in the coupling between defects. We shall now present a brief discussion of the method tailored for the Heisenberg model and critically assess whether the method accurately describes the late stages of the dynamics of Eq. (2.1).

The method consists of trading the order parameter $\vec{\phi}(\mathbf{r}, t)$ which is singular at defect sites, for an everywhere smooth field $\vec{m}(\mathbf{r}, t)$ defined by a nonlinear transformation,

$$\vec{\phi}(\mathbf{r}, t) = \vec{\sigma}(\vec{m}(\mathbf{r}, t)) . \quad (2.25)$$

The choice for the nonlinear function $\vec{\sigma}$ is dictated by the expectation that at late times, the magnitude of $\vec{\phi}$ saturates to its equilibrium value almost everywhere except near the defect cores. This suggests that the appropriate choice for $\vec{\sigma}$ is an equilibrium defect profile,

$$\frac{1}{2} \nabla_m^2 \vec{\sigma}(\vec{m}(\mathbf{r}, t)) = V'(\vec{\sigma}(\vec{m}(\mathbf{r}, t))) , \quad (2.26)$$

where $V'(\vec{x}) \equiv -\vec{x} + (\vec{x} \cdot \vec{x}) \vec{x}$. Implicit in this choice is that smooth configurations such as spin-waves relax fast and so decouple from defects at late times. The simplest nontrivial solution of Eq. (2.26) is the hedgehog configuration,

$$\vec{\sigma}(\vec{m}(\mathbf{r}, t)) = \frac{\vec{m}(\mathbf{r}, t)}{|\vec{m}(\mathbf{r}, t)|} \psi(|\vec{m}|) , \quad (2.27)$$

where $\psi(0) = 0$ and $\psi(\infty) = 1$. The auxiliary field \vec{m} now has the natural interpretation as the position vector from the nearest defect core.

Equation (2.3) can be used to derive an equation for the correlation function $C(12) \equiv \langle \vec{\phi}(\mathbf{r}_1, t_1) \cdot \vec{\phi}(\mathbf{r}_2, t_2) \rangle$. Although the method was originally used by Mazenko to solve purely dissipative equations alone, we will use the same prescription to deduce the equations for $C(12)$ when $g \neq 0$. Substituting for $\vec{\phi}$ (Eqs. (2.25), (2.27)) in the right hand side of the resulting equation we get

$$\begin{aligned} \partial_t C(12) = & (-i \nabla_1)^\mu \left[\nabla_1^2 C(12) - \langle \vec{\sigma}(\vec{m}(2)) \cdot V'(\vec{\sigma}(\vec{m}(1))) \rangle \right] \\ & + g \langle \vec{\sigma}(\vec{m}(2)) \cdot \vec{\sigma}(\vec{m}(1)) \times \nabla_1^2 \vec{\sigma}(\vec{m}(1)) \rangle . \end{aligned} \quad (2.28)$$

The Gaussian Closure Scheme assumes that each component of $\vec{m}(\mathbf{r}, t)$ is an independent Gaussian field with zero mean at all times. This implies that the joint probability distribution $P(12) \equiv P(\vec{m}(1), \vec{m}(2))$ is a product of separate distributions for each component and is given by [10],

$$P(12) = \prod_{\alpha} \mathcal{N} \exp \left\{ -\frac{1}{2(1-\gamma^2)} \left(\frac{m_{\alpha}^2(1)}{S_0(1)} + \frac{m_{\alpha}^2(2)}{S_0(2)} - \frac{2\gamma m_{\alpha}(1)m_{\alpha}(2)}{\sqrt{S_0(1)S_0(2)}} \right) \right\} , \quad (2.29)$$

where

$$\mathcal{N} = \frac{1}{2\pi \sqrt{(1-\gamma^2)S_0(1)S_0(2)}}$$

and

$$\gamma \equiv \gamma(12) = \frac{C_0(12)}{\sqrt{S_0(1)S_0(2)}}. \quad (2.30)$$

The joint distribution has been written in terms of the second moments $S_0(1) = \langle m_\alpha(1)^2 \rangle$ and $C_0(12) = \langle m_\alpha(1)m_\alpha(2) \rangle$.

Using the above assumptions (Eq. (2.29)) and the form of $\vec{\sigma}(\vec{m})$ (Eq. (2.27)), the equal time correlation function can be written in the form [11].

$$C(12) = \frac{3\gamma}{2\pi} \left[B\left(2, \frac{1}{2}\right) \right]^2 F\left(\frac{1}{2}, \frac{1}{2}, \frac{5}{2}; \gamma^2\right) \quad (2.31)$$

where $B(x, y)$ and $F(a, b, c; z)$ are the beta and hypergeometric functions respectively and γ is defined by Eq. (2.30). The functions $\gamma(12)$, $S_0(1)$ and $S_0(2)$ are to be determined by plugging this implicit form into Eq. (2.28),

$$\begin{aligned} \frac{\partial C(12)}{\partial t_1} = & (-i\nabla)^\mu \left[\nabla^2 C(12) + \frac{\gamma}{2S_0(1)} \frac{\partial C(12)}{\partial \gamma} \right] \\ & + g \langle \vec{\sigma}(\vec{m}(2)) \cdot \vec{\sigma}(\vec{m}(1)) \times \nabla^2 \vec{\sigma}(\vec{m}(1)) \rangle, \end{aligned} \quad (2.32)$$

where the Laplacian is taken with respect to \mathbf{r}_1 . This equation does not yet provide an explicit form for $C(12)$; we will do so for the case when $g = 0$. Setting $g = 0$ in Eq. (2.32), we may determine γ either numerically or analytically; $C(r, t)$ is then evaluated by substituting this solution back in Eq. (2.31). This completes the calculation of the two point correlation function from the Gaussian approximation scheme.

Having found a precisely formulated approximate theory at $g = 0$, we test it for *consistency* and *accuracy* against known exact results or numerical simulations. It has been shown that the Gaussian closure scheme is exact in the limit when the number of components of the order parameter $n \rightarrow \infty$ or the dimension $d \rightarrow \infty$ [10, 24]. To test this approximate theory for finite n and d one needs to resort to numerical simulations. A variety of studies mainly restricted to scalar order parameters, have shown [11, 10, 7, 26] that this scheme quite accurately reproduces the two point correlation functions and dynamic exponents for nonconserved order parameter dynamics. Unfortunately the scheme has met with limited success when the order parameter is conserved [10, 25]. For our purpose the consistency and

accuracy of the scheme should be checked both for $g = 0$ and $g \neq 0$. We first carry out systematic numerical tests for the nonconserved dynamics.

A. Testing the Gaussian Closure Scheme for the NCOP Dynamics

We will do this by numerically solving the Langevin equation Eq. (2.3) by the method outlined in Section 2.1.1 A. Knowing $\vec{\phi}(\mathbf{r}, t)$, one can compute $\vec{m}(\mathbf{r}, t)$ by inverting Eq. (2.27). This is facilitated by choosing

$$\psi(|\vec{m}|) = \frac{|\vec{m}|}{\sqrt{1 + \vec{m} \cdot \vec{m}}} \quad (2.33)$$

which is consistent with the boundary conditions for $\psi(x)$ mentioned earlier. The resulting ansatz for $\vec{\sigma}$,

$$\vec{\sigma}(\vec{m}(\mathbf{r}, t)) = \frac{\vec{m}}{\sqrt{1 + \vec{m} \cdot \vec{m}}}, \quad (2.34)$$

may be easily inverted. We calculate both the single point probability distribution $P(\vec{m}(\mathbf{r}, t))$ and the joint probability distribution $P(12)$ in the scaling regime and compare with the Mazenko assumption. In what follows all probability distributions have been computed on a 45^3 lattice and averaged over 100 initial configurations. We have collected data in the scaling regime from $t = 2000$ to $t = 15000$, after which finite size effects set in. Figures 2.18a and 2.18b, are the scaling plots of $P(m_1(\mathbf{r}, t))$ at $g = 0$ and $g = 1$ respectively. In accordance with the Mazenko assumption, the scaling variable has been taken to be $m_1/\sqrt{S_0(t)}$, where $S_0(t) = \langle m_1(\mathbf{r}, t)^2 \rangle$ is seen to grow linearly in time, consistent with $z = 2$ (Fig. 2.19).

The scaled distribution $P(m_1)$ for $g = 1$ is also seen to be identical to the $g = 0$ case (Fig. 2.18c), suggesting that it is independent of g .

Though the distribution grossly resembles a Gaussian at late times, closer inspection shows systematic deviations at small values of m_1 (Fig. 2.18c). The distribution seems to be flatter than a Gaussian when $m_1 \approx 0$. This is clearly visible in a plot of $-\ln(-\ln[P(m_1^2/S_0)])$ versus $\ln(m_1^2/S_0)$, which shows that distribution deviates from a Gaussian for small m_1 (Fig. 2.20). These findings are consistent with a similar analysis done on a scalar order parameter [27]. Therefore our numerics suggests that the Gaussian Approximation as formulated for nonconserved dynamics, is consistent but not very accurate. However one can in principle

systematically improve the accuracy of the method by taking account of corrections to the Gaussian distribution [28].

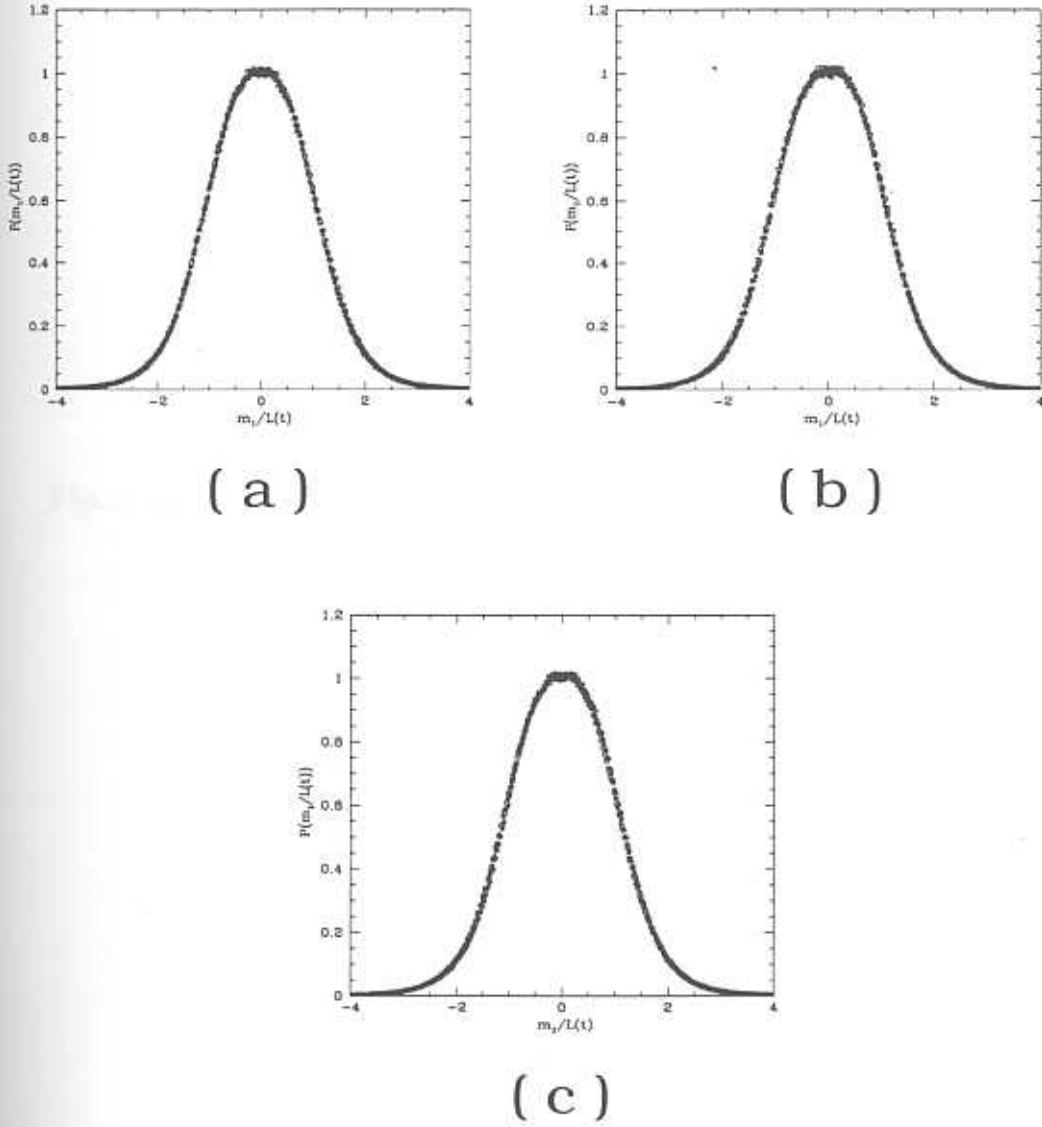


Figure 2.18: (a) Single point distribution of $P(m_1)$ for $g = 0$ at different times $t = 5000$ (\circ), $t = 10000$ (\square), $t = 15000$ (\triangle). The distribution scales in the variable m_1/L , where $L(t) = \sqrt{S_0(t)}$. (b) Same as Fig. 2.18a, but for $g = 1$ for times $t = 5000$ (\circ), $t = 10000$ (\square), $t = 15000$ (\triangle). (c) Scaling plot of $P(m_1)$ is independent of g . Data taken for $g = 0$ ($t = 5000$ (\circ), $t = 10000$ (\square)) and $g = 1$ ($t = 5000$ (\triangle), $t = 10000$ (\star)).

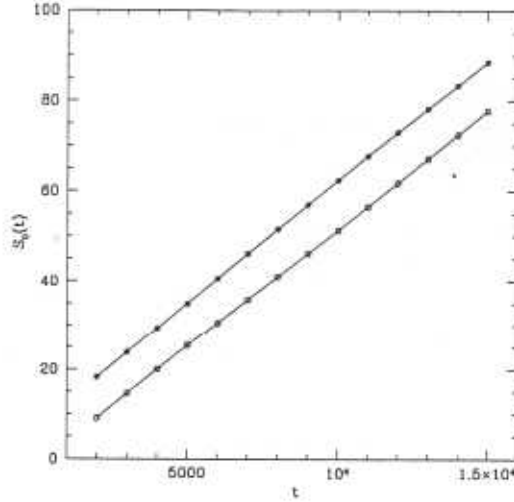


Figure 2.19: Linear growth of $S_0(t)$ with t for $g = 0$ (\circ) and $g = 1$ (\bullet).

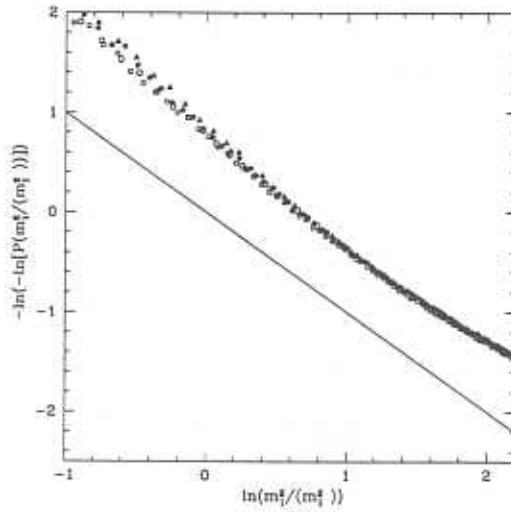


Figure 2.20: Plot of $-\ln(-\ln[P(m_1^2/S_0)])$ versus $\ln(m_1^2/S_0)$ for $g = 0$ ($t = 5000$ (\circ), $t = 10000$ (\square)) and $g = 1$ ($t = 5000$ (\triangle), $t = 10000$ (\star)). The line with slope -1 drawn for comparison, highlights the deviation of the data from a Gaussian at smaller m_1 .

We now study the joint probability distribution $P(\vec{m}(1), \vec{m}(2))$. Equation (2.29) implies that in the variables

$$\vec{m}_{\pm}(12) = \frac{1}{2} \left(\frac{\vec{m}(1)}{\sqrt{S_0(1)}} \pm \frac{\vec{m}(2)}{\sqrt{S_0(2)}} \right) (S_0(1)S_0(2))^{\frac{1}{4}},$$

the joint distribution can be written as a product $P(12) = P(\vec{m}_+(12))P(\vec{m}_-(12))$, where

$$P(\vec{m}_\pm(12)) = \prod_{\alpha} \sqrt{N} \exp \left\{ -\frac{m_{\alpha\pm}^2}{(1 \pm \gamma) \sqrt{S_0(1)S_0(2)}} \right\}. \quad (2.35)$$

We numerically compute $P(m_{\alpha+}(12), m_{\alpha-}(12))$ at $t_1 = t_2 = t$ in the scaling regime. A plot of $P(m_{1+}, m_{1-})$ for $|\mathbf{r}_1 - \mathbf{r}_2| = 4\sqrt{3}$ looks like a product of two Gaussian distributions (Fig. 2.21a). Next we compute $P(m_{1+}(12))$ and $P(m_{1-}(12))$ and scaling plots of $P(m_{1+})$ and $P(m_{1-})$ (Fig. (2.22a) and Fig. (2.22b) respectively) which indicate that the distribution looks like a Gaussian, in accordance with the Mazenko theory. The scaling plots suggest that the scaling function is independent of g . Figures 2.23a and 2.23b are plots of $-\ln(-\ln[P(m_{i\pm}^2(12))/\langle m_{i\pm}^2(12) \rangle])$ versus $\ln(m_{i\pm}^2(12)/\langle m_{i\pm}^2(12) \rangle)$. The deviation from a straight line when $m_{i\pm} \approx 0$, indicates that the distributions differ slightly from a Gaussian. Note that the data for small $m_{i\pm}$ in Figs. 2.23a, 2.23b do not quite scale and so it is likely that in the computation of the joint-probability distribution, we have not yet reached the scaling regime. To verify the Gaussianess of $P(m_{\alpha+}(12), m_{\alpha-}(12))$ we calculate the difference

$$\Delta(m_{\alpha+}(12), m_{\alpha-}(12)) \equiv P(m_{\alpha+}(12), m_{\alpha-}(12)) - P(m_{\alpha+}(12))P(m_{\alpha-}(12)), \quad (2.36)$$

which should be zero everywhere if the Mazenko approximation were to hold. Figure 2.21b shows a surface plot of the difference $\Delta(m_{1+}(12), m_{1-}(12))$, magnified 10^5 times. It is clear that $\Delta(m_{1+}(12), m_{1-}(12))$ is zero everywhere except in the region close to the origin, where the maximum deviation from 0 is around 10^{-5} .

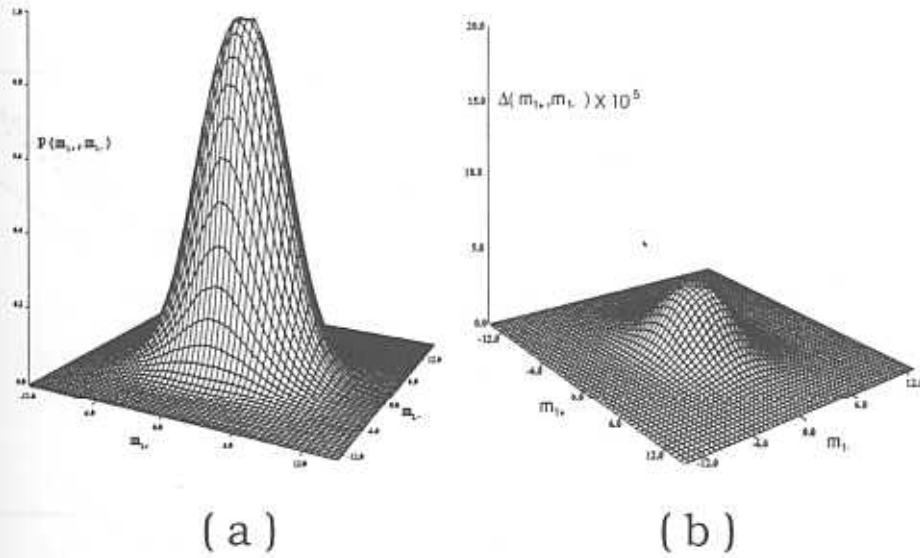


Figure 2.21: (a) Joint probability distribution $P(\vec{m}_+(12), \vec{m}_-(12))$ for $g = 0$ at $t = 5000$ and $|\mathbf{r}_1 - \mathbf{r}_2| = 4\sqrt{3}$. (b) Surface plot of $\Delta(m_{1+}(12), m_{1-}(12))$ (magnified 10^5 times) for $g = 0$ at $t = 5000$ and $|\mathbf{r}_1 - \mathbf{r}_2| = 4\sqrt{3}$. Plots are similar for $g = 1$.

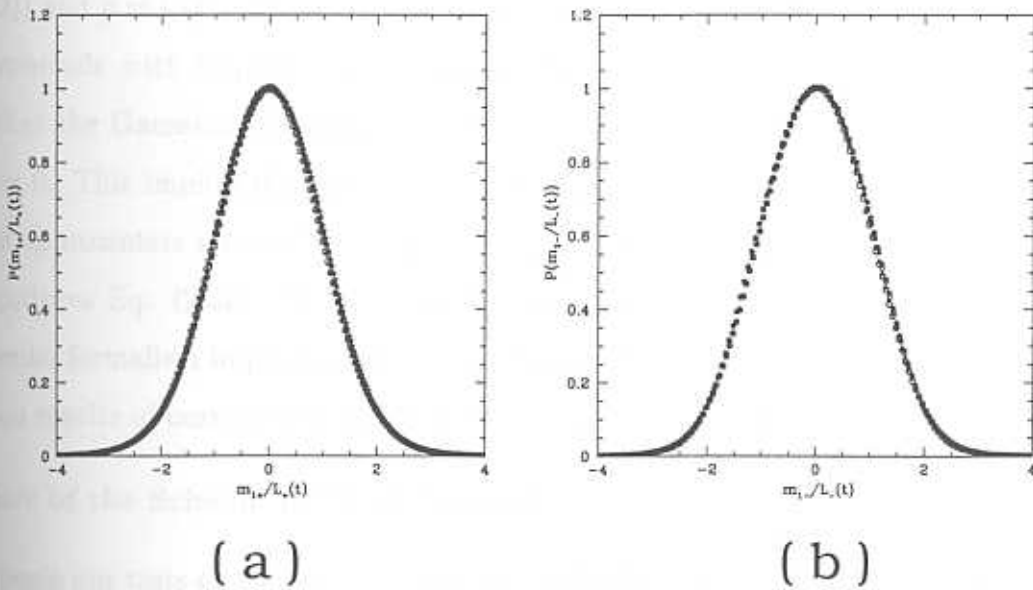


Figure 2.22: (a) Scaling plot of $P(m_{1+}/L_+)$, where $L_+ = \sqrt{\langle m_{1+}^2(\mathbf{r}, t) \rangle}$, for $g = 0$ ($t = 5000$ (\circ), $t = 10000$ (\square)) and $g = 1$ ($t = 5000$ (\triangle), $t = 10000$ (\star)). (b) Scaling plot of $P(m_{1-}/L_-)$, where $L_- = \sqrt{\langle m_{1-}^2(\mathbf{r}, t) \rangle}$, for $g = 0$ ($t = 5000$ (\circ), $t = 10000$ (\square)) and $g = 1$ ($t = 5000$ (\triangle), $t = 10000$ (\star)).

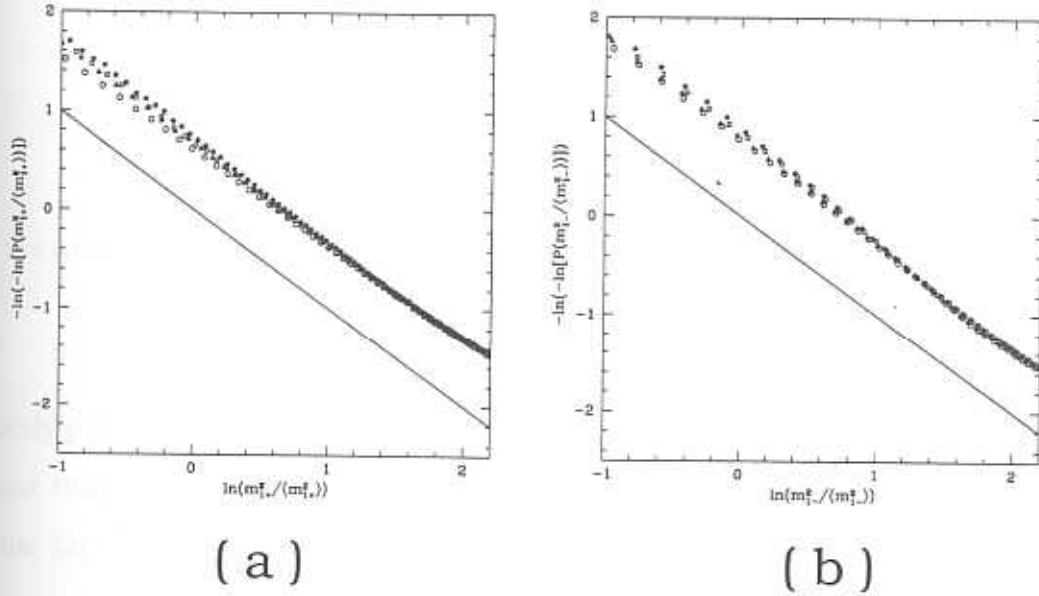


Figure 2.23: (a) $P(m_{+1}/L_{+})$ shows deviation from Gaussian for small m_{+} . Data shown for $g = 0$ ($t = 5000$ (\circ), $t = 10000$ (\square)) and $g = 1$ ($t = 5000$ (\triangle), $t = 10000$ (\star)). (b) $P(m_{-1}/L_{-})$ shows deviation from Gaussian for small m_{-} . Data shown for $g = 0$ ($t = 5000$ (\circ), $t = 10000$ (\square)) and $g = 1$ ($t = 5000$ (\triangle), $t = 10000$ (\star)).

We conclude with the following remarks. Based on our extensive numerical analysis, we see that the Gaussian Approximation Scheme is consistent and accurate (in principle) when $g = 0$. This implies that we can do perturbation about $g = 1$. We have tested that the same approximate scheme is accurate for $g = 1$. Extending the Mazenko formalism to $g \neq 0$ produces Eq. (2.32). We see that the last term containing g should be zero within the Mazenko formalism implying that g is irrelevant. This conclusion is consistent with the simulation results of ours in Sect. 2.1.1 A. Now we move on to the conserved dynamics.

B. Failure of the Scheme in COP Dynamics

We will begin our tests of the Gaussian Scheme applied to conserved dynamics investigating the consistency of the Gaussian assumption of the approximate scheme on the lines suggested by Yeung et. al. [27] for the case of a conserved scalar (Ising) order parameter. We will do this when $g = 0$, the $g \neq 0$ analysis follows similarly. The Gaussian Approximation provided us with a form for the two point correlation function given in Eq. (2.31). We may expand

the hypergeometric function as a power series in γ [17] and then take its Fourier transform,

$$S(\mathbf{k}, t) = \sum_{p=0}^{\infty} \int d\mathbf{k}_1 \dots d\mathbf{k}_{2p+1} \left[a_p \gamma_{\mathbf{k}_1}(t) \gamma_{\mathbf{k}_2}(t) \dots \gamma_{\mathbf{k}_{2p+1}}(t) \delta(\mathbf{k} + \mathbf{k}_1 + \dots + \mathbf{k}_{2p+1}) \right] \quad (2.37)$$

where the spectral density $\gamma_{\mathbf{k}}$ is the Fourier transform of $\gamma(r, t)$ and the expansion coefficients,

$$a_p = \frac{9}{8\pi^{3/2}} \frac{[\Gamma(p+1/2)]^2}{\Gamma(p+5/2)p!} \left[B\left(2, \frac{1}{2}\right) \right]^2, \quad (2.38)$$

are strictly positive for $p \geq 0$. If Eq.(2.37) has to satisfy the conservation law $S(k=0, t) = 0$, it is clear that $\gamma_{\mathbf{k}}(t)$ should be *negative* at some values of \mathbf{k} . This is inconsistent with the definition Eq. (2.30) which implies $\gamma_{\mathbf{k}}(t) \geq 0$ for all \mathbf{k} . This definition is a consequence of the Gaussian approximation.

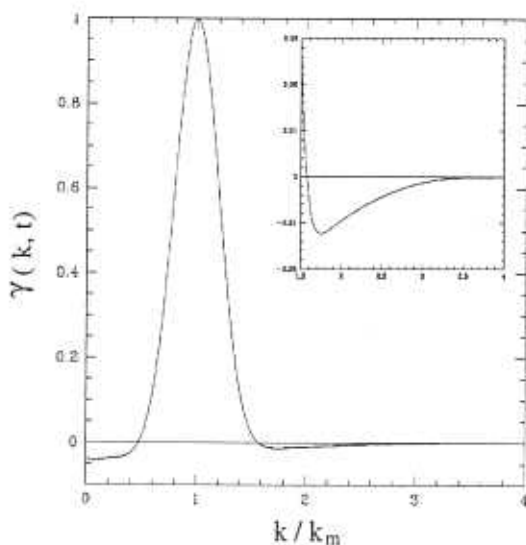


Figure 2.24: The spectral density $\gamma(k, t)$ at $t = 3600$ becomes negative for $0 \leq k/k_m < 0.5$ and for $1.5 < k/k_m < 3.0$ (inset).

To determine the range of values of \mathbf{k} for which $\gamma_{\mathbf{k}}$ is negative, we numerically evaluate the Fourier transform of $\gamma(r, t)$ after inverting Eq. (2.31). This is prone to numerical errors because of statistical errors in our computed $C(r, t)$. For instance, a numerical integration of $\int d\mathbf{r} C(r, t)$ gives a nonzero value whereas it should be identically zero because of the conservation law. This is reflected in large errors in $\gamma(\mathbf{k}, t)$ at small \mathbf{k} . We therefore adopt

the following procedure. We fit a function $C_f(x)$ to the equal time correlation function $C(r, t)$ and use this to extract $\gamma(\mathbf{k}, t)$ from the Eq. (2.31). The fitting function has been taken to be

$$C_f(x) = \frac{\sin(x/L)}{(x/L)} \left[1 + a \left(\frac{x}{L} \right)^2 \right] \exp[-b(x/L)^2], \quad (2.39)$$

which is similar to the analytic form given in Ref. [30]. Note that only b and L are independent fitting parameters, a is determined from the condition $S_f(k=0) = 0$. This function with $L = 1.5106 \pm 1.01 \times 10^{-4}$ and $b = 0.0202 \pm 2.14 \times 10^{-4}$ gives a very good fit to $C(r, t)$ upto the fourth zero of the function. We observe (Fig. 2.24) that the spectral density, which should be a strictly positive function of its arguments, becomes negative for $k/k_m < 0.5$ ($\gamma(k, t)$ is peaked at k_m) and in the range $1.5 < k/k_m < 3.0$.

Our demonstration suggests that a purely Gaussian theory for the distribution of \vec{m} is internally inconsistent. This may however be remedied by considering corrections to the purely Gaussian distribution, as suggested by Mazenko [28] for the scalar (Ising) order parameter.

In order to help us understand the nature of the corrections, let us first numerically evaluate the probability distribution of \vec{m} . As described in the last section we determine \vec{m} from Eq. (2.33). We now compute the asymptotic single point probability density $P(m_1(\mathbf{r}, t))$ on a 50^3 lattice averaged over 18 initial configurations for both $g = 0$ and $g \neq 0$. The probability density obeys a scaling form at late times (Figs. 2.25a-b), $P(m_1, t) = P(m_1/L(t))$, where the length scale $L(t) = \sqrt{\langle m_1^2 \rangle} \sim t^{1/z}$.

It is clear from Figs. 2.25a - b that the asymptotic distributions show marked deviations from a simple Gaussian. To highlight these deviations, we plot the scaled $\log(-\log(P(m_1)))$ versus $\log(m_1^2)$ (Fig. 2.26), a Gaussian distribution would have given a straight line with slope -1 .

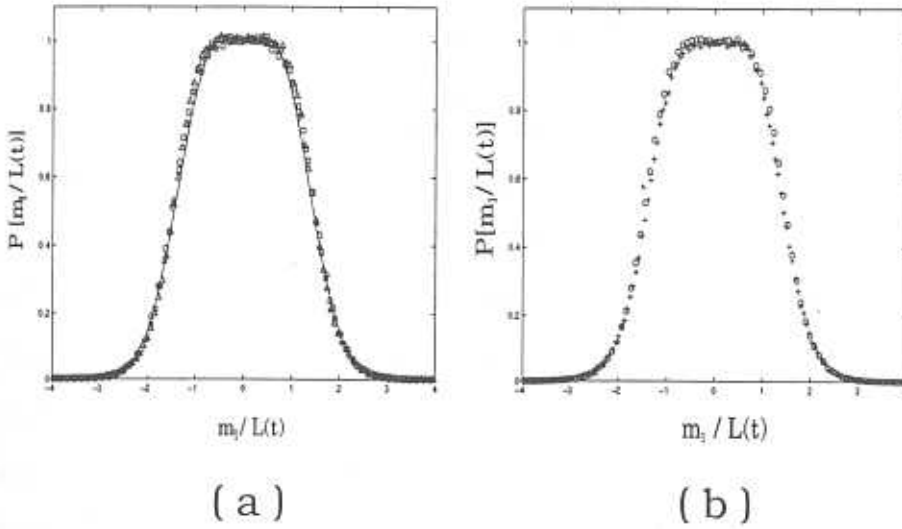


Figure 2.25: (a) Scaling plot of the un-normalized $P(x = m_1/L(t))$ for $g = 0$ at different times $t = 900(\circ)$, $3600(\square)$, $6300(\triangle)$. Solid line is a fit to Eq. (2.40). (b) Scaling plot of the un-normalized $P(x = m_1/L(t, g))$ for $g = 0(\circ)$ and $g = 0.3(+)$ at $t = 4500$ showing that the distributions are identical within error bars.

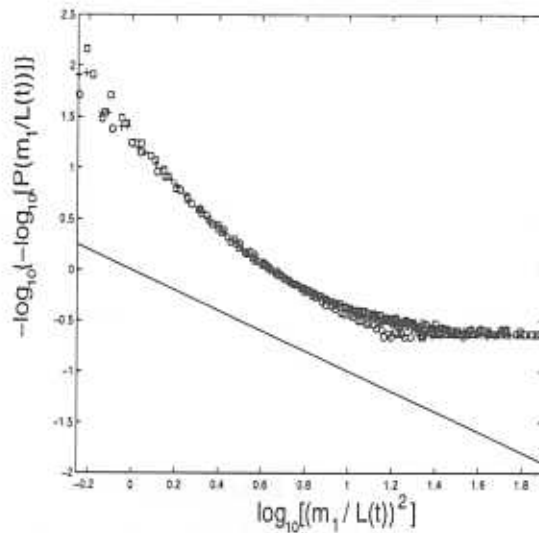


Figure 2.26: Deviation of $P(x = m_1/L)$ from Gaussian (straight line) for $g = 0$. Data have been collected at times $t = 900(\circ)$, $3600(+)$, $6300(\square)$.

Figures 2.25a - b suggest that the deviations from Gaussian can be computed by expanding $P(m)$ in a Hermite polynomial basis H_n (a strategy advocated in Ref. [28] for the scalar

(Ising) dynamics),

$$P(x) = \sum_{n=0}^{\infty} p_n H_n(x) e^{-x^2}, \quad (2.40)$$

where $x = m_1(r, t)/\sqrt{S_0(r, t)}$ and $H_0(x) = 1$, $H_1(x) = 2x$ and $H_{n+1}(x) = 2xH_n(x) - 2nH_{n-1}(x)$. The dark line in Figure 2.25a is an accurate fit to the $g = 0$ data, with $p_0 = 1$, $p_1 = 1.33 \times 10^{-3} \pm 6.0 \times 10^{-5}$, $p_2 = 0.2352 \pm 3.8 \times 10^{-5}$, $p_3 = 1.55 \times 10^{-4} \pm 1.5 \times 10^{-5}$, $p_4 = 5.542 \times 10^{-3} \pm 7.0 \times 10^{-6}$. Indeed the odd coefficients are zero to within numerical accuracy, indicating that the distribution is even.

Now we perform the same checks for $g \neq 0$. As before in $g = 0$, $\gamma(\mathbf{k}, t)$ picks up negative values for certain ranges of \mathbf{k} . We have evaluated probability density $P(m_1, t)$ for $g = 0.3, 0.4$ and 0.5 . The scaled distribution for $g = 0.3$ is shown in Fig. 2.27 which is found to be identical to the $g = 0$ distribution, Fig. 2.25b.

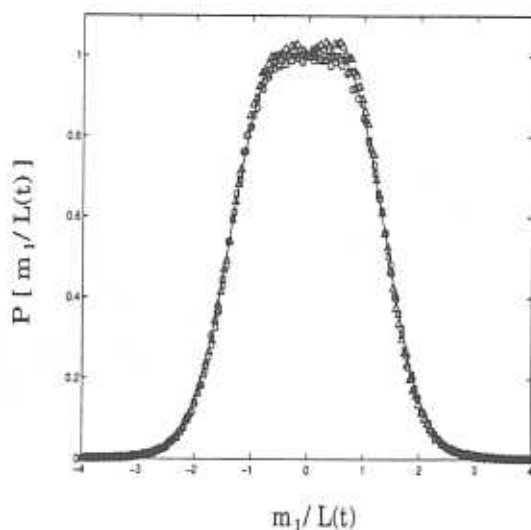


Figure 2.27: Scaling plot of the un-normalized $P(x = m_1/L(t))$ for $g = 0.3$ at different times $t=1350(\diamond)$, $3600(+)$, $5400(\square)$. Solid line is a fit to Eq. (2.40).

As before the deviations from the Gaussian nature can be accounted for by introducing corrections in a Hermite polynomial basis. In Fig. 2.27, the dark line is an accurate fit to the $g = 0.3$ data with $p_0 = 1$, $p_1 = 3.95 \times 10^{-3} \pm 5.5 \times 10^{-5}$, $p_2 = 0.2899 \pm 1.3 \times 10^{-5}$, $p_3 = 5.35 \times 10^{-4} \pm 1.3 \times 10^{-5}$, $p_4 = 1.1913 \times 10^{-2} \pm 7.0 \times 10^{-6}$. Vanishing of the odd coefficients within numerical accuracy suggests that the distribution is even.



It is conceivable that such corrections would be able to salvage the inconsistency issue both for $g = 0$ and $g \neq 0$, since an additive term to the right hand side of Eq. (2.37) would not allow us to assert that γ_k should be negative for some values of k .

Though the remedy suggested cures the inconsistency problem, it will still give a zero value to the torque contribution in Eq. (2.32) as long as the probability distribution of each component of \vec{m} is even and independent. We have already demonstrated that the single point distribution is even, now we shall show that each cartesian component of \vec{m} is independently distributed.

We numerically calculate $P(m_1(1), m_2(2))$ (which we label $P(x, y)$) at equal times $t_1 = t_2 = t$ and arbitrary separation, say $|\mathbf{r}_1 - \mathbf{r}_2| = 4\sqrt{3}$ for $g = 0.3$ (Fig. 2.28a).

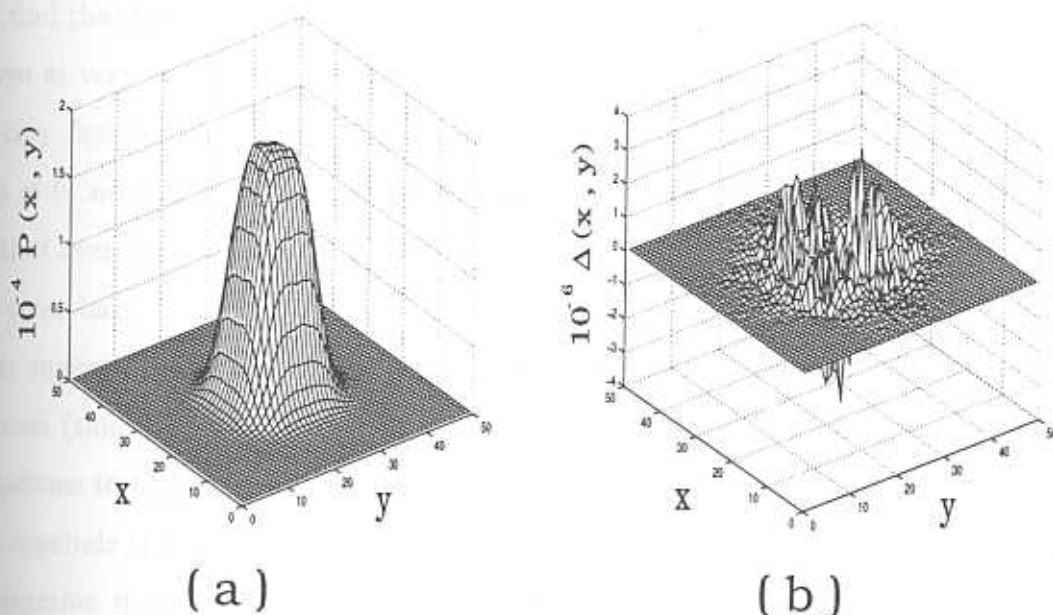


Figure 2.28: (a) Normalized joint probability distribution $P(x, y)$ where $x = m_1(1)$, $y = m_2(2)$ for $g = 0.3$ at $t = 2250$ and $|\mathbf{r}_1 - \mathbf{r}_2| = 4\sqrt{3}$ (averaged over 18 initial configurations). (b) Plot of $\Delta(x, y)$ where $x = m_1(1)$, $y = m_2(2)$ at $t = 2250$ and $|\mathbf{r}_1 - \mathbf{r}_2| = 4\sqrt{3}$ for $g = 0.3$. The maximum magnitude of Δ is of the order of errors in $\Delta(x, y)$.

To show that the joint distribution is independent in each component, we plot the difference $\Delta(x, y) = P(x, y) - P(x)P(y)$ for $g = 0.3$ (Fig. 2.28b) and find it to be zero within the accuracy of our numerical computation.

Let us summarize the situation so far. The Mazenko approximation can be made consistent and accurate for the conserved dynamics (both for $g = 0$ and $g \neq 0$) by incorporating systematic deviations to the Gaussian distribution. However, in the presence of the torque term ($g \neq 0$) this formalism runs into serious problems. It is easy to see that if Mazenko approximation holds for the $g \neq 0$ dynamics, the g term in Eq. (2.32) vanishes and is therefore irrelevant. This is in direct contradiction with our numerical result (Section 2.1.1 B).

We suggest a way out of this impasse. It appears that we are forced to admit that the order parameter $\vec{\phi}$ cannot be written in terms of \vec{m} alone (Eq. (2.25)). For in transforming the spins $\vec{\phi}$ exclusively to \vec{m} we have implicitly ignored spin-waves. The most direct demonstration of this is to compare $C_{3\vec{\phi}} = \langle \vec{\phi}(1) \cdot (\vec{\phi}(2) \times \nabla_2^2 \vec{\phi}(2)) \rangle$ with the defect-only contribution $C_{3\vec{m}} = \langle \vec{m}(1) \cdot (\vec{m}(2) \times \nabla_2^2 \vec{m}(2)) \rangle$ (where \vec{m} is computed by inverting Eq. (2.33)).

We find that for $g = 0$ both $C_{3\vec{\phi}}$ and $C_{3\vec{m}}$ are zero within error bars (Fig. 2.29a). This is true even at very early times which implies that in the absence of the torque the spin-waves decay very fast compared to the relaxation timescale of the defects. On the other hand, when $g \neq 0$, we find that the two correlators behave very differently. Figure 2.29b clearly shows that even at late times, $C_{3\vec{\phi}}$ is non zero while the defect-only contribution $C_{3\vec{m}}$ is zero within error bars.

This suggests the following decomposition in terms of defect fields (singular part) and spin-waves (smooth part), $\vec{\phi} = \vec{\sigma}(\vec{m}) + \vec{u}$, when $g \neq 0$. Such a decomposition gives rise to contributions to $C_{3\vec{\phi}}$ reflecting the interaction between defects and spin-waves.

We conclude this long meandering section by recounting its salient results. The Mazenko approximation in the conserved dynamics can be made consistent and accurate by incorporating systematic deviations to the Gaussian distribution both for the purely dissipative dynamics ($g = 0$) and for the dissipative dynamics with torque ($g \neq 0$). It is evident from our numerical and analytic study that inertia is relevant in conserved dynamics which makes the spin-waves long-lived even at late times. This results in the failure of the standard Mazenko approximation when inertia is present in the dynamics. An accurate approximation scheme when $g \neq 0$, should incorporate the interaction between defects and spin-waves excitations. We intend to work on this aspect in future.

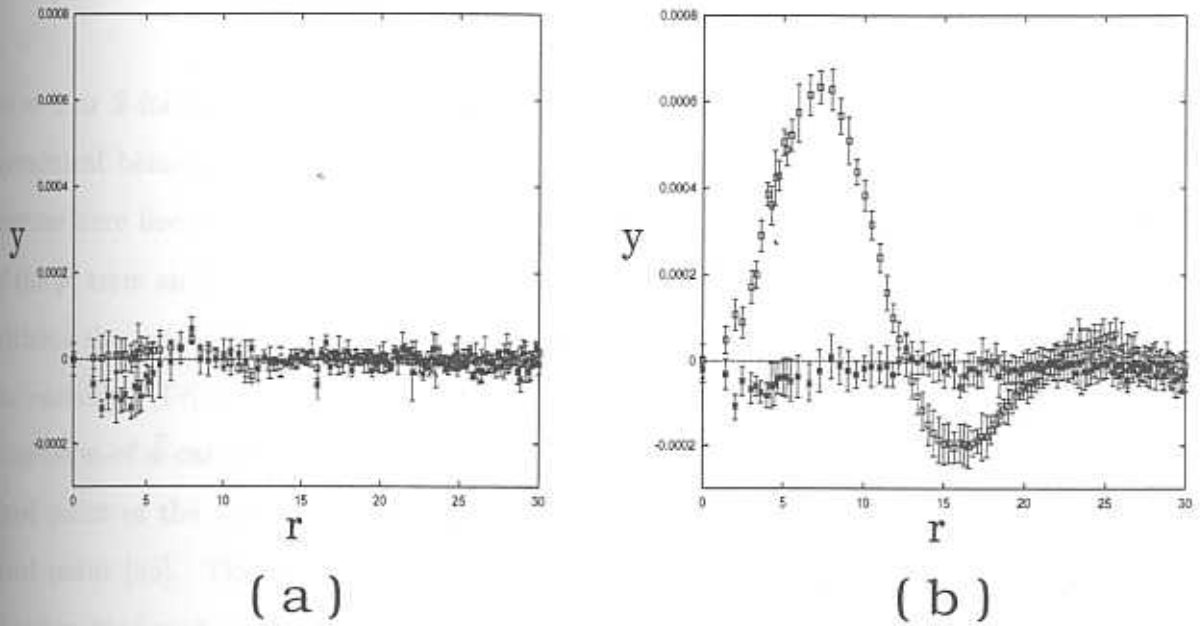


Figure 2.29: (a) $y = C_{3\vec{\phi}}(r)$ (\square) and $y = C_{3\vec{m}}(r)$ (*) at $t = 3600$ and $r = |\mathbf{r}_1 - \mathbf{r}_2|$ for $g = 0$ are zero within the error bars (averaged over 5 initial configurations). (b) $y = C_{3\vec{\phi}}(r)$ (\square) and $y = C_{3\vec{m}}(r)$ (*) at $t = 3600$ and $r = |\mathbf{r}_1 - \mathbf{r}_2|$ for $g = 0.3$ are distinctly different (averaged over 5 initial configurations). $C_{3\vec{m}}(r)$ (+), which has contributions from defects alone, is zero (within error bars), whereas $C_{3\vec{\phi}}(r)$, which in addition involves spin-wave excitations, is non zero.

2.2 Dynamics at $T = T_c$

Our final study is the dynamics of ordering following a quench to the critical point T_c . This section is added for completeness; several results derived here have been presented elsewhere [31, 32, 33]. The critical dynamics of the conserved model (called Model J in this context) was investigated some time ago by Ma and Mazenko [31]. On the other hand, the dynamical renormalisation group formalism for quench dynamics set up by Janssen *et.al.*, has been used to study Models A - C [32, 34].

We quench the system from the high temperature paramagnetic phase to the critical point T_c , and ask whether the spin precession given by the equation,

$$\frac{\partial \vec{\phi}}{\partial t} = -\Gamma(-i\nabla)^\mu \left(-\nabla^2 \vec{\phi} + r\vec{\phi} + u(\vec{\phi} \cdot \vec{\phi})\vec{\phi} \right) + \Omega_L (\vec{\phi} \times \nabla^2 \vec{\phi}) + \vec{\eta}, \quad (2.41)$$

where

$$\langle \eta_\alpha(\mathbf{x}, t) \eta_\beta(\mathbf{x}', t') \rangle = 2 k_B T \Gamma \delta_{\alpha\beta} (-i\nabla)^\mu \delta(\mathbf{x} - \mathbf{x}') \delta(t - t'), \quad (2.42)$$

($\mu = 0$ or 2 for nonconserved and conserved dynamics respectively) changes the late time dynamical behaviour. Unlike the zero temperature quench we can set up a perturbation scheme here because of presence of small parameters in Eq. (2.41), namely u , the coupling of the ϕ^3 term and $g = \Omega_L/\Gamma$, the coupling of the torque term. First, let us consider Eq. (2.41) without the torque term. The linear part of Eq. (2.41) gives the engineering dimensions of the variables, $[\Gamma t] = L^z = L^{2+\mu}$ and $[r] = L^a = L^{-2}$, where L is any length scale. The scaling dimension of $\vec{\phi}$ can be obtained from the free-energy (Eq. (1.3)), $[\phi] = L^x = L^{-d/2+1}$. The fixed point of the scaling transformation for the linear equation is known as the Gaussian fixed point [35]. The dimension of u at this fixed point is $[u] = L^{-2x-z+\mu} = L^{d-4}$ which vanishes at $d = d_c = 4$, d_c is the upper critical dimension of the perturbation scheme. If we calculate the corrections coming from the nonlinear part of Eq. (2.41) we will find that for dimensions higher than d_c the fixed point does not change from its Gaussian value ; the u -coupling is irrelevant. In contrast, for $d < d_c$, the Gaussian fixed point is no longer stable and the u -coupling takes the system to a new stable fixed point, in other words u is a relevant coupling. A dynamical renormalisation group scheme can be set up to calculate the new fixed points (stable and unstable) for $d \leq d_c$ and subsequently the exponents and scaling functions at the fixed points [35, 32]. The new fixed point (stable when $d < 4$), known as the Wilson-Fisher (WF) fixed point, is given to $\mathcal{O}(\epsilon^2)$ by $r^* = -(5/22)\Lambda^2\epsilon$, $u^* = 8\pi^2\epsilon/11$ (Λ is the ultraviolet cutoff), where $\epsilon = 4 - d$. We now include the torque term and ask whether the torque term g is relevant at this WF fixed point. We first study the nonconserved dynamics. The scaling dimension of g is computed by a power counting [32] to $\mathcal{O}(\epsilon^2)$ at the WF fixed point. The scaling dimension of g is read out by power counting $[g] = d/2 + 1 - z - \eta/2$. At the WF fixed point $z = 2 + c\eta$, where $c = 6 \ln(4/3) - 1$, and $\eta = (5/242)\epsilon^2$ to $\mathcal{O}(\epsilon^2)$. This implies that above $d = 2$, the torque term is irrelevant. At $d = 1$ the torque is relevant, as can be seen by an explicit solution of the Langevin equation Eq. (2.41) in one spatial dimension.

Next we turn to the conserved dynamics. Again power counting shows that the scaling

dimension of g is $d/2 + 1 - z + \eta/2$, where the exponents take their WF values $z = 4 - \eta$ and $\eta = (5/242)\epsilon^2$. This implies that the torque g is relevant at the WF fixed point for $d < 6$ [31].

We now have to determine this new torque driven fixed point and calculate the dynamical exponents z and λ . Both these exponents can be obtained readily using general arguments, which we briefly discuss. At the new fixed point it is clear that g does not get renormalised, which implies that $z = (d + 2 - \eta)/2$. Thus a calculation of z within perturbation theory reduces to a calculation of η at this fixed point [31]. Likewise λ can be obtained from the general arguments outlined in Ref. [36]. A crucial ingredient in this argument (valid only for quenches to T_c) is the demonstration that $S(k, t)$ obeys a scaling form at $k = 0$, a feature that was proved in Ref. [34] to all orders in perturbation for Model B dynamics. Here we *directly* calculate both z and λ using diagrammatic perturbation theory, and show that $\lambda = d$ to all orders in perturbation.

This is done within the Martin-Siggia-Rose (MSR) formalism [32]. For our problem the MSR generating functional is,

$$\begin{aligned} \mathcal{Z}[\vec{h}, \vec{\tilde{h}}] = \int \mathcal{D}(\vec{\phi}) \mathcal{D}(\vec{\tilde{\phi}}) \exp \left\{ -J[\vec{\phi}, \vec{\tilde{\phi}}] - H_0[\vec{\phi}_0] \right. \\ \left. + \int_0^\infty dt \int d\mathbf{k} (\vec{h}_{\mathbf{k}} \cdot \vec{\tilde{\phi}}_{-\mathbf{k}} + \vec{\tilde{h}}_{\mathbf{k}} \cdot \vec{\phi}_{-\mathbf{k}}) \right\} \end{aligned} \quad (2.43)$$

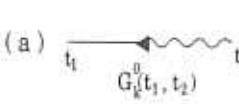
with the MSR action written as

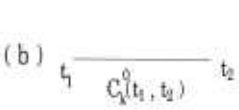
$$\begin{aligned} J[\vec{\phi}, \vec{\tilde{\phi}}] = \int_0^\infty dt \int d\mathbf{k} \left\{ \vec{\tilde{\phi}}_{\mathbf{k}} \cdot \left[\partial_t \vec{\phi}_{\mathbf{k}} + k^2 \frac{\delta F[\vec{\phi}]}{\delta \vec{\phi}_{-\mathbf{k}}} \right] \right. \\ \left. + \int d\mathbf{k}_1 \left(\frac{g\Gamma}{2} (k_1^2 - (\mathbf{k} - \mathbf{k}_1)^2) \vec{\phi}_{\mathbf{k}_1} \times \vec{\phi}_{\mathbf{k}-\mathbf{k}_1} \right) \right. \\ \left. - \Gamma k^2 \vec{\phi}_{\mathbf{k}} \cdot \vec{\tilde{\phi}}_{-\mathbf{k}} \right\}. \end{aligned} \quad (2.44)$$

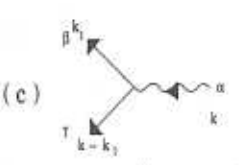
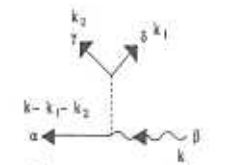
In the expression for the generating functional, the initial distribution of the order parameter (Gaussian with the width $= \tau_0^{-1}$) enters the form of $H_0 = \int d\mathbf{k} \frac{\tau_0}{2} (\vec{\phi}_{\mathbf{k}}(0) \cdot \vec{\phi}_{-\mathbf{k}}(0))$ [32].

Power counting reveals the presence of two different upper critical dimensions coming from the quartic term ($d_c^u = 4$) and the cubic torque term ($d_c^g = 6$) in the action J . This implies that we have to evaluate the fixed points and exponents in a double power series expansion in $\epsilon = 4 - d$ and $\varepsilon = 6 - d$ [35].

The unperturbed correlation $C_{\mathbf{k}}^0(t_1, t_2) = \langle \vec{\phi}_{\mathbf{k}}(t_1) \cdot \vec{\phi}_{-\mathbf{k}}(t_2) \rangle$ and response $G_{\mathbf{k}}^0(t_1, t_2) = \langle \vec{\phi}_{\mathbf{k}}(t_1) \cdot \vec{\phi}_{-\mathbf{k}}(t_2) \rangle$ functions calculated from the quadratic part of the MSR action, and the bare u and g vertices are shown in Fig.2.30.

(a)  $\equiv \theta(t_1 - t_2) e^{-\Gamma \mathbf{k}^2 (t_1 - t_2)}$

(b)  $\equiv \frac{1}{k^2} [e^{-\Gamma \mathbf{k}^2 |t_1 - t_2|} - (\frac{k^2}{k_0^2} - 1) e^{-\Gamma \mathbf{k}^2 (t_1 + t_2)}]$

(c)  $\frac{1}{2} \Gamma g \epsilon_{\alpha\beta\gamma} (k_1^2 - (k - k_1)^2)$  $-\frac{k^2}{3} \Gamma u (\delta_{\alpha\beta} \delta_{\gamma\delta} + \delta_{\alpha\delta} \delta_{\beta\gamma} + \delta_{\alpha\gamma} \delta_{\beta\delta})$

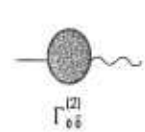
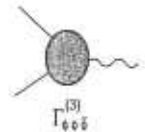
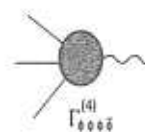
(d)  $\Gamma_{\phi\phi}^{(2)}$  $\Gamma_{\phi\phi\phi}^{(3)}$  $\Gamma_{\phi\phi\phi\phi}^{(4)}$

Figure 2.30: Unperturbed (a) response function $G_{\mathbf{k}}^0$, (b) correlation function $C_{\mathbf{k}}^0$, and the (c) two bare vertices u and g . Wavy and straight lines represent the $\vec{\phi}_{\mathbf{k}}(t)$ and $\vec{\phi}_{\mathbf{k}}(t)$ fields respectively. (d) Primitively divergent diagrams $\Gamma_{1,1}^0$, $\Gamma_{2,1}^0$ and $\Gamma_{3,1}^0$.

Again power counting shows that at $d = 3$, our perturbation expansion does not generate additional terms other than those already contained in J , i.e. the theory is renormalisable. However the perturbation theory gives rise to ultraviolet divergences which can be removed by adding counter-terms to the action. The perturbation is done in the dimensionless bare couplings $\bar{u}^B = \mu^{d-4} u^B$ and $\bar{g}^B = \mu^{d/2-3} g^B$, μ is any momentum scale. To remove these divergences, we introduce renormalisation factors (superscripts R and B denote renormalised and bare quantities respectively), $\vec{\phi}_{\mathbf{k}}^R(0) = (\tilde{Z} Z_0)^{-1/2} \vec{\phi}_{\mathbf{k}}^B(0)$, $\vec{\phi}_{\mathbf{k}}^R(t) = Z^{-1/2} \vec{\phi}_{\mathbf{k}}^B(t)$, $\vec{\phi}_{\mathbf{k}}^R(t) = \tilde{Z}^{-1/2} \vec{\phi}_{\mathbf{k}}^B(t)$, $u^R = Z_u^{-1} u^B$, $g^R = Z_g^{-1} g^B$, $\Gamma^R = Z_\Gamma^{-1} \Gamma^B$ and $\tau_0^R = Z_{\tau_0}^{-1} \tau_0^B$. The one particle irreducible correlation function $\Gamma_{N,\bar{N}}^{\bar{M}}$, with N external $\phi_{\mathbf{k}}(t)$ fields, \bar{N} external $\vec{\phi}_{\mathbf{k}}(t)$ fields and \bar{M} external $\phi_{\mathbf{k}}(0)$ fields is renormalised as

$$\Gamma_{N,\tilde{N}}^{(R)\tilde{M}} = Z^{-N/2} \tilde{Z}^{-\tilde{N}/2} (\tilde{Z} Z_0)^{-\tilde{M}/2} \Gamma_{N,\tilde{N}}^{(B)\tilde{M}}. \quad (2.45)$$

Note all the renormalised couplings are dimensionless. Since the dynamics obeys detailed balance, it follows that the renormalisation factors Z and Z_u are equal to their values calculated in statics. Further the conservation of the order parameter forces $Z\tilde{Z} = 1$ to all orders. To order 1-loop the Z factors are given by (calculation details are given in Appendix IIC),

$$\begin{aligned} Z = \tilde{Z} = 1, \quad Z_u = \mu^{4-d}(1 - 3(n+8)u_R/\epsilon), \quad Z_g = \mu^{3-d/2}(1 - g_R^2/192\pi^3\epsilon), \\ Z_\Gamma = \mu^{-\zeta}(1 + g_R^2/192\pi^3\epsilon), \quad Z_{\tau_0} = \tilde{Z}/Z. \end{aligned} \quad (2.46)$$

Note u_R and g_R are dimensionless. Now using the fact that the bare correlation functions are independent of μ we can write down an renormalisation group equation using Eq. (2.45),

$$\left(\mu \partial_\mu + \zeta \Gamma \partial_\Gamma + \kappa r \partial_r + \beta_u \partial_u + \beta_g \partial_g + \frac{N}{2} \gamma + \frac{\tilde{N}}{2} \tilde{\gamma} + \frac{\tilde{M}}{2} (\tilde{\gamma} + \gamma_0) + \zeta \tau_0^{-1} \partial \tau_0^{-1} \right) \Gamma_{N,\tilde{N}}^{(R)\tilde{M}} = 0, \quad (2.47)$$

with

$$\zeta = \mu \partial_\mu \ln \Gamma, \quad \kappa = \mu \partial_\mu \ln r, \quad \beta_u = \mu \partial_u u, \quad \beta_g = \mu \partial_g g, \quad \gamma = \mu \partial_\mu \ln Z, \quad \tilde{\gamma} = \mu \partial_\mu \ln \tilde{Z},$$

and $\gamma_0 = \mu \partial_\mu \ln Z_0$. All the derivatives are calculated at fixed ‘bare’ coupling value. The new stable fixed point given by the zeroes of the β functions (β_u and β_g) of the theory, is to order 1-loop, $g^* = \pm \sqrt{192\pi^3\epsilon} + \mathcal{O}(\epsilon^{3/2})$ [31], $u^* = (8/11)\pi^2\epsilon + \mathcal{O}(\epsilon^2)$ (note that u^* does not change from its WF value to all loops). The dynamical exponent $z = 4 + \zeta^* = 4 - \epsilon/2 + \mathcal{O}(\epsilon^2)$ [35, 33], where ζ^* is ζ evaluated at the fixed point (see Appendix IIC).

The λ exponent can be computed from the response function $G_{\mathbf{k}}(t, 0) \equiv \langle \vec{\phi}_{\mathbf{k}}(0) \cdot \vec{\phi}_{-\mathbf{k}}(t) \rangle$ since this is equal to the autocorrelation function $\tau_0^{-1} \langle \vec{\phi}_{\mathbf{k}}(t) \cdot \vec{\phi}_{-\mathbf{k}}(0) \rangle$, as can be seen from the first term in J on integrating by parts. It turns out this is the only two point correlator with a time at $t = 0$ to be renormalised to make the theory finite [32]. The response function gets renormalised to

$$G_{\mathbf{k}}^R(t, 0) = (Z_0 Z \tilde{Z})^{-1/2} G_{\mathbf{k}}^B(t, 0). \quad (2.48)$$

The divergent contributions to G_B could come from two sources. Each term in the double perturbation series could contain the primitively divergent subdiagrams $\Gamma_{1,1}^0$, $\Gamma_{2,1}^0$ or $\Gamma_{3,1}^0$, which we have already accounted for by replacing these by their renormalised counterparts. The other divergent contribution could arise from the primitive divergences of the 1-particle reducible vertex function $\Gamma^{(2)}(\mathbf{k}, t, 0)$, defined by $G_{\mathbf{k}}(t, 0) \equiv \int G_{\mathbf{k}}(t - t') \Gamma^{(2)}(\mathbf{k}, t', 0) dt'$. The superficial divergence of the diagrams contributing to $G_{\mathbf{k}}(t, 0)$ is $D = V_u(d - 4) + \frac{V_g}{2}(d - 6) - 2$ (where V_u (V_g) is the number of u (g) vertices respectively). This is negative for all d . For (a) $d > 6$, the only stable fixed point is the Gaussian fixed point and so $D = -2$, (b) $4 < d \leq 6$, u is irrelevant and so $D = \frac{V_g}{2}(d - 6) - 2 < 0$ and (c) $d \leq 4$, D is clearly negative. This implies that $G_{\mathbf{k}}^B(t, 0)$ does not get renormalised and $Z_0 = 1$. Consequently λ stays at its mean-field value of d (Appendix IIC) for this conserved Heisenberg dynamics both with and without the torque.

We conclude this section by stating that we have shown that for quenches to T_c , the torque is irrelevant for the nonconserved dynamics at the Wilson-Fisher fixed point. In the conserved case the torque is relevant at the WF fixed point with exponents $z = 4 - \varepsilon/2$ and $\lambda = d$ (where $\varepsilon = 6 - d$). We found to all orders in perturbation theory that $\lambda = d$ which follows as a consequence of the conservation of total magnetisation.

2.3 Conclusions and Future Work

In this study we have investigated the effect of inertia on the phase ordering dynamics of Heisenberg magnet where the spins precess about the local molecular field. We consider the cases when the order parameter is either nonconserved or conserved. For the nonconserved dynamics, we find that the inertia is irrelevant at late times both for a $T = 0$ and a $T = T_c$ quench. The situation is entirely different when the order parameter is conserved. In this case inertia is relevant driving the zero-temperature ordering dynamics to a new fixed point, characterised by exponents $z = 2$ and $\lambda \approx 5$. We find that at late times the dynamics cannot be described in terms of the dynamics of defects alone, which results in the failure of the standard Mazenko approximation. The torque term leads to longer lived spin-wave excitations which interact strongly with the defects, leading to a different scaling behaviour.

An accurate approximation scheme when inertial effects are present in the dynamics should incorporate the interaction between defects and spin-waves. We intend to work on this aspect in future. In the limit when the dynamics is provided solely by inertia (*pure torque dynamics*) the short wavelength spin-waves scatter off the randomly placed immobile defects, mimicking a 'heat-bath' coupled to the longer wavelength spin-waves which coarsen in time. A detailed study to understand this dynamics is under progress. For quenches to T_c , we use dynamical renormalisation group arguments to show that the torque is relevant at the conventional Wilson-Fisher fixed point.

2.4 Appendix IIA

In this Appendix we explicitly show the existence of a single length scale and hence standard scaling Eqs. (2.7, 2.8) in the late time dynamics of the conserved order parameter. Earlier, Coniglio and Zannetti [37] had explicitly shown that the late time dynamics of a conserved n -component spin model in the limit $n \rightarrow \infty$ reveals an infinity of length scales leading to a more complicated multiscaling form for the structure factor (Fourier transform of $C(\mathbf{r}, t)$),

$$S(k, t)(t)^{p(k/k_m)d}, \quad (2.49)$$

In the above multiscaling form, the structure factor grows in time, $L(t) \sim t^{1/4}$ with a scale dependent exponent $p(x) = 1 - (1 - x^2)^2$, where $x \equiv k/k_m$ and $k_m^{-1} \sim (t/\ln t)^{1/4}$ is the position of the maximum of $S(\mathbf{k}, t)$. This gave rise to the speculation that this multiscaling behaviour might be a generic feature of the dynamics of conserved order parameters. Subsequent numerical studies [5, 38] have demonstrated that this is not true. Here we show following a method described in [5], that the structure factor $S(\mathbf{k}, t)$ of the conserved $n = 3$ model (Heisenberg) does not obey multiscaling.

The method [5] demands a very accurate determination of $S(\mathbf{k}, t)$. Since the numerical evaluation of $S(\mathbf{k}, t)$ is subject to large errors (especially at small k), we fit a function $C_f(\mathbf{r}, t)$ to the computed $C(\mathbf{r}, t)$ and then calculate the Fourier transform $S_f(\mathbf{k}, t)$. The fitting function for $C_f(\mathbf{r}, t)$ has been taken as $\{\sin(r/L)/(r/L)\}(1 + a(r/L)^2) \exp(-b(r/L)^2)$ which is similar to the analytic form given in [30]. Note that only b and L are independent fitting parameters, a is determined by the condition $S_f(k = 0, t) = 0$. We now plot $S_f(k, t)$ versus t at fixed values of $x = k/k_m$ (Fig. 2.31). The resulting straight lines labeled by different values of x all show a constant slope of approximately 3/4 (Fig. 2.31). Using the proposed multiscaling form a plot of $p(x)$ versus x (inset Fig. 2.31) shows that $p(x)$ is clustered around 1. The small spread of $p(x)$ around 1 indicates that we have not quite reached the asymptotic regime, and it is likely that the late time $p(x) \rightarrow 1$ in agreement with conventional scaling. In addition, note that the form of $p(x)$ is qualitatively different from the downward curving $p(x)$ predicted by Coniglio and Zannetti [37]. We conclude then that the correlation function $C(\mathbf{r}, t)$ for the $n = 3$ conserved model does not obey multiscaling

and standard scaling with a single length scale $L(t)$ holds.

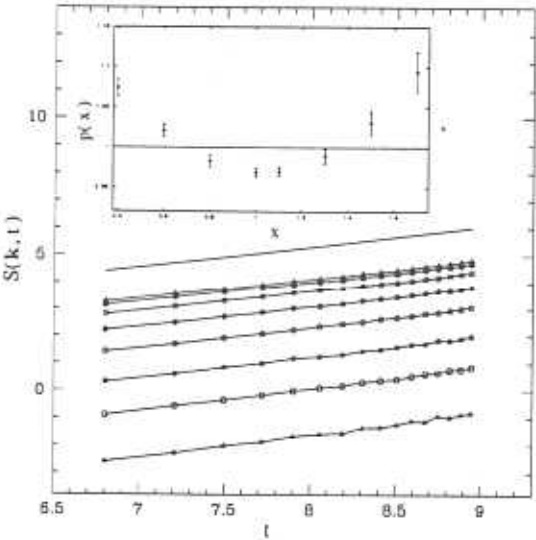


Figure 2.31: Plot of $S(k, t)$ vs t for $x = 0.4$ (circle), $x = 0.6$ (pentagon), $x = 0.8$ (square), $x = 1.0$ (triangle), $x = 1.1$ (filled circle), $x = 1.3$ (filled pentagon), $x = 1.5$ (filled square), $x = 1.7$ (filled triangle). A straight line of slope $3/4$ is given for comparison. Inset figure shows plot of $p(x)$ with x . Note that the errors in $p(x)$ increases as $|x - 1|$ increases because of the smallness of $S(k, t)$ near its wings.

2.5 Appendix IIB

In this Appendix we study the effect of spin-wave excitations on the time dependent pre-asymptotic equal-time correlation function. We would like to show that inclusion of such excitations in the correlation function $C(r, t)$ leads to a dip at pre-asymptotic times when $g \neq 0$, which eventually relaxes. As suggested in Sect. 2.1.1 A, at very late times the order parameter field has totally relaxed with respect to defect cores. Pre-asymptotic configurations typically consist of spin wave excitations interspersed between slowly moving defect cores. These defect cores are separated by a typical distance $L(t) \gg \xi$, the size of the defect core. In general one can decompose $\vec{\phi}(\mathbf{r}, t) = \vec{\phi}_{sing}(\mathbf{r}, t) + \vec{\phi}_{sm}(\mathbf{r}, t)$, where the singular part $\vec{\phi}_{sing}$ parameterizes defect configurations while the smooth part $\vec{\phi}_{sm}$ is a linear combination of spin-waves of wave-vector \mathbf{k} , $\vec{\phi}_{sm}(\mathbf{r}, t) = V^{-1/2} \sum \vec{\phi}_{\mathbf{k}}^{sm}(t) e^{i\mathbf{k} \cdot \mathbf{r}}$. The pre-asymptotic correlation function will thus have three contributions : $C_{sing} \equiv \langle \vec{\phi}_{sing}(0, t) \cdot \vec{\phi}_{sing}(\mathbf{r}, t) \rangle$, $C_{sm} \equiv \langle \vec{\phi}_{sm}(0, t) \cdot \vec{\phi}_{sm}(\mathbf{r}, t) \rangle$ and the scattering of spin-waves from slowly moving defects $C_{scat} \equiv \langle \vec{\phi}_{sm}(0, t) \cdot \vec{\phi}_{sing}(\mathbf{r}, t) \rangle$. At late times of course $\vec{\phi}_{\mathbf{k}}^{sm}(t) \rightarrow 0$, and $\vec{\phi}_{sing}$ can be traded off for the auxiliary field \vec{m} within the Mazenko approach. Thus the $C_{sing}(r, t)$ part of the correlation function is given by the solution of Eq. (2.32) or the BPT form [9].

The smooth part of the correlation function $C_{sm}(r, t)$ can be estimated from a perturbative calculation wherein the defects separated by a distance $L \gg \xi$ are taken to be static (justified post priori). We shall see that the dip is a result of this smooth part. Confining our attention to a single domain of size L , we can split the smooth $\vec{\phi}_{sm}$ into transverse and longitudinal components about the well-defined broken symmetry axis taken to be along $\alpha=3$. Thus $\phi_{\alpha}^{sm}(\mathbf{r}, t) = \phi_{eq} \delta_{\alpha 3} + u_{\alpha}(\mathbf{r}, t)$, where the equilibrium magnetisation $\phi_{eq} = 1$.

Consider an initial smooth localised pulse in the interior of this domain of the form $u_1(\mathbf{r}, 0) = u_2(\mathbf{r}, 0) = \frac{u(0)}{(2\sigma)^3 \pi^{3/2}} e^{-r^2/4\sigma^2}$ and $u_3(\mathbf{r}, 0) = \frac{u_3(0)}{(2\omega)^3 \pi^{3/2}} e^{-r^2/4\omega^2}$, where the widths $\sigma, \omega \ll L$ and $u(0), u_3(0) \ll 1$. The equation for u_{α} can be read out from Eq. (2.3),

$$\begin{aligned} \frac{\partial u_{\alpha}}{\partial t} = & \nabla^2 u_{\alpha} - g \epsilon_{\alpha\beta 3} \nabla^2 u_{\beta} - 2u_3 \delta_{\alpha 3} \\ & - (u_{\beta} u_{\beta}) \delta_{\alpha 3} - 2(u_{\alpha} u_{\beta}) \delta_{\beta 3} \end{aligned}$$

$$+g\epsilon_{\alpha\beta\gamma}u_{\beta}\nabla^2u_{\gamma}-u_{\beta}u_{\beta}u_{\alpha}. \quad (2.50)$$

To solve this equation perturbatively, we multiply the nonlinear terms in Eq. (2.50) by an arbitrary real parameter $\epsilon (\leq 1)$ and express $u_{\alpha}(\mathbf{r}, t)$ as $\sum_{n=0}^{\infty} \epsilon^n u_{\alpha}^{(n)}(\mathbf{r}, t)$. The initial conditions for $u_{\alpha}^{(n)}(\mathbf{r}, 0)$ follow from $u_{\alpha}(\mathbf{r}, 0)$. We are interested in solutions that decay as $t \rightarrow \infty$. Convergence of the perturbation series at $\epsilon = 1$ is guaranteed by the smallness of the initial deviation and because higher-order terms in the expansion decay faster. To $\mathcal{O}(\epsilon^0)$, the spin-waves do not interact and

$$\frac{\partial u_{\alpha}^{(0)}}{\partial t} = \nabla^2 u_{\alpha}^{(0)} - g\epsilon_{\alpha\beta 3} \nabla^2 u_{\beta}^{(0)} - 2u_3^{(0)} \delta_{\alpha 3}. \quad (2.51)$$

The equations for $u_1^{(0)}$ and $u_2^{(0)}$ decouple in the variables $u_{\pm}^{(0)} = (u_1^{(0)} \pm iu_2^{(0)})/2$, giving rise to two precessing Goldstone modes in the transverse direction and an exponentially decaying mode in the longitudinal direction. Thus,

$$u_{\pm}^{(0)}(\mathbf{r}, t) = \frac{(1 \pm i)u(0)}{16(\pi t(1 \pm ig))^{3/2}} \exp\left(-\frac{r^2}{4(1 \pm ig)t}\right),$$

and

$$u_3^{(0)}(\mathbf{r}, t) = \frac{u_3(0)}{8(\pi t)^{3/2}} \exp\left(-\frac{r^2}{4t} - 2t\right), \quad (2.52)$$

are the asymptotic solutions to $\mathcal{O}(\epsilon^0)$.

To $\mathcal{O}(\epsilon)$, the dynamical equations in the transverse variables are given by,

$$\begin{aligned} \frac{\partial u_{\pm}^{(1)}}{\partial t} = & (1 \pm ig) \nabla^2 u_{\pm}^{(1)} - 2u_3^{(0)} u_{\pm}^{(0)} \pm ig(u_3^{(0)} \nabla^2 u_{\pm}^{(0)} - u_{\pm}^{(0)} \nabla^2 u_3^{(0)}) \\ & - (4u_+^{(0)} u_-^{(0)} + (u_3^{(0)})^2) u_{\pm}^{(0)}. \end{aligned} \quad (2.53)$$

The last two terms are sub-dominant in $1/t$ and $u(0), u_3(0)$ respectively, and so the transverse correlator to $\mathcal{O}(\epsilon)$ is given by

$$\begin{aligned}
C_{sm}^{\perp}(\mathbf{r}, t) &= \frac{1}{2} \langle u_+(\mathbf{x}, t) u_-(\mathbf{x} + \mathbf{r}, t) + u_+(\mathbf{x} + \mathbf{r}, t) u_-(\mathbf{x}, t) \rangle \\
&\sim \frac{A_1}{t^{3/2}} \exp\left(-\frac{r^2}{8t}\right) + \frac{A_2 e^{-2t}}{t^3} \exp\left(-\frac{r^2}{2t(3+g^2)}\right) \\
&\quad \times \left\{ \cos\left(\frac{gr^2}{4t(3+g^2)} + \pi/4\right) \right\}, \tag{2.54}
\end{aligned}$$

where $A_1 \sim O(u(0)^2)$ and $A_2 \sim O(u(0)^2 u_3(0))$ are constants depending on g and initial conditions. The cosine term in the above expression results in the observed dip of the total correlation function. The magnitude of the dip increases with increasing g .

The dynamical equation for the longitudinal component to $O(\epsilon)$ is likewise given by

$$\begin{aligned}
\frac{\partial u_3^{(1)}}{\partial t} &= (\nabla^2 - 2) u_3^{(1)} - (4u_+^{(0)} u_-^{(0)} + 3(u_3^{(0)})^2) \\
&\quad + 2ig(u_+^{(0)} \nabla^2 u_-^{(0)} - u_-^{(0)} \nabla^2 u_+^{(0)}) \\
&\quad - (4u_+^{(0)} u_-^{(0)} + (u_3^{(0)})^2) u_3^{(0)} \tag{2.55}
\end{aligned}$$

As before, the terms proportional to $(u_3^{(0)})^2$, the gradient terms and the cubic term are sub-dominant, and so the decay of the longitudinal correlation function C_{sm}^{\parallel} is given by

$$\begin{aligned}
C_{sm}^{\parallel}(\mathbf{r}, t) &= \langle \phi_3(\mathbf{x}, t) \phi_3(\mathbf{x} + \mathbf{r}, t) \rangle \\
&\sim \frac{B_1 e^{-4t}}{t^{3/2}} \exp\left(-\frac{r^2}{8t}\right) - \frac{B_2 e^{-2t}}{t^3} \exp\left(-\frac{r^2}{2t(3+g^2)}\right) \\
&\quad + \frac{B_3}{t^{9/2}} \exp\left(-\frac{r^2}{4t(1+g^2)}\right), \tag{2.56}
\end{aligned}$$

where $B_1 \sim O(u_3(0)^2, u(0)^2)$, $B_2 \sim O(u(0)^2 u_3(0), u(0)^3)$ and $B_3 \sim O(u(0)^4)$ are functions of g and initial conditions.

Note that C_{sm}^{\perp} evolves with a width that scales as $t^{1/2}$ and an amplitude which decreases as $t^{-3/2}$. The longitudinal C_{sm}^{\parallel} decays exponentially fast. This decay is consistent with our earlier assertion that the defects separated by a distance $L(t)$ hardly move over time scales corresponding to spin-wave relaxation.

The cross correlator C_{scat} coming from the scattering of spin-waves by moving defects can be calculated by treating ϕ_{sm} as “slaved” to ϕ_{sing} . As the defects move they excite spin-waves which decay in a time scale smaller than the time taken by the defects to move any further. The dominant contribution to C_{scat} comes from the product of Eq. (2.52) and ϕ_{sing} . It is easy to see that this term leads to the same cosine dip as in Eq. (2.54) but with an amplitude that decays algebraically in time. This is the source of the slow decay of the dip.

2.6 Appendix IIC

We present the details of the perturbative calculation for the critical quench dynamics of Model J for the $n = 3$ Heisenberg model. First we compute the superficial divergence or engineering dimension D (in momentum scale) of a 1-particle irreducible graph $\Gamma_{N,\tilde{N}}$,

$$D = V_u(d-4) + \frac{V_g}{2}(d-6) - \frac{E}{2}(d-2) - 4x_u - 2x_g - [x_g] + d + 4 \quad (2.57)$$

Here V_u and V_g are the number of u and g vertices, $E = N + \tilde{N}$ is the number of external legs, x_u and x_g are the number of internal legs originating from the u and g vertices respectively, and $[x_g] = x_g + 1$ if x_g is odd, $[x_g] = x_g$ if x_g is even. We will find that $\Gamma_{N,\tilde{N}} = 0$ for $\tilde{N} = 0$, which follows from the causal nature of the response function. This can be seen from the following simple argument. The number of correlators in a graph if $\tilde{N} = 0$ is $C = V_u + V_g/2 - E/2$, and the number of loops in a graph is $L = V_u + V_g/2 - E/2 + 1$. Hence $L = C + 1$. This means that at least a loop in the graph is made up of only response functions, which vanishes because of causality. Clearly Eq.(2.57) shows that there are two critical dimensions in the theory, $d_c^u = 4$ and $d_c^g = 6$. Consequently we have three regimes.

I. $d > 6$ The Gaussian fixed point ($g^* = 0, u^* = 0$) is a stable fixed point. Therefore the theory is exact here.

II. $4 < d \leq 6$ In this regime $u^* = 0$ is the stable fixed point, therefore $V_u = 0$, so all graphs are to be computed at $d_c^g = 6$. The only divergent diagrams are $\Gamma_{1,1}^{(2)}$ and $\Gamma_{2,1}^{(3)}$ with the degree of divergence 2 and 0 respectively.

III. $2 < d \leq 4$ Both u^* and g^* are non zero at the stable fixed point, and so the graphs are to be calculated at $d_c^u = 4$. $\Gamma_{1,1}^{(2)}$ with $D = 2$ (when $V_g = 0$) and $D = 0$ (when $V_g = 2$), $\Gamma_{2,1}^{(3)}$ with $D = 0$ and $\Gamma_{3,1}^{(4)}$ with $D = 0$ are the only divergent diagrams.

Having separated the divergent diagrams we isolate the divergent piece of the graphs as poles of $\epsilon \rightarrow 0$ and $\varepsilon \rightarrow 0$ or in other words perform dimensional regularisation of the diagrams [39].

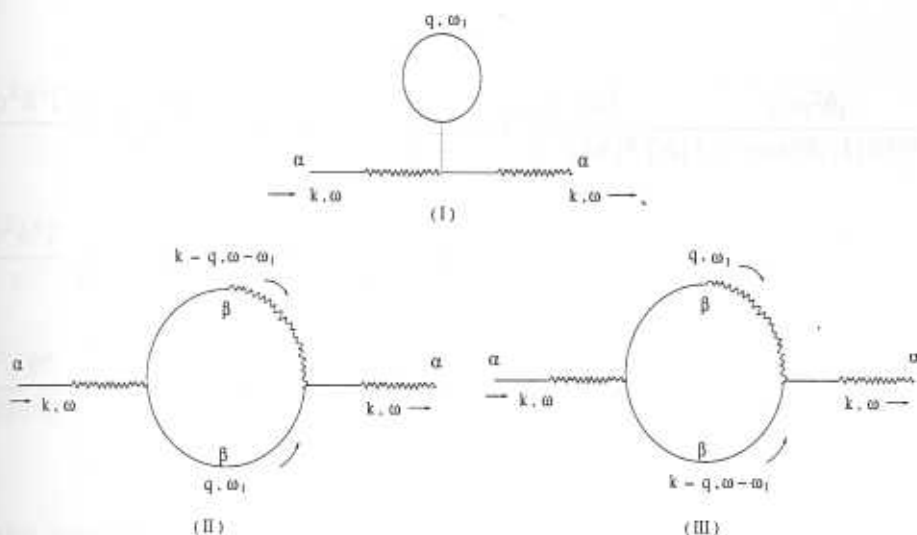


Figure 2.32: (I) shows the 1-loop contribution to the response coming from the u -vertex alone. (II) and (III) give the contributions from the g -vertex at 1-loop.

Regularisation of $\Gamma_{1,1}^{(2)}$

The contribution coming from Fig. 2.32(I) does not depend on external momenta; it therefore only changes the critical point T_c . The diagrams Fig. 2.32(II) and 2.32(III) give

$$\begin{aligned}
 & \frac{g^2 \Gamma^2}{4} \int \frac{d^d q}{(2\pi)^d} \frac{d\omega_1}{2\pi} \left[(q^2 - (\mathbf{k} - \mathbf{q})^2)(q^2 - k^2) G^0(\mathbf{k} - \mathbf{q}, \omega - \omega_1) C^0(q, \omega_1) \right. \\
 & \quad \left. + ((\mathbf{k} - \mathbf{q})^2 - q^2)((\mathbf{k} - \mathbf{q})^2 - k^2) G^0(q, \omega_1) C^0(\mathbf{k} - \mathbf{q}, \omega - \omega_1) \right] \\
 &= \frac{g^2 \Gamma^2}{4} \int \frac{d^d q}{(2\pi)^d} \frac{d\omega_1}{2\pi} \left[(q^2 - (\mathbf{k} - \mathbf{q})^2)(q^2 - k^2) \frac{2\Gamma q^2}{(\Gamma(\mathbf{k} - \mathbf{q})^4 - i(\omega - \omega_1))(\Gamma^2 q^8 + \omega_1^2)} \right. \\
 & \quad \left. + ((\mathbf{k} - \mathbf{q})^2 - q^2) \frac{2\Gamma(\mathbf{k} - \mathbf{q})^2}{(\Gamma q^4 - i\omega_1)(\Gamma^2(\mathbf{k} - \mathbf{q})^8 + (\omega - \omega_1)^2)} \right] \\
 &= \frac{g^2 \Gamma^2}{4} \int \frac{d^d q}{(2\pi)^d} \frac{k^2((\mathbf{k} - \mathbf{q})^2 - q^2)^2}{\Gamma q^2(\mathbf{k} - \mathbf{q})^2((\mathbf{k} - \mathbf{q})^4 + q^4)} \\
 &= g^2 k^2 \Gamma \int \frac{d^d q}{(2\pi)^d} \frac{(\mathbf{k} \cdot \mathbf{q})^2}{q^2(\mathbf{k} - \mathbf{q})^2((\mathbf{k} - \mathbf{q})^4 + q^4)}
 \end{aligned}$$

$$\begin{aligned}
&= 2g^2 k^4 \Gamma \int \frac{d\Omega}{(2\pi)^d} \cos^2 \theta_1 \int d^d q \frac{q^{d-1} A^3}{(q^2 + 2A(\mathbf{k} \cdot \mathbf{q}) + Ak^2)^3} \\
&\quad A = 1/(1 + i(x_1 - x_2)) \\
&= \frac{\Gamma g^2 k^4 \Gamma(d/2) \Gamma(3 - d/2)}{2} \int_0^1 dx_1 \int_0^1 dx_2 A^3 \int \frac{d\Omega}{(2\pi)^d} \frac{\cos^2 \theta_1}{(A(1 - \cos^2 \theta_1 A)k^2)^{3-d/2}} \\
&= \frac{2g^2 k^4 \Gamma}{\varepsilon} \int_0^1 dx_1 \int_0^1 dx_2 A^3 \int \frac{d\Omega}{(2\pi)^d} \cos^2 \theta_1 \\
&= \frac{g^2 \Gamma k^4}{192\pi^3 \varepsilon}.
\end{aligned} \tag{2.58}$$

This yields the recursion relation

$$\Gamma_B = Z_\Gamma \Gamma_R = \Gamma_R \mu^{-\zeta} \left(1 - \frac{g_R^2}{192\pi^3 \varepsilon}\right). \tag{2.59}$$

Regularisation of $\Gamma_{2,1}^{(3)}$

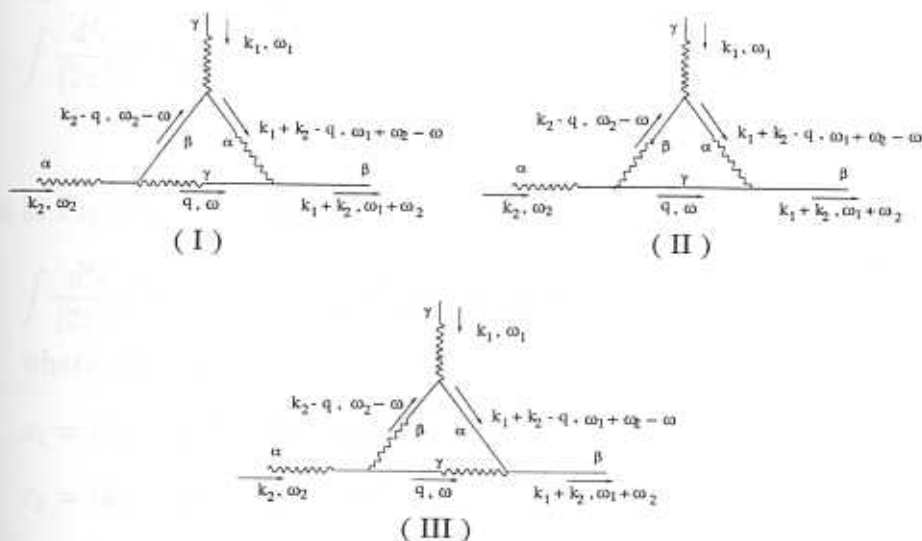


Figure 2.33: (I), (II) and (III) show the contributions coming from the g -vertex to the vertex function at 1-loop.

The diagram in Fig. 2.33(I) gives

$$\begin{aligned}
 & \int \frac{d^d q}{(2\pi)^d} \frac{d\omega}{2\pi} x_1 x_2 x_3 G(q, \omega) G(k_1 + k_2 - q, \omega_1 + \omega_2 - \omega) C(k_2 - q, \omega_2 - \omega) \\
 & \text{where, } \mathbf{K} = \mathbf{k}_1 + \mathbf{k}_2 \\
 & x_1 = (\mathbf{k}_2 - \mathbf{q})^2 - (\mathbf{K} - \mathbf{q})^2 \\
 & x_2 = (\mathbf{k}_2 - \mathbf{q})^2 - k_2^2 \\
 & x_3 = q^2 - K^2 \\
 & = \int \frac{d^d q}{(2\pi)^d} x_1 \left(\frac{3i}{4\Gamma q^6} \right).
 \end{aligned} \tag{2.60}$$

The diagram in Fig. 2.33(II) gives

$$\begin{aligned}
 & \int \frac{d^d q}{(2\pi)^d} \frac{d\omega}{2\pi} x_1 x_2 x_3 G(q, \omega) G(k_2 - q, \omega_2 - \omega) C(k_1 + k_2 - q, \omega_1 + \omega_2 - \omega) \\
 & \text{where, } \mathbf{K} = \mathbf{k}_1 + \mathbf{k}_2 \\
 & x_1 = (\mathbf{k}_2 - \mathbf{q})^2 - (\mathbf{K} - \mathbf{q})^2 \\
 & x_2 = k_1^2 - q^2 \\
 & x_3 = K^2 - (\mathbf{K}^2 - \mathbf{q})^2 \\
 & = \int \frac{d^d q}{(2\pi)^d} x_1 \left(\frac{-i}{2\Gamma q^6} \right).
 \end{aligned} \tag{2.61}$$

The diagram in Fig. 2.33(III) gives

$$\begin{aligned}
 & \int \frac{d^d q}{(2\pi)^d} \frac{d\omega}{2\pi} x_1 x_2 x_3 G(q, \omega) G(k_2 - q, \omega_2 - \omega) C(k_1 + k_2 - q, \omega_1 + \omega_2 - \omega) \\
 & \text{where, } \mathbf{K} = \mathbf{k}_1 + \mathbf{k}_2 \\
 & x_1 = (\mathbf{k}_2 - \mathbf{q})^2 - (\mathbf{K} - \mathbf{q})^2 \\
 & x_2 = (\mathbf{k}_1 + 2\mathbf{k}_2 - \mathbf{q})^2 - k_2^2 \\
 & x_3 = (\mathbf{k}_1 + 2\mathbf{k}_2 - \mathbf{q})^2 - K^2 \\
 & = \int \frac{d^d q}{(2\pi)^d} x_1 \left(\frac{-i}{4\Gamma q^6} \right).
 \end{aligned} \tag{2.62}$$

Note that Diagram I + Diagram II + Diagram III = 0.

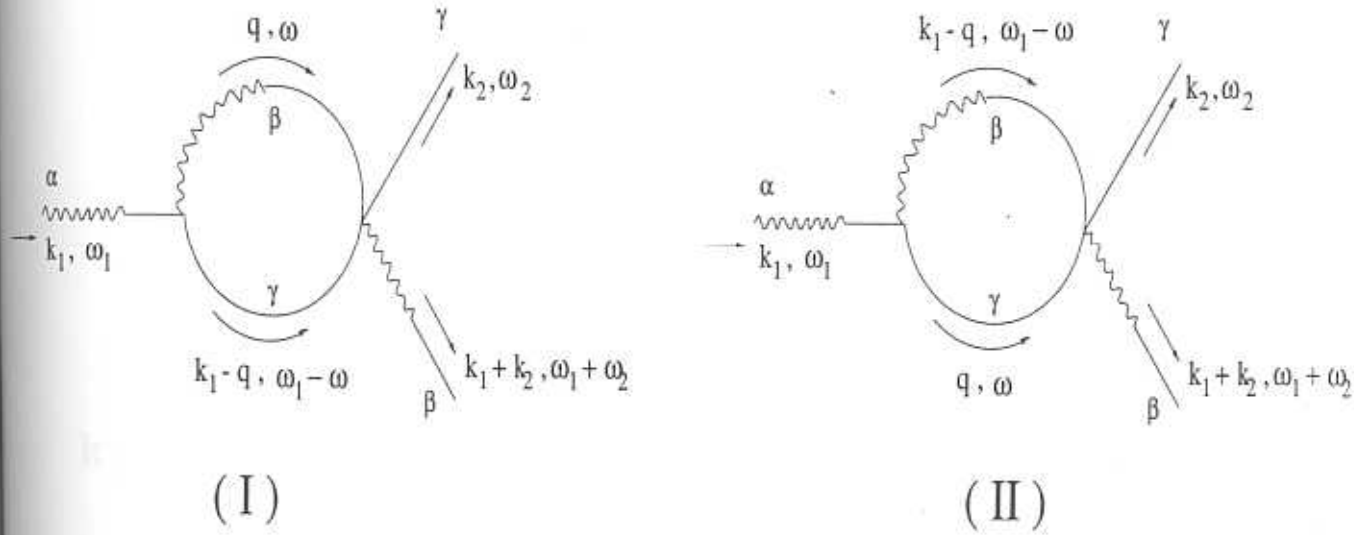


Figure 2.34: Graphs (I) and (II) give the contributions coming from the g - and u - vertices to the vertex function at 1-loop.

The diagram in Fig. 2.34(I) gives

$$\begin{aligned}
 & \frac{-guK^2}{3} \int d^d q d\omega_1 ((\mathbf{k}_1 - \mathbf{q})^2 - q^2) C(q, \omega) G(\mathbf{k}_1 - \mathbf{q}, \omega - \omega_1) \\
 &= \frac{-guK^2}{3} \int d^d q d\omega_1 ((\mathbf{k}_1 - \mathbf{q})^2 - q^2) \frac{1}{\Gamma^2 q^6}.
 \end{aligned} \tag{2.63}$$

The diagram in Fig. 2.34 II gives

$$\begin{aligned}
 & \frac{-guK^2}{3} \int d^d q d\omega_1 (q^2 - (\mathbf{k}_1 - \mathbf{q})^2) C(q, \omega) G(\mathbf{k}_1 - \mathbf{q}, \omega - \omega_1) \\
 &= \frac{guK^2}{3} \int d^d q d\omega_1 ((\mathbf{k}_1 - \mathbf{q})^2 - q^2) \frac{1}{\Gamma^2 q^6}.
 \end{aligned} \tag{2.64}$$

Again, Diagram I + Diagram II = 0. Hence there is no correction to the vertex function at 1-loop and recursion relation reduces to the scaling relation of the bare coupling :

$$g_B \Gamma_B = \mu^{3-d/2-\zeta} g_R \Gamma_R. \tag{2.65}$$

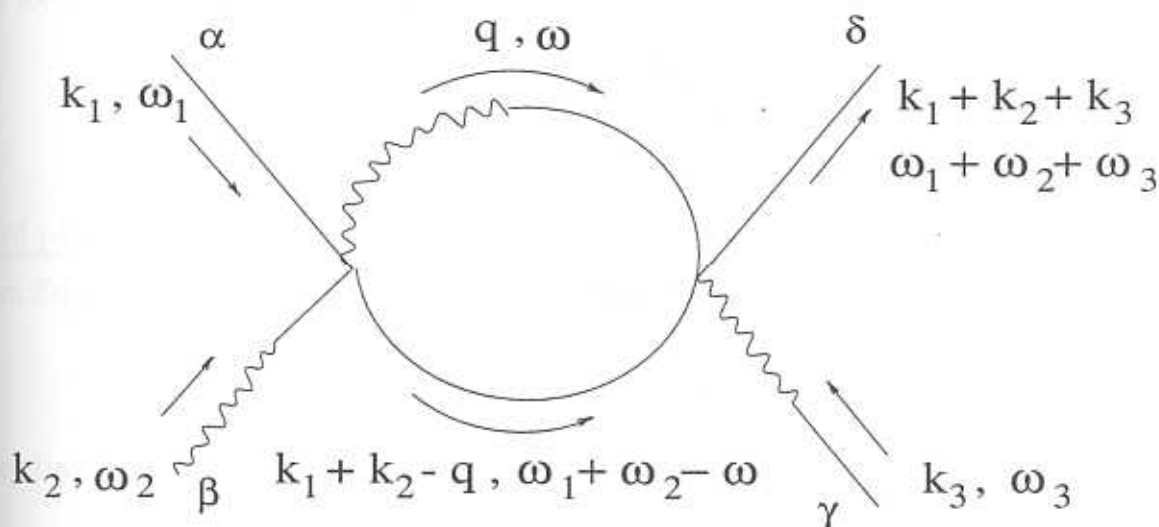
Regularisation of $\Gamma_{3,1}^{(4)}$ 

Figure 2.35: The divergent contribution coming from the u -vertex to the four point function at 1-loop.

The diagram in Fig. 2.35 gives

$$\begin{aligned} & \frac{36(n+8)(u\Gamma)^2 k_3^2}{9} \int \frac{d^d q}{(2\pi)^d} \frac{d\omega_1}{2\pi} \frac{2q^2 \Gamma(\mathbf{k}_1 + \mathbf{k}_2 - \mathbf{q})^8}{(\Gamma^2(\mathbf{k}_1 + \mathbf{k}_2 - \mathbf{q})^2 + (\omega_1 + \omega_2 - \omega)^2)(\Gamma q^4 - i\omega)} \\ &= 4(n+8)(u^2 \Gamma) k_3^2 \int \frac{d^d q}{(2\pi)^d} \frac{q^2}{((\mathbf{K} - \mathbf{q})^2 + q^4)((\mathbf{K} - \mathbf{q})^4 + q^4)} \end{aligned}$$

where, $\mathbf{K} = \mathbf{k}_1 + \mathbf{k}_2$

$$\begin{aligned} &= 4(n+8)(u^2 \Gamma) k_3^2 \int_0^1 dx \int \frac{d^d q}{(2\pi)^d} \frac{A^2}{(q^2 - 2A\mathbf{K} \cdot \mathbf{q} + AK^2)} \\ &= \frac{4(n+8)(u^2 \Gamma) k_3^2 \Gamma(2-d/2)}{(4\pi)^{d/2}} \int_0^1 dx \frac{A^2}{(AK^2(1 - A\cos^2\theta_1))^{2-d/2}} \\ &= \frac{(n+8)(u^2 \Gamma) k_3^2}{2\pi^2 \epsilon} \int_0^1 dx A^2 \end{aligned}$$

$$= \frac{(n+8)(u^2\Gamma)k_3^2}{4\pi^2\epsilon}. \quad (2.66)$$

The recursion relation is therefore

$$u_B = Z_u u_R = \mu^{4-d} u_R \left(1 - \frac{3(n+8)u_R}{4\pi^2\epsilon}\right). \quad (2.67)$$

Fixed points

From Eq.(2.59) and Eq. (2.65) we get the recursion relation in g ,

$$g_B = g_R \mu^{3-d/2} \left(1 - \frac{g_R^2}{192\pi^3\epsilon}\right). \quad (2.68)$$

Operating by $\mu \frac{\partial}{\partial \mu}$ on both the sides of Eq. (2.68),

$$\begin{aligned} \mu \frac{\partial g_B}{\partial \mu} = 0 &= \mu \frac{\partial}{\partial \mu} \left(\mu^{4-d} g_R \left(1 - \frac{g_R^2}{192\pi^3\epsilon}\right) \right) \\ \Rightarrow \mu \frac{\partial g_R}{\partial \mu} &= \frac{\epsilon}{2} g_R - \frac{g_R^3}{192\pi^3} + O(g_R^3) = \beta_g. \end{aligned} \quad (2.69)$$

$$(2.70)$$

This equation admits three fixed points, $g^* = 0$ and $g = \pm \epsilon/96\pi^{3/2}$. For $d \leq 6$ the nonzero g^* is the stable fixed point and for $d > 6$, $g^* = 0$ is the stable fixed point. Operating by $\mu \frac{\partial}{\partial \mu}$ on both the sides of Eq. (2.67),

$$\begin{aligned} \mu \frac{\partial u_B}{\partial \mu} = 0 &= \mu \frac{\partial}{\partial \mu} \left(\mu^{4-d} u_R \left(1 - \frac{3(n+8)u_R}{4\pi^2\epsilon}\right) \right) \\ \Rightarrow \mu \frac{\partial u_R}{\partial \mu} &= \epsilon u_R - \frac{3(n+8)u_R}{4\pi^2} u_R^2 + O(u_R^3) = \beta_u. \end{aligned} \quad (2.71)$$

Equation (2.71) has two fixed points, $u^* = 0$ (Gaussian fixed point) and $u^* = 4\pi^2/3(n+8)$ (Wilson-Fisher fixed point). For $d > 4$ the Gaussian fixed point is stable, which for $d \leq 4$ the Wilson-Fisher fixed point is stable. This follows from a stability analysis of Eq. (2.71) about the fixed points.

Exponents

The z exponent can be calculated from the relation $z = 4 + \zeta^*$. ζ^* is calculated using the fluctuation-dissipation relation which involves renormalisation of the composite operator $\vec{\phi} \times \vec{\phi}$. Details of the calculation can be found in Ref. [33]. To $O(\varepsilon)$, $\zeta^* = -\varepsilon/2$ which makes $z = 4 - \varepsilon/2$.

The mean field value of λ is calculated by taking the Fourier transform of $C_{\mathbf{k}}(t, 0) = (1/\tau_0) \exp(-\Gamma k^4 t)$ at $r = 0$ which gives

$$\begin{aligned} A(t) &= \frac{1}{\tau_0} \int d^d k \exp(-\Gamma k^4 t) \\ &= \frac{\pi^{d/2}}{4\tau_0 \Gamma(d/2)} \left(\frac{1}{\Gamma t^{1/4}} \right)^d, \end{aligned} \quad (2.72)$$

which implies $\lambda = d$.

Bibliography

- [1] P. C. Hohenberg and B. I. Halperin, *Rev. Mod. Phys.* **49**, 435 (1977).
- [2] P. M. Chaikin and T. C. Lubensky in *Principles of Condensed Matter Physics* (Cambridge University Press, Cambridge, 1995).
- [3] J. D. Gunton, M. San Miguel and P. S. Sahni in *Phase Transitions and Critical Phenomena*, Vol. 8, eds. C. Domb and M. Green (Academic Press, NY, 1983).
- [4] N. Mason, A. N. Pargellis and B. Yurke, *Phys. Rev. Lett.* **70**, 190 (1993).
- [5] M. Seigert and M. Rao, *Phys. Rev. Lett.* **70**, 1956 (1993).
- [6] W. H. Press, S. A. Teukolsky, W. T. Vetterling and B. P. Flannery in *Numerical Recipes in Fortran*, 2nd ed. (Cambridge University Press, Cambridge, 1992).
- [7] J. Das and M. Rao, *Phys. Rev. E* **57**, 5069 (1998).
- [8] J. Das and M. Rao, *Physica A* **270**, 253 (1999).
- [9] A. J. Bray, and S. Puri, *Phys. Rev. Lett.* **67**, 2670 (1991); H. Toyoki, *ibid.*, **45**, 1995 (1992).
- [10] A. J. Bray *Adv. Phys.* **43**, 357 (1994).
- [11] G. F. Mazenko, *Phys. Rev. B* **43**, 5747 (1991) ; A. J. Bray and K. Humayum, *J. Phys. A* **25**, 2191 (1992).
- [12] C. Yeung, M. Rao and R. C. Desai, *Phys. Rev. E* **53**, 2621 (1994).

- [13] F. J. Wegner, Phys. Rev. B **5**, 4529 (1972) ; C. J. Camacho and M. E. Fisher, J. Chem. Phys. **94**, 5493 (1991).
- [14] D. Stauffer, M. Ferer and M. Wortis, Phys. Rev. Lett. **29**, 345 (1972).
- [15] A. J. Bray, private communication.
- [16] K. Damle, S. Majumdar and S. Sachdev, Phys Rev A **54**, 5037 (1996).
- [17] A. J. C. Ladd, H. Gang and D. A. Weitz, Phys. Rev. E **52**, 6550 (1995).
- [18] J. Tjon and J. Wright, Phys. Rev. B **15**, 3470 (1977).
- [19] H. C. Fogedby, J. Phys. A **13** 1476 (1980).
- [20] M. E. Fisher in *Critical Phenomena, Proceedings of the Summer School held at University of Stellenbosch, South Africa, Jan. 18-29, 1982* (Springer-Verlag, Heidelberg, 1983).
- [21] J. Villain, in *Scaling Phenomena in Disordered Systems*, eds. R. Pynn and A. Skjeltorp, NATO ASI Ser. B, Vol. 133 (Plenum, NY, 1985) ; T. Natterman and J. Villain, Phase Transitions **11**, 5 (1988).
- [22] M. Rao and A. Chakrabarti, Phys. Rev. Lett. **71**, 3501 (1993).
- [23] C. M. Bender and S. Orzag in *Advanced Mathematical Methods for Scientists and Engineers*, (McGraw-Hill, NY, 1978).
- [24] S. De Siena and M. Zannetti, Phys. Rev. E **50**, 2621 (1994).
- [25] J. Das and M. Rao, Phys. Rev. E **62**, 1601 (2000).
- [26] G. Brown, P. A. Rikvold, M. Sutton and M. Grant, Phys. Rev. E **60** , 5151 (1999).
- [27] C. Yeung, A. Shinozaki and Y. Onno, Phys. Rev. E **49**, 2693 (1994).
- [28] G. F. Mazenko, Phys. Rev. E **49**, 3717 (1994).

- [29] M. Abramovitz and I. A. Stegun in *Handbook of Mathematical Functions* (Dover, NY, 1970).
- [30] F. R. Iniguez and A. J. Bray, Phys. Rev. E **51**, 188 (1995).
- [31] S. K. Ma and G. F. Mazenko, Phys. Rev. B **11**, 4077 (1975).
- [32] H. K. Janssen, B. Schaub and B. Schmittman, Z. Phys. B **73**, 539 (1989) ; H. K. Janssen in *From Phase Transitions to Chaos*, eds. G. Györgyi et.al. (World Scientific, Singapore, 1992).
- [33] R. Bausch, H. K. Janssen and H. Wagner, Z. Phys. B **24**, 113(1976).
- [34] J. G. Kissner, Phys. Rev. B **46**, 2676 (1992).
- [35] S. K. Ma in *Modern Theory of Critical Phenomen* (W. A. Benjamin Inc. , Massachusetts, 1976).
- [36] S. Majumdar, D. Huse and B. Lubachevsky, Phys. Rev. Lett. **73**, 182 (1995) ; M. Rao, ICTP preprint, IC/94/137.
- [37] A. Coniglio and M. Zannetti, Europhys. Lett. **10** 57 (1989).
- [38] M. Rao and A. Chakrabarti, Phys. Rev. E **49** 3727 (1994).
- [39] M. Veltmann in *Diagrammatica : The Path to Feynmann Rules* (Cambridge University Press, Cambridge, 1994).

Chapter 3

Dissipative Dynamics of Driven Heisenberg magnets

In this chapter we study the dynamics of Heisenberg spins in d -dimensions subject to an external anisotropic driving (not derivable from a Hamiltonian) in the presence of dissipation and inertia. We begin this chapter by deriving the equations of motion for the model (Sect. 3.1) both from symmetry arguments and by analysing a specific lattice model. We show that the 'high temperature' steady state of the model is paramagnetic (Sect. 3.2). There exists a 'critical phase' where the system exhibits power law correlations; the exponents are determined using a dynamical renormalisation group calculation (Sect. 3.3). Lastly (Sect. 3.4) we study the 'low temperature' phase of the system which exhibits spatio-temporal chaos. This chaotic phase may be 'controlled' giving rise to a steady state configuration with broken chiral symmetry. Detailed calculations for Sections 3.3 and 3.4 are given in the Appendices IIIA and IIIB respectively. While reading this chapter, it would be useful to recall the results of the single particle study in Section 1.2.

3.1 Derivation of the Dynamical Equations

Consider a collection of particles each carrying a Heisenberg spin falling along one direction (say along \hat{x}) in the presence of a field which does not couple directly with the spins. Let us ask for the coarse-grained dynamics of the spin density, ignoring for the moment, the dynamics of the mass and momentum densities. We make use of symmetry arguments alone. In the absence of driving the dynamics conserves the total spin; $\partial_t \mathbf{S}$ is given by the divergence

of a current $\mathbf{J} = \Gamma \partial_x \vec{\mu} + \mathbf{j}_{iner}$, where $\vec{\mu} = \delta F[\mathbf{S}] / \delta \mathbf{S}$ is the chemical potential and \mathbf{j}_{iner} is the current coming from inertia ($F[\mathbf{S}]$ is the Landau-Ginzburg free-energy functional Eq. (1.3) and Γ the spin mobility). The external drive would clearly break the $x \leftrightarrow -x$ symmetry of the equations of motion, and so on general symmetry grounds one should include terms in the equations of motion containing an odd number of spatial derivatives. To lowest order, the dynamics of the spins with the driving alone maybe written as

$$\partial_t \mathbf{S} = v \partial_x \mathbf{S} + \lambda \mathbf{S} \times \partial_x \mathbf{S}. \quad (3.1)$$

The first term may be eliminated by a Galilean transformation $x \rightarrow x + vt$, $t \rightarrow t$, leaving only the second term to reflect the drive. Therefore in the presence of all the three effects — dissipation, inertia and driving — the time evolution is given by

$$\partial_t \mathbf{S} = -\Gamma \partial_x^2 \vec{\mu} - \partial_x \mathbf{j}_{iner} + \lambda \mathbf{S} \times \partial_x \mathbf{S} + \vec{\xi}(x, t), \quad (3.2)$$

where $\vec{\xi}$ is a conservative Gaussian noise with the correlator,

$$\langle \xi_\alpha(x, t) \xi_\beta(x', t') \rangle = -2k_B T \Gamma \partial_x^2 \delta_{\alpha\beta} \delta(x - x') \delta(t - t'). \quad (3.3)$$

The drive breaks the conservation of total spin, since it cannot be written as the divergence of a current. Therefore under renormalisation, the drive should give rise to other spin nonconserving terms of the form $(\mathbf{S} \cdot \mathbf{S})^n \mathbf{S}$ in addition to a *nonconservative noise*. We will see later that the coefficient of the $n = 0$ term is of $O(\lambda^2)$, the $n = 1$ term is of $O(\lambda^4)$ and the nonconservative noise variance of $O(\lambda^2)$. Since this nonconservative noise is generated by an external drive, its variance is not related to the dissipation via the Fluctuation-Dissipation Theorem (FDT) (see Sect. 1.1). These contributions clearly dominate over the conserved dissipation and noise at large length scales. The breakdown of FDT as a consequence of the external driving implies that the stationary probability distribution of the steady state configurations is not the equilibrium canonical distribution $P_{eq}(\{\mathbf{S}\}) \propto \exp(-F[\mathbf{S}]/k_B T)$, as can be seen by constructing the Fokker-Planck equation [1] for the probability distribution of spins $P(\{\mathbf{S}\}, t)$ corresponding to the Langevin equation Eq.(3.2),

$$\frac{\partial P}{\partial t} = \int dx (-\Gamma \partial_x^2) \frac{\delta}{\delta S_\mu} \left(\frac{\delta F}{\delta S_\mu} + \frac{\delta}{\delta S_\mu} \right) P - \int dx \frac{\delta}{\delta S_\mu} \left(\lambda \epsilon_{\mu\nu\rho} S_\nu S_\rho P \right). \quad (3.4)$$

We now generalise the above arguments to arbitrary $d \equiv d_{\perp} + 1$ dimensions, where the anisotropic driving is along one direction (\parallel) only. The resulting Langevin equation possesses spatial $O(d - 1)$ symmetry. Keeping all the relevant terms in the hydrodynamic limit, we obtain,

$$\frac{\partial \mathbf{S}}{\partial t} = \left(r_{\parallel} \partial_{\parallel}^2 + r_{\perp} \nabla_{\perp}^2 \right) \mathbf{S} - v \mathbf{S} - \frac{u}{6} (\mathbf{S} \cdot \mathbf{S}) \mathbf{S} - \lambda \mathbf{S} \times \partial_{\parallel} \mathbf{S} + g_{\parallel} \mathbf{S} \times \partial_{\parallel}^2 \mathbf{S} + g_{\perp} \mathbf{S} \times \nabla_{\perp}^2 \mathbf{S} + \tilde{\eta}. \quad (3.5)$$

We have displayed the usual spin precession term here in its anisotropic form explicitly. The nonconservative noise $\tilde{\eta}$ has mean zero and variance,

$$\langle \eta_{\alpha}(\mathbf{x}, t) \eta_{\beta}(\mathbf{x}', t') \rangle = 2B \delta_{\alpha\beta} \delta(\mathbf{x} - \mathbf{x}') \delta(t - t'). \quad (3.6)$$

Note that we have arrived at the final form of the continuum equations of motion using only symmetry arguments and conservation laws. The drive $\mathbf{S} \times \partial_x \mathbf{S}$ is a pseudo-vector; in the arguments just outlined there is no microscopic justification for including such a term. We therefore provide a microscopic model where the pseudo-vector drive arises from precession.

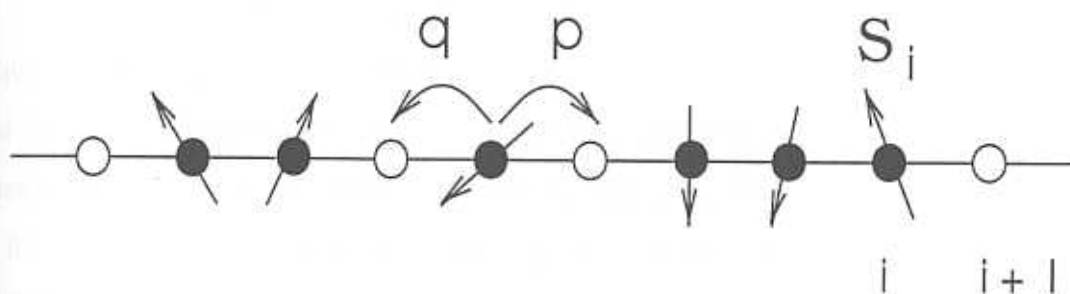


Figure 3.1: Hopping rules for the ASEP model with Heisenberg spins. Black spheres denote particles with an attached Heisenberg spin and white spheres denote vacancies.

We find that a slight extension of the discrete model introduced in Sect.1.2 gives rise to the above spin dynamics in the continuum limit. The extension consists of attaching a Heisenberg spin to each particle (Fig. 3.1), which interact with each other by the usual hard-core repulsion and nearest-neighbour exchange. The particle hopping probabilities p and q can in general depend on the spins of the particles, but for the time being let us restrict

our analysis to the simplest case when p and q are spin independent. In this limit, the zero temperature particle dynamics without dissipation is described by

$$\begin{aligned} \frac{\partial n_l(t)}{\partial t} &= \left[(1 - n_l)n_{l+1}q - n_l(1 - n_{l+1})p \right] - \left[n_l(1 - n_{l-1})q - n_{l-1}(1 - n_l)p \right] \\ &= j_{l+1/2} - j_{l-1/2}, \end{aligned} \quad (3.7)$$

where $n_l(t) = 0$ (vacant) or 1 (filled) denotes the occupancy of site l at time t . The corresponding spin dynamics in variables $\vec{\sigma}_l(t)$ (spin of particle at site l and time t) has contributions coming from hopping and spin precession (g is the Larmour frequency),

$$\begin{aligned} \frac{\partial \vec{\sigma}_l}{\partial t} &= g n_l \vec{\sigma}_l \times \vec{h}_l + \left[(1 - n_l)n_{l+1}\vec{\sigma}_{l+1}q - n_l(1 - n_{l+1})\vec{\sigma}_l p \right] \\ &\quad - \left[n_l(1 - n_{l-1})\vec{\sigma}_l q - n_{l-1}(1 - n_l)\vec{\sigma}_{l-1}p \right], \end{aligned} \quad (3.8)$$

where $\vec{h}_l = -J(n_{l+1}\vec{\sigma}_{l+1} + n_{l-1}\vec{\sigma}_{l-1})$ is the local molecular field. Now let us introduce coarse-grained variables $\rho_l = \langle n_l \rangle_h$ and $\mathbf{S}_l = \langle \vec{\sigma}_l \rangle_h$, where $\langle \cdot \rangle_h$ denotes average over histories till time t . We simplify the coarse-grained equations further by making a mean-field approximation [2] given by $\langle n_i n_j \rangle = \langle n_i \rangle \langle n_j \rangle$, $\langle \vec{\sigma}_i \vec{\sigma}_j \rangle = \langle \vec{\sigma}_i \rangle \langle \vec{\sigma}_j \rangle$ and $\langle n_i \vec{\sigma}_j \rangle = \langle n_i \rangle \langle \vec{\sigma}_j \rangle$. With this approximation, Eq.(3.7) takes the following form in the continuum limit :

$$\frac{\partial \rho}{\partial t} = \frac{p+q}{2} \frac{\partial^2 \rho}{\partial x^2} + (p-q) \left(\rho \frac{\partial \rho}{\partial x} - \frac{\partial \rho}{\partial x} \right). \quad (3.9)$$

This equation is known as the noiseless Burgers equation [2, 3] in one dimension. The external drive $p - q$ breaks the $x \leftrightarrow -x$ (reflection) symmetry in Eq.(3.9). Within the same mean-field approximation, the spin dynamics Eq.(3.8) simplifies considerably. Let us focus on the first term describing spin precession about the local magnetic field \vec{h}_l . Using the mean-field decoupling this may be written as

$$g \langle n_l \vec{\sigma}_l \times \vec{h}_l \rangle_h \rightarrow -gJ [\rho_l (\rho_{l+1} - \rho_{l-1})] \mathbf{S} \times \frac{\partial \mathbf{S}}{\partial x}. \quad (3.10)$$

This term has the form of the drive in Eq. (3.5) with a ‘coupling’ $-gJ\rho_l(\rho_{l+1} - \rho_{l-1})$. We evaluate this ‘coupling’ in the steady state of Eq. (3.7). Within the mean field approximation the steady state densities obey the recursion relation [2], $q\rho_{l+1} - p\rho_l + (p-q)\rho_l\rho_{l+1} = j_c$, where $j_{l+1/2} = j_{l-1/2} = j_c = \text{const}$. This implies

$$\rho_l(\rho_{l+1} - \rho_{l-1}) = p(\rho_l - \rho_{l-1}) - q(\rho_{l+1} - \rho_l). \quad (3.11)$$

The RHS of Eq. (3.11) can be written (to lowest order in ∂_x) as $\partial\rho/\partial x$ in the continuum limit. Since the external drive breaks the $x \leftrightarrow -x$ (reflection) symmetry in Eq.(3.9), $\partial\rho/\partial x$ would in general be non-zero. This implies that a term analogous to the drive in Eq. (3.5) would exist, if we can show that there exist steady state solutions for which $\partial\rho/\partial x$ is a constant or at best slowly varying in space. To see that this is indeed so, let us evaluate $\partial\rho/\partial x$ for particular steady state solutions, which are steady state solutions for respectable parameter ranges. Static solitons $\rho_s(x)$ are generic steady state solutions of Eq. (3.9), having the form [4]

$$\rho_s(x) = \rho_0 \tanh(k_s(x - x_0)), \quad (3.12)$$

where $\rho(x) \rightarrow \pm\rho_0$ as $x \rightarrow \pm\infty$. This static soliton is centered at x_0 and has a width $k_s^{-1} = (p + q)/(\rho_0(p - q))$. For a soliton with a large width (when $p \rightarrow q$ or $\rho_0 \ll 1$), the slope of the profile is almost a constant (and equal to $\rho_0 k_s$) in the bulk. This implies that in this regime, the drive term $\lambda \mathbf{S}(x, t) \times \partial_x \mathbf{S}(x, t)$ in Eq. (3.5) is reproduced in the continuum limit (to lowest order) with $\lambda = -gJ\rho_0^3(p - q)/(p + q)$.

Having provided a microscopic model for the coarse-grained dynamics Eq. (3.5), we will proceed to establish a ‘nonequilibrium phase diagram’ of steady states obtained by analysing the stationary solutions ($\partial_t \mathbf{S} = 0$) of Eq. (3.5). Let us specify the parameters in our ‘phase diagram’. Note that there are three different ‘temperature’ scales. For in the absence of any driving, the spin system has an equilibrium canonical temperature T . The parameters r_\perp and r_\parallel in the equations of motion Eq. (3.5) are functions of this temperature. Introduction of the drive brings in two other temperature scales : (i) the drive-induced dissipation v proportional to $T_{drive} - T_{drive}^c$ and (ii) the variance of the nonconserved noise $B \propto T_{noise}$. Since the FDT is violated by the external drive, these two temperature scales are not related to each other. Throughout this study we shall be in the paramagnetic phase of the equilibrium Heisenberg model $T > T_c$, or in other words $r_\perp, r_\parallel > 0$. Our phase diagram will therefore be parametrised by the two parameters v and B . Thus the ‘high drive-temperature’ phase corresponds to $T_{drive} > T_{drive}^c$ or $v > 0$, the critical phase corresponds to $T_{drive} = T_{drive}^c$ or $v = 0$ and the ‘low drive-temperature’ phase to $T_{drive} < T_{drive}^c$ or $v < 0$.

3.2 Dynamics at High Drive-Temperatures, $v > 0$

At high drive-temperatures the steady state, obtained by setting $\partial_t \mathbf{S} = 0$ is paramagnetic, characterised by $\langle \mathbf{S}(\mathbf{x}, t) \rangle = 0$ ($\langle \cdot \cdot \rangle$ denotes an average over the noise $\vec{\eta}$) and correlators. The effect of the drive is to change the correlation lengths $\xi_{\perp} = \sqrt{r_{\perp}/v} + O(\lambda^2/\sqrt{v}) - O(\lambda^2)$ and $\xi_{\parallel} = \sqrt{r_{\parallel}/v} + O(\lambda^2/\sqrt{v}) - O(\lambda^2)$. We find that this paramagnetic state is stable under dynamical perturbations. This can be seen by writing $\mathbf{S}(\mathbf{x}, t) = \langle \mathbf{S}(\mathbf{x}, t) \rangle + \mathbf{u}(\mathbf{x}, t)$, where \mathbf{u} is an arbitrary small perturbation. The time evolution of $\mathbf{u}(\mathbf{x}, t)$ to linear order is given by

$$\frac{\partial \mathbf{u}}{\partial t} = (r_{\perp} \nabla_{\perp}^2 + r_{\parallel} \partial_{\parallel}^2 - v) \mathbf{u} + \vec{\eta}, \quad (3.13)$$

which on Fourier transformation reads

$$\mathbf{u}_{\mathbf{k}}(t) = \mathbf{u}_{\mathbf{k}}(0) \exp(-\gamma_{\mathbf{k}} t) + \int_0^t dt' \vec{\eta}_{\mathbf{k}}(t') \exp(-\gamma_{\mathbf{k}}(t - t')), \quad (3.14)$$

where

$$\gamma_{\mathbf{k}} = -r_{\perp} k_{\perp}^2 - r_{\parallel} k_{\parallel}^2 - v. \quad (3.15)$$

This arbitrary perturbation $\mathbf{u}_{\mathbf{k}}$ always decays to zero when $v > 0$. The ‘paramagnetic phase’ is therefore linearly stable.

3.3 Dynamics in the Critical Phase, $v = 0$

In the critical region $v = 0$ ($T_{\text{drive}} = T_{\text{drive}}^c$), the linear theory is massless, resulting in divergent long wavelength fluctuations. This can be seen by calculating the correlation function $C(x, t) = \langle \mathbf{S}(\mathbf{x} + \mathbf{x}', t + t') \cdot \mathbf{S}(\mathbf{x}', t') \rangle$ from Eq. (3.5) by setting $u = \lambda = 0$. The correlation function has the scaling form

$$C(x, t) = \frac{B}{r_{\parallel}} x_{\parallel}^{2\chi} F_0 \left(\frac{r_{\parallel} t}{x_{\parallel}^z}, \frac{x_{\perp}}{x_{\parallel}^{\zeta}} \sqrt{\frac{r_{\parallel}}{r_{\perp}}} \right), \quad (3.16)$$

where the roughening exponent $\chi = 1 - d/2$, the growth exponent $z = 2$, the anisotropy exponent $\zeta = 1$, and F_0 is an analytic function of its arguments.

What is the nature of these divergent fluctuations in the presence of the nonlinear terms? This can be addressed by a perturbative calculation about the linear theory, treating the

couplings λ and u as small parameters (the other couplings g_{\parallel} and g_{\perp} will turn out to be *irrelevant* for $d > 2$). The perturbative corrections to the correlation function may be equivalently viewed as arising from modifications (renormalisations) of the parameters r_{\parallel} , r_{\perp} and B . The modified (renormalised) parameters (denoted by superscript R) may be calculated perturbatively in λ and u and have the generic form

$$r_{\parallel}^R = r_{\parallel} \left(1 + \sum_{i,j=1}^{\infty} a_{ij} (ux_{\parallel}^{\epsilon})^i (\lambda x_{\parallel}^{\epsilon})^j \right), \quad (3.17)$$

where x_{\parallel}^{ϵ} and x_{\perp}^{ϵ} denote the length dimension of the couplings u and λ respectively. Likewise the parameters r_{\perp}^R and B^R may be written in the form Eq. (3.17) with different expansion coefficients. If the theory is *renormalisable* then the series in Eq. (3.17) can be summed to be written in the form

$$r_{\parallel}^R = r_{\parallel} \left(1 + \alpha_1 (ux_{\parallel}^{\epsilon}) + \beta_1 (\lambda x_{\parallel}^{\epsilon}) \right)^{\delta}. \quad (3.18)$$

Similar expressions may be obtained for r_{\perp}^R and B^R with different sets of (α, β, δ) . This essentially implies that the theory, even in the presence of nonlinear couplings can be described by a *finite* number of parameters. Since renormalisability guarantees that the series Eq. (3.17) can be summed to a closed form (Eq. (3.18)), the correlation function $C(x, t)$ will retain a scaling form as in Eq. (3.16) with modified exponents z , ζ , χ and a new scaling function

$$C(x, t) = x_{\parallel}^{2\chi} F\left(\frac{t}{x_{\parallel}^z}, \frac{x_{\perp}}{x_{\parallel}^{\zeta}}\right). \quad (3.19)$$

This implies that the critical region (defined by $v^R = 0$) still has divergent long wavelength fluctuations.

In our model we assume renormalisability, which we justify *a posteriori* to lowest order in perturbation. We carry out a dynamical renormalisation group (RG) calculation to compute the new exponents and the scaling function using a field theoretic approach [5, 6, 7, 8]. This consists of the following steps —

(i) Naive Scaling : We scale space, time and the order parameter by an arbitrary length scale parameter $b < 1$ as, $x_{\parallel} = bx'_{\parallel}$, $\mathbf{x}_{\perp} = b^{\zeta} \mathbf{x}'_{\perp}$, $t = b^z t'$, and $\mathbf{S} = b^{\chi} \mathbf{S}'$, where the primed variables denote dimensionless quantities. We may reinterpret the effect of such a rescaling as

a change in the parameters; thus the form of Eq. (3.5) will remain unchanged if we change the parameters to their primed values $r'_{\parallel} = b^{z-2}r_{\parallel}$, $r'_{\perp} = b^{z-2\zeta}r_{\perp}$, $B' = b^{z-2\chi-\zeta(d-1)-1}B$, $u' = b^{4-d}u$, $\lambda' = b^{\chi+z-1}\lambda$, $g'_{\parallel} = b^{\chi+z-2}g_{\parallel}$, and $g'_{\perp} = b^{\chi+z-2}g_{\perp}$. In the absence of nonlinearities (when $u = \lambda = g_{\parallel} = g_{\perp} = 0$), the linear equation can be made scale invariant by choosing $\chi = 1 - d/2$, $z = 2$, $\zeta = 1$. With this choice of the exponents u and λ become dimensionless when $d_c^u = d_c^{\lambda} = 4$ (upper critical dimension), which implies that they will modify the scaling behaviour of the linear theory when $d < 4$ (u and λ are *relevant* for $d < 4$). The other two couplings g_{\parallel} and g_{\perp} have an upper critical dimension $d_c^g = 2$, therefore they are *irrelevant* for $d > 2$.

(ii) Perturbative Calculation : We calculate the corrections to the correlation functions from the nonlinearities, perturbatively in the couplings u and λ . On Fourier transforming Eq. (3.5) we obtain

$$\begin{aligned} S_{\alpha}(\mathbf{k}, \omega) = & G_0(\mathbf{k}, \omega) \eta_{\alpha} - \frac{i\lambda}{2} G_0(\mathbf{k}, \omega) \int \tilde{d}q \tilde{d}\nu [q_{\parallel} - (k_{\parallel} - q_{\parallel})] \epsilon_{\alpha\beta\delta} S_{\beta}(\mathbf{q}, \nu) S_{\delta}(\mathbf{k} - \mathbf{q}, \omega - \nu) \\ & - u F_{\alpha\beta\gamma\delta} G_0(\mathbf{k}, \omega) \int \tilde{d}q_1 \tilde{d}q_2 \tilde{d}\nu_1 \tilde{d}\nu_2 S_{\beta}(\mathbf{q}_1, \nu_1) S_{\gamma}(\mathbf{q}_2, \nu_2) S_{\delta}(\mathbf{k} - \mathbf{q}_1 - \mathbf{q}_2, \omega - \nu_1 - \nu_2), \end{aligned} \quad (3.20)$$

where the Fourier transform is defined as

$$\mathbf{S}(\mathbf{x}, t) = \int \tilde{d}k \tilde{d}\omega \mathbf{S}(\mathbf{k}, \omega) e^{i\omega t - i\mathbf{k} \cdot \mathbf{x}}, \quad (3.21)$$

with the measure $\tilde{d}(q, k) = d^d(q, k)/(2\pi)^d$, $\tilde{d}(\nu, \omega) = d(\nu, \omega)/2\pi$ and the range of integration $0 \leq |q|, |k| \leq \infty$, $-\infty \leq \nu, \omega \leq \infty$. The coefficient of the cubic term is given by $F_{\alpha\beta\gamma\delta} = (1/3)(\delta_{\alpha\beta}\delta_{\gamma\delta} + \delta_{\alpha\delta}\delta_{\beta\gamma} + \delta_{\alpha\gamma}\delta_{\beta\delta})$. The bare (unrenormalised) response function $G_0(\mathbf{k}, \omega)$ and the correlator $C_0(\mathbf{k}, \omega)$ are defined from the linear theory as

$$\begin{aligned} G_0(\mathbf{k}, \omega) = \langle \mathbf{S}(\mathbf{k}, \omega) \cdot \vec{\eta}(-\mathbf{k}, -\omega) \rangle &= \frac{1}{r_{\parallel} k_{\parallel}^2 + r_{\perp} k_{\perp}^2 - v - i\omega}, \\ C_0(\mathbf{k}, \omega) = \langle \mathbf{S}(\mathbf{k}, \omega) \cdot \mathbf{S}(-\mathbf{k}, -\omega) \rangle &= \frac{2B}{(r_{\parallel} k_{\parallel}^2 + r_{\perp} k_{\perp}^2 - v)^2 + \omega^2}. \end{aligned} \quad (3.22)$$

Note that we have explicitly retained v in the above expressions; at the end of the calculation, we shall however set $v^R = 0$ which characterises the critical phase. To carry out

the perturbative calculation effectively it is convenient to rewrite the recursion relation Eq. (3.20) in terms of the graphical representation (Feynman graphs) displayed in Fig. 3.2.

We now calculate the corrections to $G_0(\mathbf{k}, \omega)$ or the renormalised response function $G^R(\mathbf{k}, \omega)$ defined by

$$S_\alpha(\mathbf{k}, \omega) = G^R(\mathbf{k}, \omega) \eta_\alpha \quad (3.23)$$

order-by-order in perturbation theory. For this we need to use Eq. (3.20) together with the noise spectrum characterised by

$$\langle \eta_\alpha(\mathbf{k}_1, \omega_1) \eta_\beta(\mathbf{k}_2, \omega_2) \rangle = 2B\delta^d(\mathbf{k}_1 + \mathbf{k}_2)\delta(\omega_1 + \omega_2)\delta_{\alpha\beta}. \quad (3.24)$$

To $O(\lambda^2)$ and $O(u)$ (this corresponds to the lowest, 1-loop order) we obtain

$$\begin{aligned} G^R(\mathbf{k}, \omega) &= G_0(\mathbf{k}, \omega) - G_0(\mathbf{k}, \omega)^2 \left\{ \frac{\lambda^2}{4} \int d\mathbf{q} d\nu \left[(q_\parallel - (k_\parallel - q_\parallel))(k_\parallel - (-q_\parallel)) G_0(\mathbf{k} - \mathbf{q}, \omega - \nu) \right. \right. \\ &\quad \times C_0(\mathbf{q}, \nu) + ((k_\parallel - q_\parallel) - q_\parallel)(k_\parallel + (k_\parallel - q_\parallel)) G_0(\mathbf{q}, \nu) C_0(\mathbf{k} - \mathbf{q}, \omega - \nu) \Big] \\ &\quad \left. + \frac{5u}{3} \int d\mathbf{q} d\nu C_0(\mathbf{q}, \nu) \right\} \\ &= G_0(\mathbf{k}, \omega) + G_0(\mathbf{k}, \omega)^2 \Sigma(\mathbf{k}, \omega). \end{aligned} \quad (3.25)$$

The self energy $\Sigma(\mathbf{k}, \omega)$ contains all the corrections coming from the nonlinear terms. Since the critical dimensions of both u and λ is 4, the calculation of $\Sigma(\mathbf{k}, \omega)$ at the critical point ($v \rightarrow 0$) would involve integrals which are singular in the $k \rightarrow 0$ limit (infrared (IR) singularities) for $d < 4$. The integrals turn out to be logarithmically divergent (both in the $k \rightarrow 0$ (IR) and the $k \rightarrow \infty$ (UV) limit) as $d \rightarrow 4$ and the divergent pieces in both the limits turn out to be the same [6]. This allows us to use a procedure known as dimensional regularisation [8], to separate out the divergences as poles at $4 - d \equiv \epsilon = 0$. Details of the calculation are presented in Appendix IIIA.

The inverse of the renormalised response function $[G^R(\mathbf{k})]^{-1}$, can be used to define the renormalised parameters v^R , r_\parallel^R and r_\perp^R :

$$\begin{aligned} [G^R(\mathbf{k}, \omega)]^{-1} &= r_\parallel^R k_\parallel^2 + r_\perp^R k_\perp^2 - v^R - i\omega \\ &= G_0^{-1}(\mathbf{k}, \omega) - \Sigma(\mathbf{k}, \omega). \end{aligned} \quad (3.26)$$

$$v^R = v - \pi^3 \Lambda r_{\perp} \left(\frac{\tau}{8} + \frac{5\kappa}{6} \right), \quad (3.29)$$

where τ and κ are defined as

$$\tau = \frac{\lambda^2 B}{2\pi^3 (r_{\parallel} r_{\perp})^{3/2}}, \quad (3.30)$$

and

$$\kappa = \frac{u B}{2\pi^3 r_{\parallel}^{1/2} r_{\perp}^{3/2}}. \quad (3.31)$$

Note that we have used an upper momentum cutoff Λ to evaluate the renormalised v^R . The IR-divergences appear as poles at $\epsilon = 0$.

We now calculate the renormalised correlation function $C^R(\mathbf{k}, \omega) = \langle \mathbf{S}(\mathbf{k}, \omega) \cdot \mathbf{S}(-\mathbf{k}, -\omega) \rangle$ which to 1-loop satisfies the recursion relation

$$\begin{aligned} C^R(\mathbf{k}, \omega) &= C_0(\mathbf{k}, \omega) - \frac{\lambda^2}{4} \int d\mathbf{q} d\nu ((k_{\parallel} - q_{\parallel}) - q_{\parallel})(q_{\parallel} - (k_{\parallel} - q_{\parallel})) C_0(\mathbf{k} - \mathbf{q}, \omega - \nu) C_0(\mathbf{q}, \nu) \\ &\quad \times G_0(\mathbf{k}, \omega) G_0(-\mathbf{k}, -\omega) \\ &= 2G_0(\mathbf{k}, \omega) G_0(-\mathbf{k}, -\omega) B + G_0(\mathbf{k}, \omega) G_0(-\mathbf{k}, -\omega) \Sigma_B. \end{aligned} \quad (3.32)$$

The function Σ_B contains all the corrections coming from the nonlinear couplings and is calculated in Appendix IIIA. The renormalisation of the noise may now be easily determined via the definition $C^R(\mathbf{k}, \omega) = 2B^R G^R(\mathbf{k}, \omega) G^R(-\mathbf{k}, -\omega)$,

$$B^R = B \left(1 + \frac{\pi \tau v^{-\epsilon/2}}{32\epsilon} \right). \quad (3.33)$$

We have also computed the lowest order corrections to the nonlinear couplings (vertex corrections) defined as $-i\lambda^R = -i\lambda + 2\Gamma_{\lambda}$, and $-u^R = -u + \Gamma_u$, where the vertex functions Γ_{λ} and Γ_u have been computed in Appendix IIIA. To 1-loop we find

$$\lambda^R = \lambda \left(1 - \frac{3\pi \tau v^{-\epsilon/2}}{128\epsilon} \right), \quad (3.34)$$

and

$$u^R = u - (r_{\parallel}^{1/2} r_{\perp}^{3/2}) \left(\frac{11\pi^4 \kappa^2}{12B\epsilon} - \frac{27\pi^4 \tau^2}{8B\epsilon} \right). \quad (3.35)$$

(iii) Recursion Relations : By treating the scale parameter b as being infinitesimally small, we may recast the relation between the bare and the renormalised couplings as differential recursion relations. This makes the scale dependence of the couplings apparent. Let us define a scale of observation $b a_0 \sim v^{-1/2}$, where we have written a_0 as a microscopic lengthscale and b as a pure number. We first define a dimensionless coupling $\tilde{r}_{\parallel}^R(b) = r_{\parallel}^R(b a_0)^{z-2}$ which from Eq. (3.27) satisfies,

$$\tilde{r}_{\parallel}^R(b) = r_{\parallel}(b a_0)^{z-2} \left(1 + \frac{\pi \tau (b a_0)^{\epsilon}}{4\epsilon} \right). \quad (3.36)$$

Since b is infinitesimal, we may apply the rescaling operator $b\partial/\partial b$ on Eq. (3.36) to obtain,

$$b \frac{\partial \tilde{r}_{\parallel}^R}{\partial b} = r_{\parallel}(b a_0)^{z-2} \left(z - 2 + \frac{\pi \tau (b a_0)^{\epsilon}}{4} \right). \quad (3.37)$$

We again define a dimensionless parameter for τ by $\tilde{\tau}^R(b) = \tau^R(b a_0)^{\epsilon}$. Recalling that τ is of $O(\lambda^2)$ (Eq. (3.30)), we may to lowest order in τ replace r_{\parallel} and τ in Eq. (3.37) by their renormalised values. We thus arrive at a differential recursion relation to lowest order in perturbation,

$$\frac{\partial \tilde{r}_{\parallel}^R}{\partial l} = \tilde{r}_{\parallel}^R \left(z - 2 + \frac{\pi \tilde{\tau}^R}{4} \right), \quad (3.38)$$

where $l = \ln b$. Following same procedure we obtain differential recursion relations for other renormalised parameters :

$$\frac{\partial \tilde{r}_{\perp}^R}{\partial l} = \tilde{r}_{\perp}^R \left(z - 2\zeta + \frac{5\pi \tilde{\tau}^R}{48} \right), \quad (3.39)$$

$$\frac{\partial \tilde{B}^R}{\partial l} = \tilde{B}^R \left(z - 2\chi - \zeta(d-1) - 1 + \frac{\pi \tilde{\tau}^R}{32} \right), \quad (3.40)$$

$$\frac{\partial \tilde{\lambda}^R}{\partial l} = \tilde{\lambda}^R \left(\chi + z - 1 + \frac{3\pi \tilde{\tau}^R}{128} \right), \quad (3.41)$$

$$\frac{\partial \tilde{u}^R}{\partial l} = \tilde{u}^R \left(z + 2\chi - \frac{11\pi\zeta}{24} \tilde{\kappa}^R \right) + \frac{27\pi^4 \zeta (\tilde{r}_{\parallel}^R)^{1/2} (\tilde{r}_{\perp}^R)^{3/2}}{8\tilde{B}^R} (\tilde{\tau}^R)^2, \quad (3.42)$$

$$\frac{\partial \tilde{\tau}^R}{\partial l} = \tilde{v}^R \left((4-d)\zeta - \frac{35\pi\tilde{\tau}^R}{64} \right), \quad (3.43)$$

$$\frac{\partial \tilde{\kappa}^R}{\partial l} = \tilde{\kappa}^R \left(\zeta\epsilon - \frac{11\pi\zeta\tilde{\kappa}^R}{24} - \frac{\pi\tilde{v}^R}{2} \right) + \frac{27\pi\zeta(\tilde{\tau}^R)^2}{16}. \quad (3.44)$$

(iv) Fixed Points and RG flows : In the critical phase the system is scale invariant at length scales much larger than the cutoff. This implies that the critical phase is given by the *fixed points* of the recursion equations derived above,

$$\frac{\partial \tilde{\tau}^*}{\partial l} = \frac{\partial \tilde{\kappa}^*}{\partial l} = \frac{\partial \tilde{r}_{\parallel}^*}{\partial l} = \frac{\partial \tilde{r}_{\perp}^*}{\partial l} = \frac{\partial \tilde{\lambda}^*}{\partial l} = \frac{\partial \tilde{B}^*}{\partial l} = 0. \quad (3.45)$$

The above equations yield four fixed points :

- (A) $\tilde{\tau}^* = \tilde{\kappa}^* = 0$. This ‘Gaussian fixed point’ is stable for $d > 4$ and unstable for $d < 4$. The exponents take their ‘mean field’ values $z = 2$, $\zeta = 1$, and $\chi = 1 - d/2$ at this fixed point.
- (B) $\tilde{\tau}^* = 0$, $\tilde{\kappa}^* = 24\epsilon/(n+8)\pi$. This fixed point is unstable for both $d > 4$ and $d < 4$.
- (C) $\tilde{\tau}^* = 64\epsilon/35\pi$, $\tilde{\kappa}^* = 24\epsilon[3 + \sqrt{3 + 1112(n+8)}]/\{35(n+8)\pi\}$. This fixed point is again unstable for both $d > 4$ and $d < 4$.
- (D) $\tilde{\tau}^* = 64\epsilon/(35\pi)$, $\tilde{\kappa}^* = 24\epsilon[3 - \sqrt{3 + 1112(n+8)}]/\{35(n+8)\pi\}$. This ‘driven fixed point’ is unstable for $d > 4$ but stable for $d < 4$. Exponents take nontrivial values to $O(\epsilon)$, $z = 2 - 16\epsilon/35$, $\zeta = 1 - 2\epsilon/15$ (anisotropic), and $\chi = 1 - d/2$. Note that χ does not change from its mean field value to this order.

We exhibit the fixed points and the RG flow diagram to $O(\epsilon)$ in Fig. 3.3 .

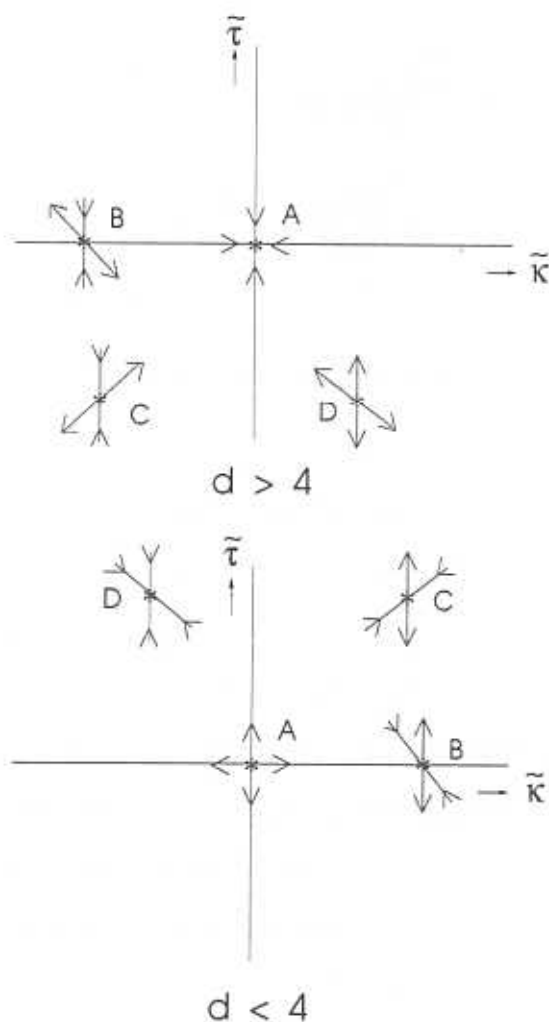


Figure 3.3: Plot show fixed points and RG flows. For $d > 4$, A (Gaussian fixed point) is the only stable fixed point, while for $d < 4$ there is a nontrivial stable driven fixed point D.

We would like to stress that these nontrivial critical fluctuations as a result of the external drive exist *even when the equilibrium Heisenberg magnet is in its high temperature paramagnetic phase*.

3.4 Dynamics at Low Drive-Temperatures, $v < 0$

We now investigate the effects of driving when $v < 0$ (low-drive-temperature). Our results hold when the equilibrium phase of the Heisenberg spins (without driving) is either paramagnetic ($T > T_c$) or ferromagnetic ($T < T_c$). In the presence of driving we ask for the stable

steady states that the spin system gets into. It is convenient to work with dimensionless variables

$$\begin{aligned} x_{\parallel} &\rightarrow x_{\parallel} \sqrt{\frac{r_{\parallel}}{v}}, \quad x_{\perp} \rightarrow x_{\perp} \sqrt{\frac{r_{\perp}}{v}}, \quad t \rightarrow tv, \quad \mathbf{S} \rightarrow \mathbf{S} \sqrt{\frac{6v}{u}}, \quad \vec{\eta} \rightarrow \vec{\eta} v \sqrt{\frac{6v}{u}}, \quad \lambda \rightarrow \lambda \sqrt{\frac{6v}{r_{\parallel}}}, \\ g_{\parallel} &\rightarrow g_{\parallel} \sqrt{\frac{6v}{ur_{\parallel}^2}}, \quad g_{\perp} \rightarrow g_{\perp} \sqrt{\frac{6v}{ur_{\perp}^2}}, \quad B \rightarrow B \frac{uv^{d/2-4}}{6r_{\parallel}^{1/2} r_{\perp}^{d/2-1}}, \end{aligned}$$

which simplify the equations of motion to

$$\frac{\partial \mathbf{S}}{\partial t} = \left(\partial_{\parallel}^2 + \nabla_{\perp}^2 \right) \mathbf{S} + \mathbf{S} - (\mathbf{S} \cdot \mathbf{S}) \mathbf{S} - \lambda \mathbf{S} \times \partial_{\parallel} \mathbf{S} + g_{\parallel} \mathbf{S} \times \partial_{\parallel}^2 \mathbf{S} + g_{\perp} \mathbf{S} \times \nabla_{\perp}^2 \mathbf{S} + \vec{\eta} \quad (3.46)$$

with nonconservative noise variance satisfying Eq. (3.6). For our subsequent analysis we shall fix $T > T_C$ or $r > 0$ where the equilibrium phase with no driving is paramagnetic.

We set $T_{\text{noise}} = 0$ (i.e. $B = 0$), the noiseless Eq. (3.46) can now be analysed for steady states. We first investigate the *homogeneous* steady states :

(i) 'Paramagnetic steady state' represented by $\langle S_{\alpha} \rangle = 0$ (average is taken over the steady state configurations) is a solution of the stationary equations. It is easy to see from Eq. (3.13) that this steady state is linearly unstable.

(ii) 'Ferromagnetic steady state' with broken $O(3)$ symmetry represented by $\langle S_1 \rangle = \langle S_2 \rangle = 0$ and $\langle S_3 \rangle = 1$ is also a solution of the stationary equations. This turns out to be linearly unstable too, as can be seen by perturbing about this state by a small fluctuation $u(\mathbf{x}, t)$ (to avoid a clutter of terms we set $g_{\perp} = g_{\parallel} = 0$ with no loss of generality),

$$\begin{aligned} \partial_t u_1(\mathbf{x}, t) &= \nabla^2 u_1(\mathbf{x}, t) + \lambda \partial_{\parallel} u_2(\mathbf{x}, t), \\ \partial_t u_2(\mathbf{x}, t) &= \nabla^2 u_2(\mathbf{x}, t) - \lambda \partial_{\parallel} u_1(\mathbf{x}, t), \\ \partial_t u_3(\mathbf{x}, t) &= \nabla^2 u_3(\mathbf{x}, t) - 2u_3(\mathbf{x}, t). \end{aligned} \quad (3.47)$$

Using the combination $u^+ = u_1 + iu_2$, $u^- = u_1 - iu_2$ and u_3 the above equations simplify in Fourier space,

$$\begin{aligned} \partial_t u_{\mathbf{k}}^+(t) &= -k^2 u_{\mathbf{k}}^+(t) + \lambda k_{\parallel} u_{\mathbf{k}}^+(t), \\ \partial_t u_{\mathbf{k}}^-(t) &= -k^2 u_{\mathbf{k}}^-(t) - \lambda k_{\parallel} u_{\mathbf{k}}^-(t), \\ \partial_t u_{3\mathbf{k}}(t) &= -k^2 u_{3\mathbf{k}}(t) - 2u_{3\mathbf{k}}(t), \end{aligned} \quad (3.48)$$

clearly showing that $u_{\mathbf{k}}^{\pm}(t) = u_{\mathbf{k}}^{\pm}(0) \exp(-k^2 \pm \lambda k_{\parallel} t)$ are unstable at large wavelengths when $k_{\parallel} < \lambda$.

Next, we study the *inhomogeneous* steady states :

(iii) 'Helical steady state' with broken chiral symmetry is represented more conveniently in the variables ρ , ϕ and S_3 , which are related to S_1 , S_2 and S_3 by the transformation $S_1 = \rho \cos \phi$, $S_2 = \rho \sin \phi$ and $S_3 = S_3$. The noiseless equations of motion (setting $g_{\parallel} = g_{\perp} = 0$) in these variables are

$$\begin{aligned} \frac{\partial \rho}{\partial t} &= \nabla^2 \rho - \rho(\nabla \phi)^2 + \rho - (\rho^2 + S_3^2)\rho - \lambda \rho S_3 \partial_{\parallel} \phi + \eta_{\rho}, \\ \frac{\partial \phi}{\partial t} &= \nabla^2 \phi + \frac{2}{\rho}(\nabla \rho) \cdot (\nabla \phi) + \frac{\lambda}{\rho}(S_3 \partial_{\parallel} \rho - \rho \partial_{\parallel} S_3) + \eta_{\phi}, \\ \frac{\partial S_3}{\partial t} &= \nabla^2 S_3 + S_3 - (\rho^2 + S_3^2)S_3 + \lambda \rho^2 \partial_{\parallel} \phi + \eta_3. \end{aligned} \quad (3.49)$$

The components of the noise are related to the cartesian components by $\eta_{\rho} = \eta_1 \cos \phi + \eta_2 \sin \phi$, $\eta_{\phi} = \rho^{-1}(\eta_2 \cos \phi - \eta_1 \sin \phi)$. A helical configuration is represented by $\rho = a$, $\phi = px_{\parallel} + c$ and $S_3 = b$, where a, b and p are arbitrary constants. Such a helix is a solution of the stationary equations if the projection of the local spins along the \parallel axis b and the pitch $1/p$ satisfy the following relations

$$b = \pm \left[\frac{1}{2} \left\{ 1 - a^2(1 + \lambda^2) \pm \sqrt{(a^2(\lambda^2 + 1) - 1)^2 - 4a^4} \right\} \right]^{1/2}, \quad (3.50)$$

and

$$p = \frac{1}{2} \left\{ -\lambda b \pm \sqrt{\lambda^2 b^2 - 4(R^2 - 1)} \right\}, \quad (3.51)$$

where $R = \sqrt{a^2 + b^2}$ is the magnitude of each spin. The only free parameter a is however bounded by $a < (3 + \lambda^2)^{-1/2}$, coming from the requirement that b be real.

Unfortunately even this steady state is linearly unstable as we show explicitly. Consider small fluctuations about the helical steady state, $\rho = a + \delta\rho$, $\phi = px_{\parallel} + c + \delta\phi$ and $S_3 = b + u$. To linear order the Fourier components of the fluctuations evolve as (for simplicity we exhibit

the modes with $k_{\perp} = 0$)

$$\frac{\partial}{\partial t} \begin{pmatrix} \delta \rho_{\mathbf{k}} \\ \delta \phi_{\mathbf{k}} \\ u_{\mathbf{k}} \end{pmatrix} = \underbrace{\begin{pmatrix} -k_{\parallel}^2 - 2a^2 & -ik_{\parallel}a(2p + \lambda b) & -a(2b + \lambda p) \\ ik_{\parallel}(2p + \lambda b)/a & -k_{\parallel}^2 & -ik_{\parallel}\lambda \\ -2a(b - \lambda p) & i\lambda k_{\parallel}a^2 & -k_{\parallel}^2 + (1 - a^2 - 3b^2) \end{pmatrix}}_D \begin{pmatrix} \delta \rho_{\mathbf{k}} \\ \delta \phi_{\mathbf{k}} \\ u_{\mathbf{k}} \end{pmatrix}. \quad (3.52)$$

The signature of instability is that the real part of any one of the eigenvalues of the matrix D be positive. Fig. (3.4) shows 2-dimensional plots of the real part of the eigenvalues versus a and k_{\parallel} for a particular value of λ . This shows that at least one eigenvalue has a positive real part for a continuous band of k_{\parallel} . We have checked that this result holds for other values of λ . This implies that there is an infinity of unstable spatially periodic steady states parametrised by a (and for each value of a there are two values of b and p), a fact that will be of some significance later.

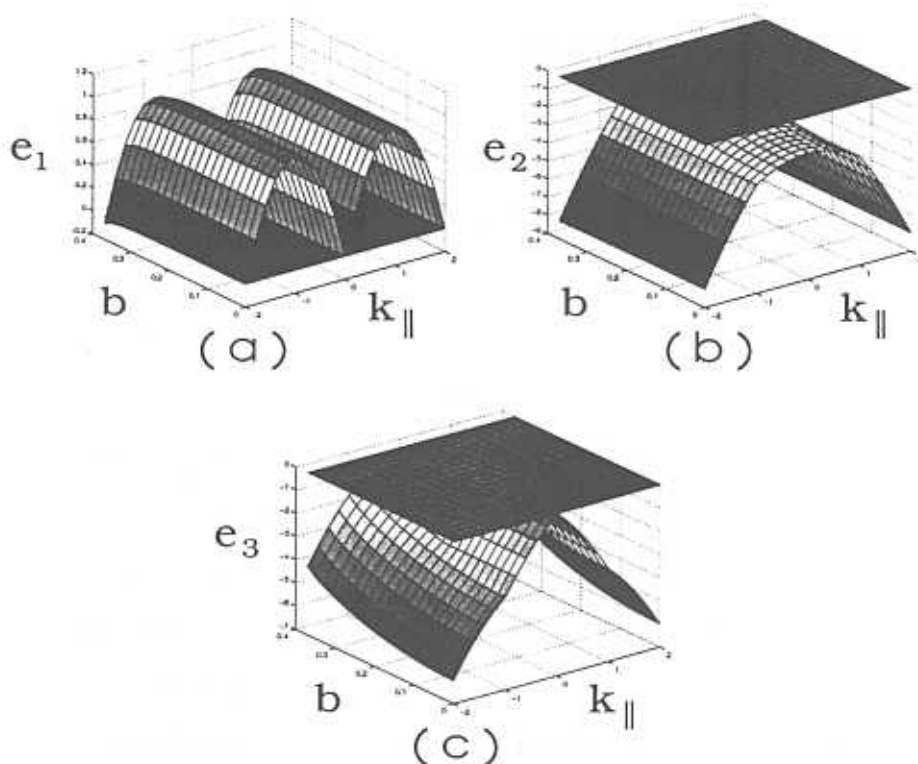


Figure 3.4: Plot of the real part of the eigenvalues e_1 , e_2 and e_3 versus a and k_{\parallel} for $\lambda = 2$. The eigenvalue e_1 is positive for all values of a and k_{\parallel} indicating linear instability.

The inhomogeneous helical steady state was suggested by the chiral nature of the driving. It would be impossible to do an exhaustive check of all inhomogeneous configurations for possible steady states. Our strategy is therefore to solve the noiseless equations of motion numerically starting from arbitrary initial configurations. The dynamics could either take the system to some other non-trivial inhomogeneous stationary state or lead to temporally periodic or chaotic configurations [9].

To determine the asymptotic configurations starting from generic initial conditions we solve the noiseless Eq. (3.46) numerically in $d = 1$. This equation should be handled carefully as the linear derivative in the drive would give rise to numerical instabilities if the standard Euler scheme of discretisation were implemented [10]. We adopt an operator splitting method [10] which allows us to treat the dissipative terms and the drive separately under different discretisation schemes. The dissipative part is solved using the standard Euler method (Sect. 2.1.1) and for the drive we use the following algorithm. The time evolution of the spins with the drive alone is a precession about the local magnetic field $\mathbf{h}(\mathbf{x}, t) = \partial_{\parallel} \mathbf{S}(\mathbf{x}, t)$. If $\mathbf{h}(\mathbf{x}, t)$ were a constant in space and time, the local spin $\mathbf{S}(\mathbf{x}, t)$ would have precessed about this field, keeping its magnitude $|\mathbf{S}|$ fixed but changing its azimuthal angle ϕ (taking the direction of \mathbf{h} as the z -axis) by $|\mathbf{h}(\mathbf{x}, t)|\Delta t$ in a time interval of Δt . This would have been exact if the field \mathbf{h} were a constant; in our case however $\mathbf{h}(\mathbf{x}, t)$ depends on space and time and we introduce errors of $O(\Delta t)$. We choose Δt small enough so as to reduce this error. The advantage of this method is that it does not give rise to numerical instabilities and automatically preserves the magnitude of the local spin $|\mathbf{S}|$ in time. In the simulation space and time are discretised with $\Delta x = 1$ and $\Delta t = 0.0001$ on a system of size $N = 200$ (large enough to avoid finite size effects) with periodic boundary conditions. The local field is calculated by the rule $\mathbf{h}_i = (\mathbf{S}_{i+1} - \mathbf{S}_{i-1})/\Delta x$. This field is used to update the local spin by the precession algorithm.

Using this numerical scheme we can compute the time series of observables like the magnetisation and energy density $E = \langle \int dx (\nabla \mathbf{S})^2 \rangle$ ($\langle \cdots \rangle$ denotes an average over initial configurations). We first note that these quantities never seem to settle to a stationary

value, strongly suggesting that no stable steady state exists. The motion could therefore be either temporally periodic or chaotic. This should be revealed in a power spectrum analysis; periodic motion would appear as delta function peaks. In Fig. (3.5) we display the power spectrum $P(\omega) = |M_3(\omega)|^2$ of the third component of the total magnetisation $M_3 = \langle S_3 \rangle$ for data collected over more than 3 decades. The data shows some small features which are in fact spurious since they can be erased by more averaging and more sophisticated binning. We also find that the power spectrum follows a power law ($1/\omega^2$) behaviour over roughly 3 decades. The power spectrum of the total energy density also shows a similar behaviour. This strongly suggests that the dynamics is temporally chaotic [11]. We have also checked that this chaotic behaviour persists when Eq. (3.46) is solved numerically starting from a variety of initial configurations.

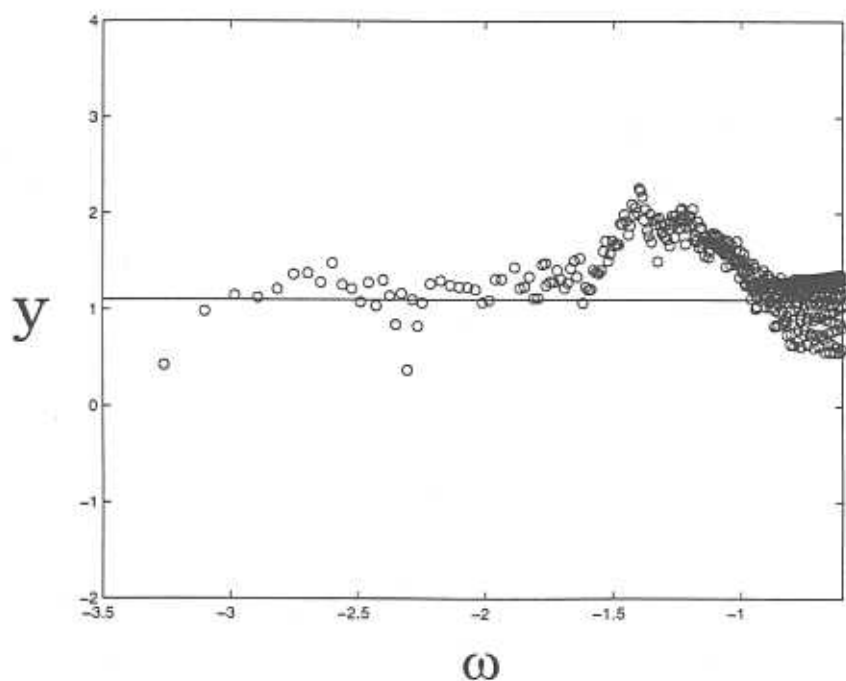


Figure 3.5: Plot of $y = \sqrt{\omega^2 P(\omega)}$ showing a $1/\omega^2$ dependence of the power spectrum over approximately 3 decades.

Since the components of spin obey partial differential equations (PDEs), we also check for spatial chaos. This is best visualised by constructing space-time plots of local quantities. For instance, Fig. (3.6) is a space-time plot of the signed local pitch, $\text{sgn}(p) \equiv \text{sgn}(\partial_x \phi)$,

strongly suggesting spatio-temporal chaos[11].

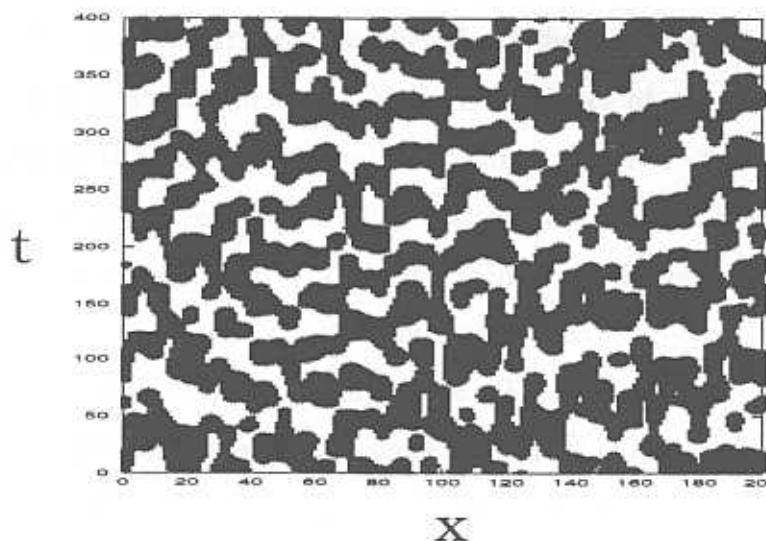


Figure 3.6: Space-time plot of the signed local pitch, $\text{sgn}(p) \equiv \text{sgn}(\partial_x \phi)$ (black and white patches denote $\text{sgn}(p) = \pm 1$ respectively), suggesting spatio-temporal chaos.

We hope we have provided convincing evidence that the asymptotic configurations in the low drive-temperature regime exhibit spatio-temporal chaos. The numerical evidence we presented was for $d = 1$, and though we cannot be sure whether this spatio-temporal chaos will persist at higher spatial dimensions, we feel that this is quite likely. This is because in our stability analysis of steady states done for arbitrary spatial dimension, we failed to find any reasonable stable steady state configuration at low drive-temperatures. Moreover, a Lyapunov stability analysis of the simpler equation $\partial_t \mathbf{S} = \lambda \mathbf{S} \times \partial_{||} \mathbf{S}$ in arbitrary d reveals that a tiny disturbance in the initial conditions grows exponentially in time. Several questions arise, to which we do not have answers at present, such as whether there exists a low-dimensional chaotic attractor and if so what is its nature and dimensionality.

The spatio-temporal chaotic phase that we just discovered has embedded in it an infinity of unstable (spatially) periodic steady states. This, together with the fact that the dynamics is ergodic, are two of the characteristic properties of chaotic systems [12, 13]. These properties would imply that starting from generic initial conditions the configuration of spins would eventually visit these periodic steady states. However starting from generic initial conditions the time taken to visit any one of these periodic steady states is unpredictable. Since

these periodic steady states are unstable, once visited, the dynamics will veer the spin configurations away from it.

We now ask whether we can arrange that the spin configuration stays put in a prescribed periodic steady state having visited it? This is the subject of *control of spatio-temporal chaotic systems*, one of the most important problems in modern chaos research [12, 13]. There are two aspects to the control of chaos, *stabilisation* and *targeting*. Holding the periodic steady state having visited it, is termed stabilisation. However since the time taken for this visit from an arbitrary initial condition can be extremely large, it is desirable to *target* a prescribed unstable periodic steady state. There have been many proposals for controlling chaos in finite dimensional dynamical systems [12, 13]. However there has been very little work in the more important area of control of spatio-temporal chaos in PDEs (which correspond to an infinite dimensional dynamical system, see Ref. [13] for a review). We will show that for our dynamical model spatio-temporal chaos can be both stabilised and targeted, and hence controlled.

We have seen that the spatially periodic unstable steady states (helical steady states) are parametrised by a , the projection of the spin along the \perp axis, p , the inverse pitch, and b , the projection of the spin along the \parallel axis. Our stability analysis (Sect. 3.4) indicated that the dominant instabilities occurred along the direction of the drive. We therefore focus on controlling the spin component S_3 .

We attempt to control the spatio-temporal chaos in order to obtain a prescribed helical configuration with fixed values of a , b and p . Since the dynamics is ergodic it will eventually visit this configuration. We subsequently apply small perturbations to prevent S_3 from deviating from this value of b . This prescription *stabilizes* the prescribed helical configuration, Fig. (3.7).



Figure 3.7: Picture of the stabilised helical configuration from numerical simulations.

In order to *target* this prescribed helix we add a uniaxial spin anisotropic potential $V_3 = r_3(S_3^2 - b^2)^2$ (or even $V_3 = -r_3 S_3^4$) to the free-energy functional with a large positive value of r_3 . We have found that for sufficiently large r_3 , this uniaxial potential forces S_3 to take the value b exponentially fast starting from arbitrary initial configurations. The subsequent dynamics maintains $S_3 = b = \text{constant}$; the noiseless Eq. (3.46) reduces (in d -dimensions) to

$$\begin{aligned}\frac{\partial \rho}{\partial t} &= \nabla^2 \rho - \rho(\nabla \phi)^2 + \rho - (\rho^2 + b^2)\rho - \lambda b \rho \partial_{\parallel} \phi, \\ \frac{\partial \phi}{\partial t} &= \nabla^2 \phi + \frac{2}{\rho}(\nabla \rho) \cdot (\nabla \phi) + \frac{\lambda b}{\rho}(\partial_{\parallel} \rho),\end{aligned}\quad (3.53)$$

We now note that these dynamical equations can be recast as a conventional purely dissipative Langevin equation at zero temperature,

$$\begin{aligned}\frac{\partial \rho}{\partial t} &= -\frac{\delta F}{\delta \rho}, \\ \frac{\partial \phi}{\partial t} &= -\frac{1}{\rho^2} \frac{\delta F}{\delta \phi},\end{aligned}\quad (3.54)$$

where the ‘free-energy functional’ F has the form of a *chiral XY model* [14],

$$F = \frac{1}{2} \int d^d x \left[(\nabla \rho)^2 + \rho^2 (\nabla \phi)^2 - (\rho^2 + b^2) + \frac{1}{2}(\rho^2 + b^2)^2 + \lambda b \rho^2 \partial_{\parallel} \phi \right], \quad (3.55)$$

It is easy to see that F is a Lyapunov functional [1],

$$\frac{dF}{dt} = \int d^d x \left(\frac{\delta F}{\delta S_1} \frac{\partial S_1}{\partial t} + \frac{\delta F}{\delta S_2} \frac{\partial S_2}{\partial t} \right) = \int d^d x \left[-\left(\frac{\delta F}{\delta S_1} \right)^2 - \left(\frac{\delta F}{\delta S_2} \right)^2 \right] < 0, \quad (3.56)$$

which decreases monotonically in time. Hence starting from any initial configuration the system heads towards the minimum of this F , which is a unique helix with parameters b , a and p (p is related to a and b via Eq. (3.51)). That there is a unique minimum can be seen by determining the ‘free-energy’ F_h of the helical configurations from Eq. (3.55) and plotting $F_h[p, a]$ against p and a (Fig. 3.8).

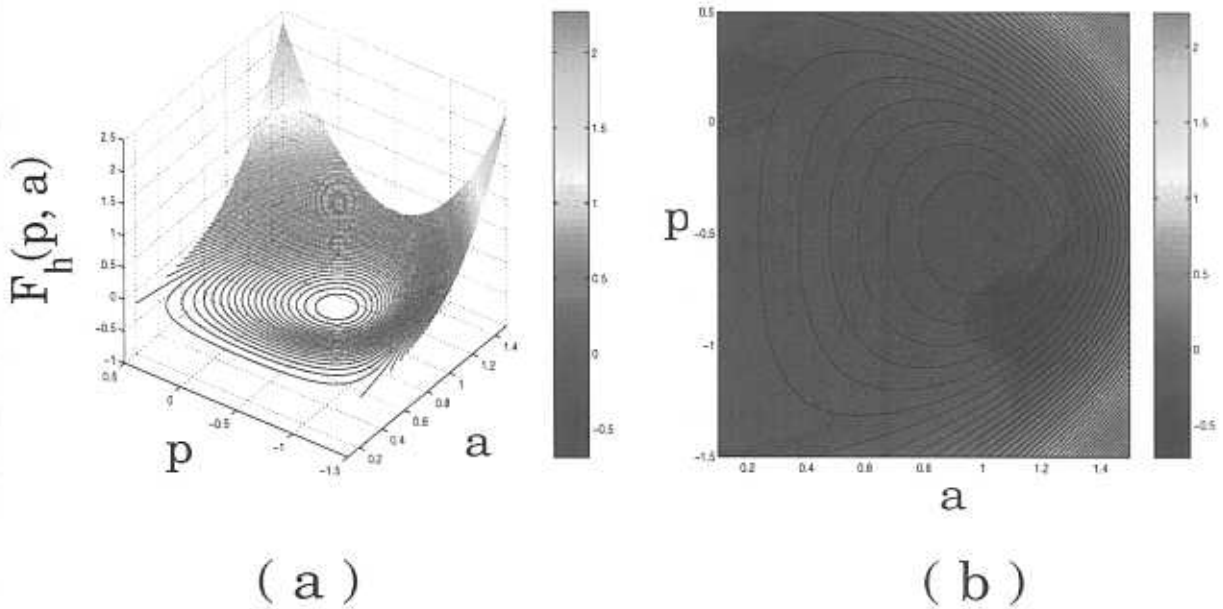


Figure 3.8: (a) Contour plot of the ‘free-energy’ F_h as a function of a and p . (b) Projection of plot (a) on the pa -plane. It is clear from the plots that there is a unique helical minimum.

The stability of this ‘free-energy’ minimising helix can also be tested directly from Eq.(3.53). As before, we perturb about this helix : $\rho = a + \tilde{\rho}(\mathbf{x}, t)$, and $\phi = px_{\parallel} + c + \tilde{\phi}(\mathbf{x}, t)$, and deduce the growth of these perturbations to linear order,

$$\begin{aligned}
 \frac{\partial \tilde{\rho}}{\partial t} &= \nabla^2 \tilde{\rho} - 2a^2 \tilde{\rho} - a(2p + \lambda b) \partial_{\parallel} \tilde{\phi}, \\
 \frac{\partial \tilde{\phi}}{\partial t} &= \nabla^2 \tilde{\phi} + \frac{1}{a}(2p + \lambda b) \partial_{\parallel} \tilde{\rho}.
 \end{aligned}
 \tag{3.57}$$

By going to Fourier space we may evaluate the eigenvalues $\omega_1(\mathbf{k})$ and $\omega_2(\mathbf{k})$ of the dynamical matrix, given by

$$\omega_{1,2}(\mathbf{k}) = -(k_{\parallel}^2 + k_{\perp}^2 + a^2) \pm \left\{ a^2 + k_{\parallel}^2 (2p + \lambda b)^2 \right\}^{1/2}.
 \tag{3.58}$$

The helix configuration would be stable if these two eigenvalues have positive real parts for all \mathbf{k} . This can be seen numerically by substituting the values a and p take at the 'free-energy' minimum in the above expression.

This completes our discussion of the control of spatio-temporal chaos. However no discussion would be complete without considering the effects of noise which might result in occasional escapes from the otherwise well controlled system. Do these escapes lead to an instability of the targeted configuration? We therefore ask what happens to this controlled helical configuration when we turn on the nonconserved noise $\vec{\eta}$, i.e. when $T_{noise} \neq 0$. We answer this by again considering small fluctuations $\tilde{\rho}(\mathbf{x}, t)$ and $\tilde{\phi}(\mathbf{x}, t)$ about the controlled helical state.

The linearised equations of motion Eq. (3.57) in $\tilde{\rho}$ and $\tilde{\phi}$ now contain the nonconservative noises η_ρ and η_ϕ with mean zero and correlators $\langle \eta_{\rho\mathbf{k}}(t) \eta_{\rho\mathbf{k}'}(t') \rangle = B \delta_{\mathbf{k}, -\mathbf{k}'} \delta(t - t')$, $\langle \eta_{\phi\mathbf{k}}(t) \eta_{\phi\mathbf{k}'}(t') \rangle = B \delta_{\mathbf{k}, -\mathbf{k}'} \delta(t - t')$ and $\langle \eta_{\rho\mathbf{k}}(t) \eta_{\phi\mathbf{k}'}(t') \rangle = 0$, to linear order. The linearised equations are stochastic differential equations with Gaussian white noise and so we need to modify our definition of dynamical stability. We shall say that the controlled helical state is stable if the means $\langle \tilde{\rho} \rangle$ and $\langle \tilde{\phi} \rangle$ vanish and the variances are finite in the thermodynamic limit.

The equations for $\langle \tilde{\rho} \rangle$ and $\langle \tilde{\phi} \rangle$ are identical to Eq. (3.57) and therefore the means decay to zero exponentially fast. To obtain the variance we calculate the equal-time correlation functions $C_{\tilde{\rho}}(\mathbf{k}, t) = \langle \tilde{\rho}_{\mathbf{k}}(t) \tilde{\rho}_{-\mathbf{k}}(t) \rangle$ and $C_{\tilde{\phi}}(\mathbf{k}, t) = \langle \tilde{\phi}_{\mathbf{k}}(t) \tilde{\phi}_{-\mathbf{k}}(t) \rangle$ and integrate over all \mathbf{k} between $2\pi/L$ and Λ , where L is the size of the system and Λ is the ultraviolet cutoff. Since we are interested in the L dependence of the variance, we will replace the correlation functions in the entire k range by their behaviour at small k . The calculation in Appendix IIIB shows that for small k

$$\begin{aligned} C_{\tilde{\rho}}(\mathbf{k}, t) &\sim \frac{B}{k^2 + a^2}, \\ C_{\tilde{\phi}}(\mathbf{k}, t) &\sim \frac{B}{k_{\perp}^2 + k_{\parallel}^2 \left(1 - \left(\frac{2p + \lambda b}{a} \right)^2 \right)}. \end{aligned} \quad (3.59)$$

The variances $\Delta_{\tilde{\rho}}$ and $\Delta_{\tilde{\phi}}$ obtained on integrating the correlators over all \mathbf{k} and then taking the thermodynamic limit $L \rightarrow \infty$ depend sensitively on the spatial dimension d . The variance

of $\bar{\rho}$ is finite in all dimensions,

$$\Delta_{\bar{\rho}} = \begin{cases} \pi/a & d = 1, \\ \ln(1 + (\Lambda/a)^2) & d = 2, \\ \text{finite} & d = 3, \end{cases} \quad (3.60)$$

while the variance of $\tilde{\phi}$ diverges in 1 and 2 dimensions and is finite in higher dimensions,

$$\Delta_{\tilde{\phi}} = \begin{cases} L & d = 1, \\ \ln L & d = 2, \\ \text{finite} & d = 3. \end{cases} \quad (3.61)$$

Thus in higher dimensions $d > 2$, the occasional excursions from the controlled state as a result of the noise do not lead to the instability of the targeted state. In lower dimensions however the noise fluctuations are large enough to destabilise the targeted state.

The reader may notice a close analogy between the modes $\bar{\rho}$ and $\tilde{\phi}$ and the massive and Goldstone fluctuations in the equilibrium ordered phase of the chiral-XY model. Fluctuations in ϕ are massless (Goldstone) arising from the spontaneously broken $O(2)$ symmetry corresponding to rotations in the plane perpendicular to the helical axis in the order parameter manifold.

3.5 Conclusions and Future Work

In this chapter we have studied the interplay between dissipation, inertia and an anisotropic driving on the dynamics of a Heisenberg magnet in d -dimensions. As in the single-particle example in Chapter 1, the asymptotic configurations exhibit a rich variety of non-equilibrium phases as a function of the drive-temperature T_{drive} [15, 16]. The system exhibits a ‘paramagnetic steady state’ at high T_{drive} and a ‘critical steady state’ at $T_{drive} = T_{drive}^c$, with power-law correlations induced by the driving even when the equilibrium Heisenberg magnet (without the driving) is paramagnetic. The drive takes the system away from the Wilson-Fisher fixed point leading to a new drive induced universality class. At low drive-temperatures both the homogeneous and inhomogeneous steady states are unstable. In particular, the system has an infinity of spatially periodic unstable steady states which are helical. We have provided numerical ‘proof’ (at least in $d = 1$) that the dynamics at low T_{drive} is spatio-temporally

chaotic. We would like to do a similar analysis for higher dimensions in the future. Several questions regarding this spatio-temporal chaos remain unanswered, such as the existence and nature of a low dimensional attractor. We have found that the spatio-temporal chaos may be ‘controlled’ to target any desired helical steady state. This control works even in the presence of noise in dimensions $d > 2$. We have yet to explore the entire set of parameters, *e.g.* the different values of r_{\perp} and r_{\parallel} , and so we exhibit the non-equilibrium phase diagram in the restricted space of parameters that we have studied, Fig. (3.9). Our work has explored the asymptotic states of spins subject to an external driving that breaks reflection symmetry. In future we would like to study the effect of an external drive which may break other space-time symmetries.

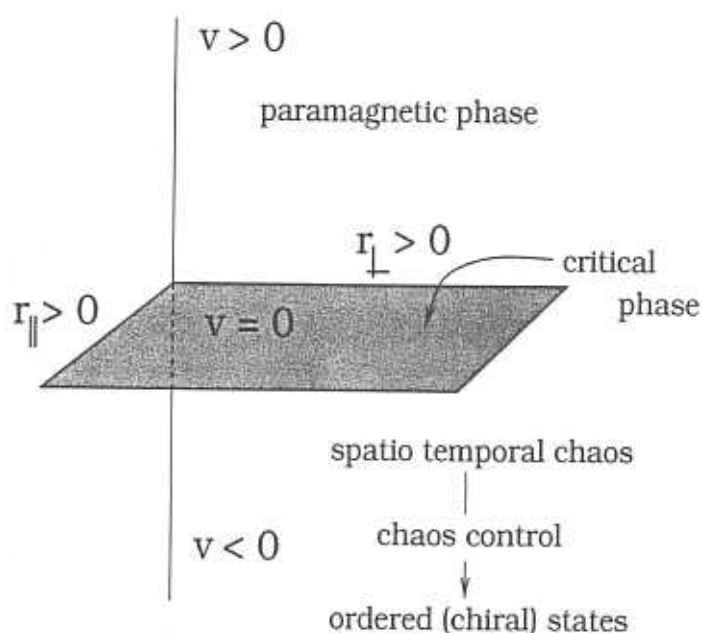


Figure 3.9: Non-equilibrium phase diagram as a function of the drive temperature T_{drive} .

3.6 Appendix IIIA

In this Appendix we present the details of perturbative calculation mentioned in Sect. 1.3. The diagrams corresponding to the lowest order terms in the perturbation expansion are constructed following the rules shown in Fig. 3.10.

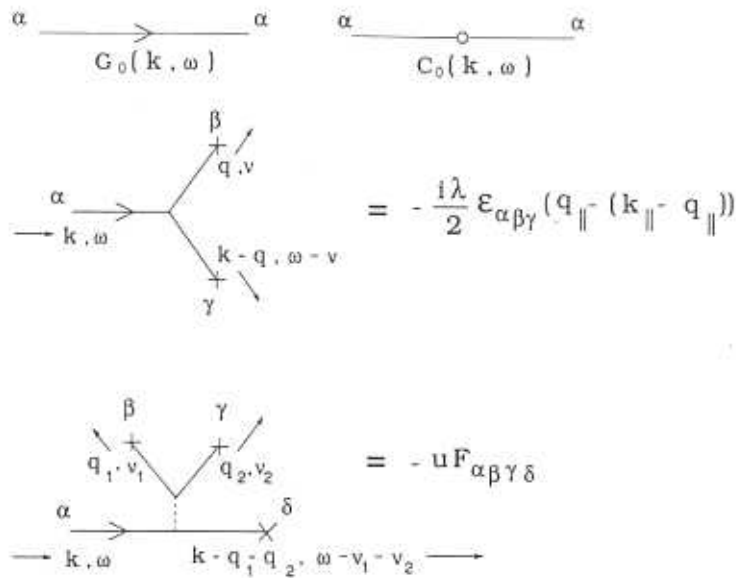


Figure 3.10: Graphs for correlation functions and vertices at the tree level. $F_{\alpha\beta\gamma\delta} = (1/3)[\delta_{\alpha\beta}\delta_{\gamma\delta} + \delta_{\alpha\delta}\delta_{\beta\gamma} + \delta_{\alpha\gamma}\delta_{\beta\delta}]$.

Corrections to $G_0(\mathbf{k}, \omega)$

(I) Corrections from the λ vertex :

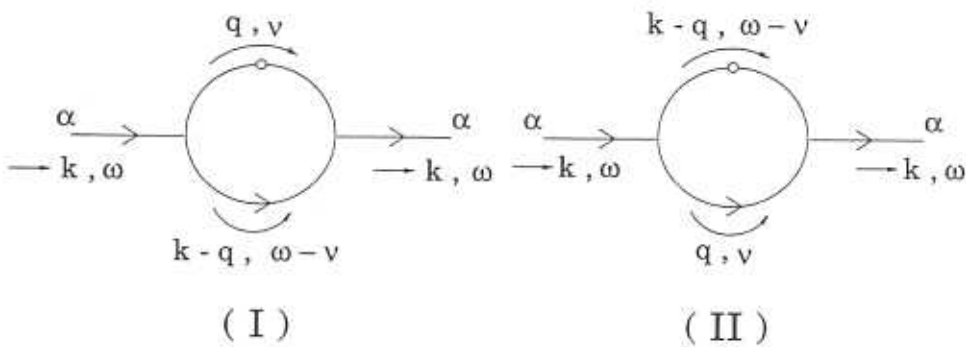


Figure 3.11: $O(\lambda^2)$ corrections to $G_0(\mathbf{k}, \omega)$.

Graphs (I) and (II) in Fig. 3.11 show the one-loop corrections to $G_0(\mathbf{k}, \omega)$ due to the λ vertex.

$$\Sigma_\lambda(\mathbf{k}, \omega) = -\frac{\lambda^2}{4} \int d\mathbf{q} d\nu \left[(q_\parallel - (k_\parallel - q_\parallel))(k_\parallel - (-q_\parallel)) G_0(\mathbf{k} - \mathbf{q}, \omega - \nu) C_0(\mathbf{q}, \nu) \right]$$

$$\begin{aligned}
& +((k_{\parallel} - q_{\parallel}) - q_{\parallel})(k_{\parallel} + (k_{\parallel} - q_{\parallel}))G_0(\mathbf{q}, \nu)C_0(\mathbf{k} - \mathbf{q}, \omega - \nu) \Big] \\
& = -\frac{2\lambda^2 B}{4} \int d\mathbf{q} \left[\frac{(2q_{\parallel} - k_{\parallel})(k_{\parallel} + q_{\parallel})}{\gamma^2(\mathbf{q})} + \frac{(k_{\parallel} - 2q_{\parallel})(2q_{\parallel} - q_{\parallel})}{\gamma^2(\mathbf{k} - \mathbf{q})} \right] \frac{1}{\gamma^2(\mathbf{q}) + \gamma^2(\mathbf{k} - \mathbf{q})}. \quad (3.62)
\end{aligned}$$

(in the limit $\omega \rightarrow 0$)

In the above integrals $\gamma^n(\mathbf{k})$ is defined as

$$\gamma^n(\mathbf{k}) = \left(\frac{1}{r_{\parallel} k_{\parallel}^2 + r_{\perp} k_{\perp}^2 - v} \right)^n.$$

We expand $\Sigma_{\lambda}(\mathbf{k}, 0)$ in powers of k_{\parallel} and k_{\perp} . Terms which are higher order than $O(k_{\parallel}^2)$ or $O(k_{\perp}^2)$ are ultraviolet convergent. Coefficients of the terms of order k^0 , k_{\parallel}^2 and k_{\perp}^2 denote changes to v , r_{\parallel} and r_{\perp} respectively.

(i) Term proportional to k^0

This part of $\Sigma_{\lambda}(\mathbf{k}, 0)$ does not have any infrared divergences but has divergences in the ultraviolet. We introduce an upper momentum cutoff Λ to get an estimate of the correction to v . We will denote the self energy contribution coming from the λ vertex to order k^0 as $(\Sigma_0)_{\lambda}$,

$$\begin{aligned}
(\Sigma_0)_{\lambda} &= -\frac{\lambda^2 B}{2} \int d\mathbf{q} \frac{q_{\parallel}^2}{\gamma^4(\mathbf{q})} \\
&= -\frac{\pi \Lambda^2 B}{4 r_{\parallel}^{3/2} r_{\perp}^{1/2}}. \quad (3.63)
\end{aligned}$$

(ii) Term proportional to k_{\parallel}^2

$$\begin{aligned}
(\Sigma_{\parallel})_{\lambda} &= -\frac{\lambda^2 B k_{\parallel}^2}{4} \int d\mathbf{q} \left[\frac{1}{2\gamma^4(\mathbf{q})} + \frac{16r_{\parallel}^2 q_{\parallel}^4}{\gamma^8(\mathbf{q})} - \frac{4r_{\parallel} q_{\parallel}^2}{\gamma^6(\mathbf{q})} \right] \\
&= \frac{\lambda^2 B v^{\epsilon/2} r_{\parallel} k_{\parallel}^2}{8\pi^2 \epsilon (r_{\parallel} r_{\perp})^{3/2}}, \quad (3.64)
\end{aligned}$$

where the integrals,

$$\int d\mathbf{q} \frac{1}{\gamma^4(\mathbf{q})} = \frac{r_{\parallel} v^{-\epsilon/2}}{8\pi^2 (r_{\parallel} r_{\perp})^{3/2}} \frac{1}{\epsilon}, \quad (3.65)$$

$$\int d\mathbf{q} \frac{q_{\parallel}^2}{\gamma^6(\mathbf{q})} = \frac{v^{-\epsilon/2}}{32\pi^2 (r_{\parallel} r_{\perp})^{3/2}} \frac{1}{\epsilon}, \quad (3.66)$$

$$\int d\mathbf{q} \frac{q_{\parallel}^4}{\gamma^8(\mathbf{q})} = \frac{r_{\parallel} v^{-\epsilon/2}}{64\pi^2 (r_{\parallel}^{5/2} r_{\perp}^{3/2})} \frac{1}{\epsilon}, \quad (3.67)$$

have been evaluated using the standard integrals for the general form $\int d\mathbf{q} (q_{\parallel}^a q_{\perp}^b) / \gamma^c(\mathbf{q})$ given in Ref. [8]. We have also had to make use of the asymptotic expansion for the Gamma function $\Gamma(-n + \epsilon)$, when n is zero or any positive integer and $\epsilon \rightarrow 0$,

$$\Gamma(-n + \epsilon) = \frac{(-1)^n}{n!} \left[\frac{1}{\epsilon} + \left(1 + \frac{1}{2} + \dots + \frac{1}{n} - \gamma \right) + O(\epsilon) \right], \quad (3.68)$$

where γ is the Euler-Maschieroni constant [17].

(iii) Term proportional to k_{\perp}^2

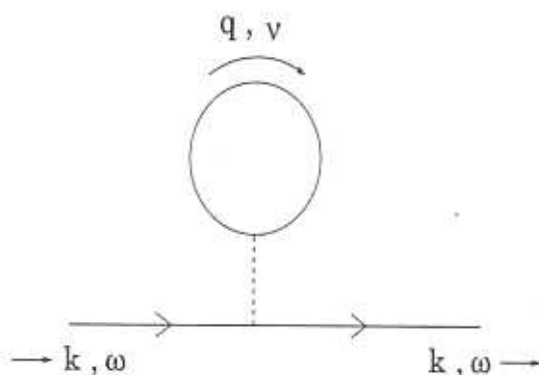
$$\begin{aligned} (\Sigma_{\perp})_{\lambda} &= -\frac{\lambda^2 B k_{\perp}^2}{4} \int d\mathbf{q} q_{\parallel}^2 \left[\frac{16 r_{\perp} q_{\perp}}{\gamma^8(\mathbf{q})} - \frac{4 r_{\perp}}{\gamma^6(\mathbf{q})} \right] \\ &= -\frac{5\lambda^2 B r_{\perp} k_{\perp}^2 v^{-\epsilon/2}}{96\pi^2 r_{\perp} (r_{\parallel} r_{\perp})^{3/2}} \frac{1}{\epsilon}, \end{aligned} \quad (3.69)$$

where we have evaluated the integral

$$\int d\mathbf{q} \frac{q_{\parallel}^2 q_{\perp}^2}{\gamma^8(\mathbf{q})} = \frac{v^{-\epsilon/2}}{48\pi^2 r_{\perp} (r_{\parallel} r_{\perp})^{3/2}} \frac{1}{\epsilon}. \quad (3.70)$$

(II) Corrections from the u - vertex :

There is also a correction to the response function $G(\mathbf{k}, \omega)$ coming from the u - vertex; to $O(\epsilon)$ this is shown in the figure below.

Figure 3.12: $O(u^2)$ corrections to the $\mathbf{k} = 0$ part of $G_0(\mathbf{k}, \omega)$.

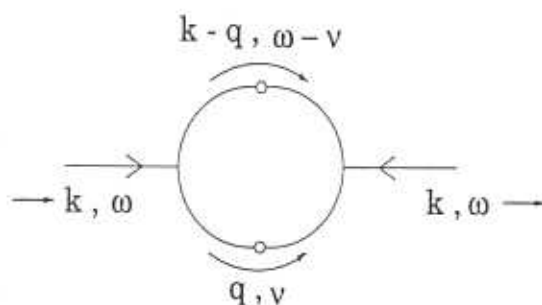
To 1-loop, the correction to $G(\mathbf{k}, \omega)$ from this interaction comes only from the $\mathbf{k} = 0$ piece given by,

$$\begin{aligned}
 (\Sigma_0)_u &= -\frac{5u}{3} \int d\mathbf{q} d\nu \nu C_0(\mathbf{q}, \nu) \\
 &= -\frac{5uB}{3} \int d\mathbf{q} \frac{1}{\gamma^2(\mathbf{q})} \\
 &= -\frac{5\pi\Lambda uB}{6r_{\parallel}^{1/2} r_{\perp}^{3/2}}.
 \end{aligned} \tag{3.71}$$

The net 1-loop correction to the response function G adds up to

$$\Sigma(\mathbf{k}, \omega) = [(\Sigma_0)_{\lambda} + (\Sigma_0)_u] + (\Sigma_{\parallel})_{\lambda} k_{\parallel}^2 + (\Sigma_{\perp})_{\lambda} k_{\perp}^2. \tag{3.72}$$

Corrections to $C_0(\mathbf{k}, \omega)$

Figure 3.13: $O(\lambda^2)$ corrections to $C_0(\mathbf{k}, \omega)$.

$$\begin{aligned}
\Sigma_B &= -\frac{\lambda^2}{4} \int \tilde{d}q \tilde{d}\nu ((k_{\parallel} - q_{\parallel}) - q_{\parallel})(q_{\parallel} - (k_{\parallel} - q_{\parallel})) C_0(\mathbf{k} - \mathbf{q}, \omega - \nu) C_0(\mathbf{q}, \nu) \\
&= \lambda^2 B^2 \int \tilde{d}q \frac{q_{\parallel}^2}{\gamma^6(\mathbf{q})} \\
&= \frac{\lambda^2 B^2 v^{-\epsilon/2}}{32\pi^2 (r_{\parallel} r_{\perp})^{3/2}} \frac{1}{\epsilon}.
\end{aligned} \tag{3.73}$$

The renormalised couplings are obtained from the vertex corrections to λ and u .

Corrections to the λ - vertex

The corrections to λ come from the three-point correlators,

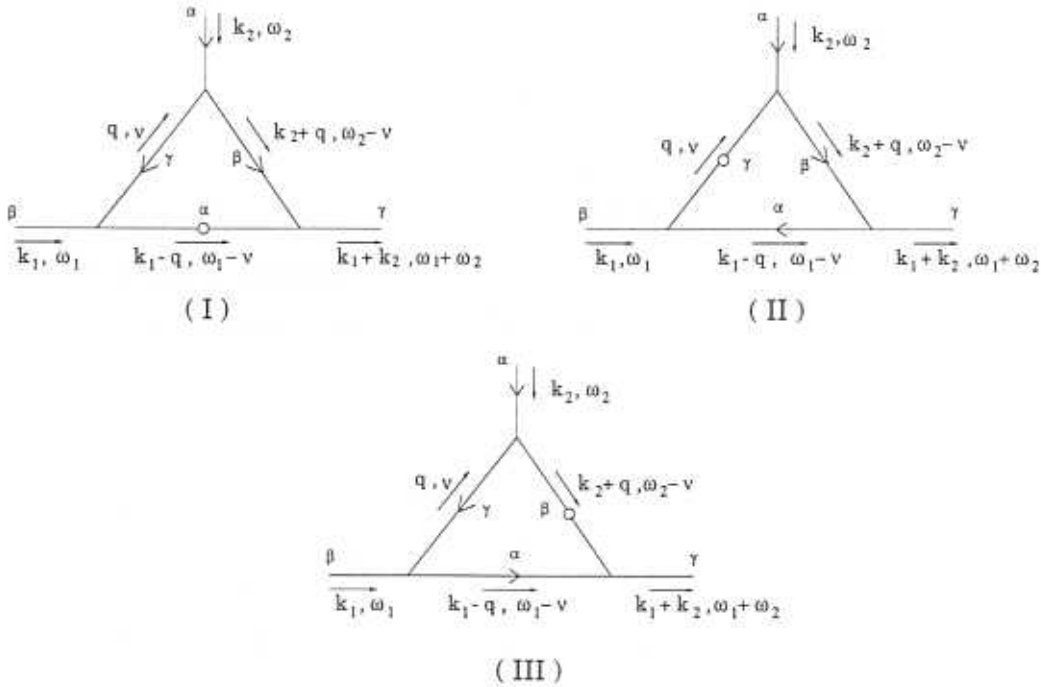


Figure 3.14: $O(\lambda^3)$ correction to the λ - vertex.

The contribution from (I) to the vertex function Γ_λ is given by,

$$\begin{aligned}
&\left(\frac{-i\lambda}{2}\right)^3 \int \tilde{d}q \tilde{d}\nu \left[((k_{1\parallel} - q_{\parallel}) + k_{1\parallel}) ((k_{2\parallel} + q_{\parallel}) + q_{\parallel}) ((k_{1\parallel} + k_{2\parallel}) + (k_{1\parallel} - q_{\parallel})) \right] \times \\
&G_0(\mathbf{q}, \nu) G_0(\mathbf{k}_2 + \mathbf{q}, \omega_2 - \nu) C_0(\mathbf{k}_1 - \mathbf{q}, \omega_1 - \nu) \\
&= \frac{i\lambda^3 B}{16} \int \tilde{d}q \frac{(8k_{1\parallel} + k_{2\parallel}) q_{\parallel}^2}{\gamma^6(\mathbf{q})}.
\end{aligned} \tag{3.74}$$

Likewise the contribution from (II) to Γ_λ is

$$\begin{aligned} & \left(\frac{-i\lambda}{2} \right)^3 \int \tilde{d}q \tilde{d}\nu \left[(-k_{1\parallel} - q_{\parallel})((k_{2\parallel} + q_{\parallel}) + q_{\parallel})((k_{1\parallel} + k_{2\parallel}) + (k_{1\parallel} - q_{\parallel})) \right] \times \\ & G_0(\mathbf{k}_1 - \mathbf{q}, \omega_1 - \nu) G_0(\mathbf{k}_2 + \mathbf{q}, \omega_2 - \nu) C_0(\mathbf{q}, \nu) \\ & = -\frac{i\lambda^3 B}{32} \int \tilde{d}q \frac{(2k_{1\parallel} + k_{2\parallel})q_{\parallel}^2}{\gamma^6(\mathbf{q})}, \end{aligned} \quad (3.75)$$

while (III) gives,

$$\begin{aligned} & \left(\frac{-i\lambda}{2} \right)^3 \int \tilde{d}q \tilde{d}\nu \left[-(k_{2\parallel} + q_{\parallel}) - (k_{1\parallel} + k_{2\parallel})((k_{2\parallel} + q_{\parallel}) + q_{\parallel})((k_{1\parallel} - q_{\parallel}) + k_{1\parallel}) \right] \times \\ & G_0(\mathbf{q}, \nu) G_0(\mathbf{k}_1 - \mathbf{q}, \omega_1 + \nu) C_0(\mathbf{k}_2 + \mathbf{q}, \omega_1 + \nu) \\ & = -\frac{i\lambda^3 B}{32} \int \tilde{d}q \frac{(2k_{1\parallel} - 5k_{2\parallel})q_{\parallel}^2}{\gamma^6(\mathbf{q})}. \end{aligned} \quad (3.76)$$

The three contributions combine to give,

$$\begin{aligned} \Gamma_\lambda(2k_{1\parallel} + k_{2\parallel}) &= \frac{3i\lambda^3 B}{16} \int \tilde{d}q \frac{q_{\parallel}^2(2k_{1\parallel} + k_{2\parallel})}{\gamma^6(\mathbf{q})} \\ &= \frac{3i\lambda^3 B(2k_{1\parallel} + k_{2\parallel})v^{-\epsilon/2}}{512\pi^2(r_{\parallel}r_{\perp})^{3/2}} \frac{1}{\epsilon}. \end{aligned} \quad (3.77)$$

Corrections to the u -vertex

There are two contributions to the vertex function Γ_u to $O(u^2)$ and $O(\lambda^4)$.

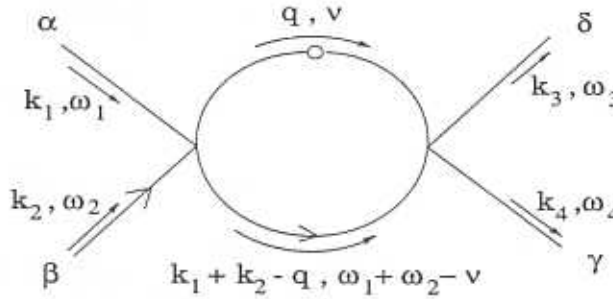
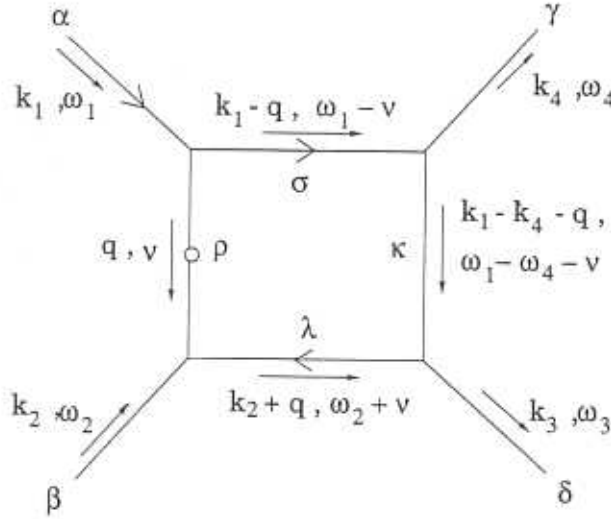


Figure 3.15: $O(u^2)$ correction to the u -vertex.

The $O(u^2)$ graph gives

$$\begin{aligned} & F_{\alpha\beta\gamma\delta} \frac{11u^2}{9} \int \tilde{d}q \tilde{d}\nu C_0(\mathbf{q}, \nu) G_0(\mathbf{k}_1 + \mathbf{k}_2 - \mathbf{q}, \omega_1 + \omega_2 - \nu) \\ & = F_{\alpha\beta\gamma\delta} \frac{11u^2 B}{18} \int \tilde{d}q \frac{1}{\gamma^4(\mathbf{q})} \\ & = F_{\alpha\beta\gamma\delta} \frac{11u^2 B}{48\pi^2 r_{\perp}^{3/2} r_{\parallel}^{1/2}} \frac{1}{\epsilon}. \end{aligned} \quad (3.78)$$

Figure 3.16: $O(\lambda^4)$ correction to the u -vertex.

The $O(\lambda^4)$ graph gives the following contribution :

$$\begin{aligned}
 & -1152 F_{\alpha\beta\gamma\delta} \left(\frac{\lambda}{4} \right)^4 \int d\mathbf{q} d\nu \nu ((k_{1\parallel} - q_{\parallel}) - q_{\parallel})(k_{4\parallel} - (k_{1\parallel} - k_{4\parallel} - q_{\parallel}))(k_{3\parallel} - (k_{2\parallel} + q_{\parallel}))(k_{2\parallel} + q_{\parallel}) \times \\
 & G_0(\mathbf{k}_1 - \mathbf{q}, \omega - \nu) G_0(\mathbf{k}_1 - \mathbf{k}_4 - \mathbf{q}, \omega_1 - \omega_2 - \nu) G_0(\mathbf{k}_2 + \mathbf{q}, \omega_2 + \nu) C_0(\mathbf{q}, \nu) \\
 & -1152 F_{\alpha\beta\gamma\delta} \left(\frac{3\lambda^4 B}{4^3} \right) \int d\mathbf{q} \frac{q_{\parallel}^2}{\gamma^8(\mathbf{q})} \\
 & = -F_{\alpha\beta\gamma\delta} \frac{27\lambda^4}{32\pi^2 r_{\perp}^{3/2} r_{\parallel}^{1/2} \epsilon}.
 \end{aligned} \tag{3.79}$$

The net correction to the u -vertex is,

$$\begin{aligned}
 \Gamma_u &= F_{\alpha\beta\gamma\delta} \frac{11u^2 B}{48\pi^2 r_{\perp}^{3/2} r_{\parallel}^{1/2}} \frac{1}{\epsilon} - F_{\alpha\beta\gamma\delta} \frac{27\lambda^4}{32\pi^2 r_{\perp}^{3/2} r_{\parallel}^{1/2} \epsilon} \\
 &= F_{\alpha\beta\gamma\delta} (r_{\parallel}^{1/2} r_{\perp}^{3/2}) \left[\frac{11\pi^4 \kappa^2}{12B\epsilon} - \frac{27\pi^4 \tau^2}{8B\epsilon} \right],
 \end{aligned} \tag{3.80}$$

where κ and τ are defined by

$$\kappa = \frac{uB}{2\pi^3 (r_{\parallel}^{1/2} r_{\perp}^{3/2})}, \tag{3.81}$$

$$\tau = \frac{\lambda B}{2\pi^3 (r_{\parallel}^{3/2} r_{\perp}^{3/2})}. \tag{3.82}$$

3.7 Appendix IIIB

In this Appendix we derive the results for the correlators given in Eq. (3.59). Consider small fluctuations $\tilde{\rho}(\mathbf{x}, t)$ and $\tilde{\phi}(\mathbf{x}, t)$ over the helical steady state $\rho(\mathbf{x}, t) = a$ and $\phi(\mathbf{x}, t) = px_{\parallel} + c$ respectively. To $O(\tilde{\rho})$ and $O(\tilde{\phi})$ the time evolution of the fluctuations is given by the linearised version of Eq. (3.53) about the helical state,

$$\begin{aligned}\frac{\partial \tilde{\rho}}{\partial t} &= \nabla^2 \tilde{\rho} - 2a^2 \tilde{\rho} - (2ap + \lambda ab) \partial_{\parallel} \tilde{\phi} + \eta_{\rho}, \\ \frac{\partial \tilde{\phi}}{\partial t} &= \nabla^2 \tilde{\phi} + \frac{1}{a} (2p + \lambda b) \partial_{\parallel} \tilde{\rho} + \eta_{\phi},\end{aligned}\quad (3.83)$$

where $\eta_{\rho}(\mathbf{x}, t) = \eta_1(\mathbf{x}, t) \cos(px_{\parallel}) + \eta_2(\mathbf{x}, t) \sin(px_{\parallel})$ and $\eta_{\phi}(\mathbf{x}, t) = a^{-1}[\eta_2(\mathbf{x}, t) \cos(px_{\parallel}) - \eta_1(\mathbf{x}, t) \sin(px_{\parallel})]$. The noises $\eta_{\rho}(\mathbf{k}, t)$ and $\eta_{\phi}(\mathbf{k}, t)$ satisfy

$$\begin{aligned}\langle \eta_{\rho}(\mathbf{k}, t) \eta_{\rho}(\mathbf{k}', t') \rangle &= 2B \delta_{\mathbf{k}, -\mathbf{k}'} \delta(t - t'), \\ \langle \eta_{\phi}(\mathbf{k}, t) \eta_{\phi}(\mathbf{k}', t') \rangle &= \frac{2B}{a^2} \delta_{\mathbf{k}, -\mathbf{k}'} \delta(t - t'), \\ \langle \eta_{\rho}(\mathbf{k}, t) \eta_{\phi}(\mathbf{k}', t') \rangle &= 0.\end{aligned}\quad (3.84)$$

We use the following definition of the Fourier transforms

$$\begin{aligned}\tilde{\rho}_{\mathbf{k}}(\omega) &= \int d\mathbf{k} d\omega \tilde{\rho}(\mathbf{x}, t) e^{-i\mathbf{k} \cdot \mathbf{x}} e^{i\omega t} \\ \tilde{\phi}_{\mathbf{k}}(\omega) &= \int d\mathbf{k} d\omega \tilde{\phi}(\mathbf{x}, t) e^{-i\mathbf{k} \cdot \mathbf{x}} e^{i\omega t}\end{aligned}\quad (3.85)$$

to solve Eq. (3.83) for $\rho_{\mathbf{k}}$ and $\phi_{\mathbf{k}}$,

$$\begin{aligned}\tilde{\rho}_{\mathbf{k}}(\omega) &= \frac{1}{D(\mathbf{k}, \omega)} (\eta_{\rho}(\mathbf{k}, \omega) (i\omega + k^2) - i\eta_{\phi}(\mathbf{k}, \omega) k_{\parallel} a (2p + \lambda b)), \\ \tilde{\phi}_{\mathbf{k}}(\omega) &= \frac{1}{D(\mathbf{k}, \omega)} (\eta_{\phi}(\mathbf{k}, \omega) (i\omega + k^2 + 2a^2) - \frac{i}{a} \eta_{\rho}(\mathbf{k}, \omega) k_{\parallel} (2p + \lambda b)),\end{aligned}\quad (3.86)$$

where

$$D(\mathbf{k}, \omega) = -\omega^2 + 2i\omega(k^2 + a^2) + k^2(k^2 + 2a^2) - k_{\parallel}^2(2p + \lambda b)^2. \quad (3.87)$$

We now compute the equal time correlation functions $C_{\tilde{\rho}}$ and $C_{\tilde{\phi}}$ averaged over the noise:

$$\begin{aligned}C_{\tilde{\rho}}(\mathbf{k}) &= \langle \tilde{\rho}_{\mathbf{k}}(t) \tilde{\rho}_{-\mathbf{k}}(t) \rangle = \int d\omega \langle \tilde{\rho}_{\mathbf{k}}(\omega) \tilde{\rho}_{-\mathbf{k}}(-\omega) \rangle \\ &= B \frac{k^4 + k_{\parallel}^2 a^2 (2p + \lambda b)^2}{2ff_{-}(f_{+} + f_{-})} + \frac{B}{2(f_{+} + f_{-})}\end{aligned}\quad (3.88)$$

where f_+ and f_- are the roots of the equation $D(\mathbf{k}, \omega) = 0$,

$$f_{\pm} = k^2 + a^2 \pm \left[a^4 + k_{\parallel}^2 (2p + \lambda b)^2 \right]^{1/2}. \quad (3.89)$$

and

$$\begin{aligned} C_{\tilde{\phi}}(\mathbf{k}) &= \langle \tilde{\phi}_{\mathbf{k}}(t) \tilde{\phi}_{-\mathbf{k}}(t) \rangle = \int d\omega \langle \tilde{\phi}_{\mathbf{k}}(\omega) \tilde{\phi}_{-\mathbf{k}}(-\omega) \rangle \\ &= \frac{B}{a^2} \frac{k^2 + 2a^2 + k_{\parallel}^2 (2p + \lambda b)^2}{2f_+ f_- (f_+ + f_-)} + \frac{B}{2a^2} \frac{1}{f_+ + f_-}. \end{aligned} \quad (3.90)$$

We use the $k \rightarrow 0$ behaviour to evaluate the variances $\Delta_{\tilde{\rho}}$ and $\Delta_{\tilde{\phi}}$. In this infrared limit

$$C_{\tilde{\rho}} \sim \frac{B}{k^2 + a^2}, \quad (3.91)$$

and

$$C_{\tilde{\phi}}(\mathbf{k}) \sim \frac{B}{k_{\perp}^2 + k_{\parallel}^2 \left(1 - \left(\frac{2p + \lambda b}{2a} \right)^2 \right)}. \quad (3.92)$$

Bibliography

- [1] N. G. Van Kampen in *Stochastic Processes in Physics and Chemistry* (North Holland Physics Publishing, Amsterdam, 1985).
- [2] R. Stinchcombe, Oxford Univ. Preprint, OUTP-96-26S.
- [3] B. Schmittmann and R. K. P. Zia in *Phase Transitions and Critical Phenomena*, Vol. 17, eds. C. Domb and J. L. Lebowitz (Academic Press, NY, 1995).
- [4] H. C. Fogedby, Phys. Rev. E **57**, 2331 (1998).
- [5] T. Hwa, *Statistical Mechanics and Dynamics of Surfaces and Membranes*, Ph.D Thesis (Massachusetts Institute of Technology, 1990).
- [6] D. J. Amit in *Field Theory, the Renormalisation Group, and Critical Phenomena* (McGraw-Hill International Book Company, NY, 1978).
- [7] E. Brezin, J. C. Le Guillon and Zinn-Justin in *Phase Transitions and Critical Phenomena*, Vol. 6, eds. C. Domb and M. Green (Academic Press, NY, 1976).
- [8] G. 't Hooft and M. Veltman, Nuc. Phys. B **44**, 189 (1972) ; M. Veltmann in *Diagrammatics : The Path to Feynmann Rules* (Cambridge University Press, Cambridge, 1994).
- [9] That these are the only possible asymptotic behaviours is discussed in S. Wolfram, Rev. Mod. Phys. **55**, 601 (1984), in the context of cellular automata models.
- [10] W. H. Press, S. A. Teukolsky, W. T. Vetterling and B. P. Flannery in *Numerical Recipes in Fortran*, 2nd ed. (Cambridge University Press, Cambridge, 1992).

- [11] M. C. Cross and P. C. Hohenberg, *Rev. Mod. Phys.* **65**, 851 (1993).
- [12] T. Shinbrot, C. Grebogi, E. Ott and J. A. Yorke, *Nature* **363**, 411 (1993).
- [13] T. Shinbrot, *Adv. Phys.* **44**, 73 (1995).
- [14] P. M. Chaikin and T. C. Lubensky in *Principles of Condensed Matter Physics* (Cambridge University Press, Cambridge, 1995).
- [15] J. Das, M. Rao and S. Ramaswamy, in preparation.
- [16] J. Das, M. Rao and S. Ramaswamy, in preparation.
- [17] M. Abramovitz and I. A. Stegun in *Handbook of Mathematical Functions* (Dover, NY, 1970).

Chapter 4

Dynamics of Heisenberg magnets driven by a Temperature gradient

In this last chapter we study the dynamics of Heisenberg spins where the effects of inertia, driving and *boundary dissipation* compete with each other to give rise to new steady states. We apply two heat sources at the boundary which are simultaneously sources of noise and dissipation. Furthermore, the boundaries either allow for a spin current to flow across (*non-conserved model*) or disallow a spin current (*conserved model*). For the most part, we restrict our study to the conserved model in $d = 1$ (Sect. 4.2). In last section we touch upon the non-conserved model leaving a detailed investigation for the future. Details of our calculations are presented in Appendix IVA.

4.1 Model of Heat Conduction

Consider a system of Heisenberg spins placed between two heat baths (1 and 2) kept at temperatures T_1 and T_2 (let $T_1 > T_2$) respectively, separated by a distance L (Fig. 4.1). The spins are arranged on a d -dimensional regular hypercubic lattice with fixed sites labelled by $\{\mathbf{r}\}$. The microscopic Hamiltonian is short-ranged and is given by

$$E = -2J \sum_{\mathbf{r}, \mathbf{a}} \mathbf{S}_{\mathbf{r}} \cdot \mathbf{S}_{\mathbf{r}+\mathbf{a}}, \quad (4.1)$$

where $J > 0$ (ferromagnetic) and $\{\mathbf{a}\}$ are the primitive vectors.

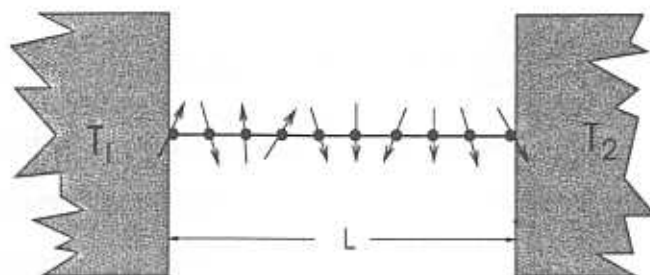


Figure 4.1: Schematic picture of a system of Heisenberg spins in $d = 1$ placed in between heat baths with temperatures T_1 and T_2 , where $T_1 > T_2$.

We will work with the *microscopic dynamics* for the bulk spins, since one of the contentious issues in this field is the existence of local thermodynamic equilibrium (LTE) [1]. The existence of LTE implies that the system can be divided into small d -dimensional cells $\{\Sigma(\mathbf{x})\}$ (where $\{\mathbf{x}\}$ labels the centres of the boxes), each one large enough to be treated as a macroscopic thermodynamic subsystem but much smaller than the system size, so that intensive thermodynamic variables such as pressure $P(\mathbf{x})$, temperature $T(\mathbf{x})$ and magnetisation $\mathbf{m}(\mathbf{x})$ do not change within the cell and have the same relation to each other as in equilibrium [2]. It appears that in most one dimensional microscopic models of heat conduction investigated so far, LTE does not exist [1, 3, 4]. This in particular would imply that we cannot write down continuum hydrodynamic equations for the heat flow [5].

As in the earlier chapters, the microscopic equation of motion in the bulk is given by the energy conserving (inertial) dynamics,

$$\frac{\partial \mathbf{S}_r}{\partial t} = \mathbf{S}_r \times \mathbf{h}_r, \quad (4.2)$$

where $\mathbf{h}_r = -J \sum_{\mathbf{a}} (\mathbf{S}_{r+\mathbf{a}} + \mathbf{S}_{r-\mathbf{a}})$ is the local magnetic field experienced by the bulk spins. The boundary spins in addition interact with the heat bath and so the full dynamics of the boundary spins is reversible precession and boundary dissipation. At the boundaries (denoted as 1 and 2) the spins are in local thermal equilibrium with their adjoining heat baths. We are therefore justified in using a coarse-grained continuum description for the dynamics of the boundary spins. The time evolution of the boundary spins may be written

as,

$$\frac{\partial \mathbf{S}_{b1,2}}{\partial t} = -\Gamma_{1,2} \frac{\delta F}{\delta \mathbf{S}_{b1,2}} + \Omega_L \mathbf{S}_{b1,2} \times \frac{\delta F}{\delta \mathbf{S}_{b1,2}} + \vec{\mu}_{1,2} + \vec{\eta}_{1,2} \quad (4.3)$$

where $F[\mathbf{S}_b]$ is the continuum Landau-Ginzburg free-energy functional (Eq. (1.3)). The first term is the boundary dissipation with $\Gamma_{1,2}$ being the kinetic coefficients. The boundary noises $\vec{\eta}_{1,2}$ have zero mean and correlator,

$$\langle \eta_{\alpha(1,2)}(\mathbf{x}, t) \eta_{\beta(1,2)}(\mathbf{x}', t') \rangle = 2\Gamma_{(1,2)} k_B T_{(1,2)} \delta_{\alpha\beta} \delta^d(\mathbf{x} - \mathbf{x}') \delta(t - t'), \quad (4.4)$$

and obeys the boundary FDT. The second term in Eq. (4.3) is the inertial precession dynamics. Clearly if $T_1 > T_2$, an 'energy current' or 'heat flux' will flow in the system proportional to the gradient of the temperature. The boundary chemical potentials $\vec{\mu}_1$ and $\vec{\mu}_2$ are conjugate to the boundary spins. If $\vec{\mu}_1 > \vec{\mu}_2$, a 'spin current' or 'spin flux' will be set up proportional to the gradient in the chemical potential. The heat flow dynamics in the absence of a spin current ($\vec{\mu}_1 = \vec{\mu}_2$) will be called the *conserved model*, while the dynamics in the presence of spin current ($\vec{\mu}_1 \neq \vec{\mu}_2$) will be called the *nonconserved model*. Since we work in a fixed particle ensemble, there will be no particle current.

The forms of the energy and spin current in the bulk can be determined from the time evolution described in Eq. (4.2). In the bulk the local energy density is given by

$$\epsilon(\mathbf{x}, t) = \sum_{\mathbf{r}} \epsilon_{\mathbf{r}} \delta^d(\mathbf{x} - \mathbf{r}), \quad (4.5)$$

where

$$\epsilon_{\mathbf{r}} = \frac{J}{2} \sum_{\mathbf{a}} \left[(\mathbf{S}_{\mathbf{r}+\mathbf{a}} - \mathbf{S}_{\mathbf{r}})^2 + (\mathbf{S}_{\mathbf{r}-\mathbf{a}} - \mathbf{S}_{\mathbf{r}})^2 \right] \quad (4.6)$$

The energy density $\epsilon(\mathbf{x}, t)$ obeys a continuity equation,

$$\frac{\partial \epsilon(\mathbf{x}, t)}{\partial t} + \nabla \cdot \mathbf{J}^{\epsilon}(\mathbf{x}, t) = 0. \quad (4.7)$$

The heat current is defined as $\mathbf{J}^{\epsilon}(\mathbf{x}, t) = \sum_{\mathbf{r}} \mathbf{j}_{\mathbf{r}}^{\epsilon} \delta^d(\mathbf{x} - \mathbf{r})$, where $\mathbf{j}_{\mathbf{r}}^{\epsilon}$ takes the form (derived in Appendix IVA)

$$\mathbf{j}_{\mathbf{r}}^{\epsilon} = 2Ja(\mathbf{S}_{\mathbf{r}} \times \mathbf{S}_{\mathbf{r}-\mathbf{a}}) \cdot \mathbf{S}_{\mathbf{r}+\mathbf{a}}. \quad (4.8)$$

One can define a macroscopic current density $\langle \mathbf{J}^e(\mathbf{x}, t) \rangle$ within each cell $\Sigma(\mathbf{x})$, where $\langle \cdot \cdot \cdot \rangle$ indicates an average over the distribution of states, which in the presence of LTE corresponds to an average over the equilibrium ensemble in that cell. When LTE exists one may define a local temperature $T(\mathbf{x}, t)$ which bears the same relation to the local energy density $\langle \epsilon(\mathbf{x}, t) \rangle$ as the canonical temperature to the average energy density at equilibrium. This latter relation, known exactly for the Heisenberg model in $d = 1$ [6], is given by

$$\langle \epsilon(\mathbf{x}) \rangle = 2(J - (\coth(J/k_B T) - k_B T/J)). \quad (4.9)$$

In higher dimensions where such a relation is not known exactly, one may obtain the relation between the local energy density and the local temperature through a numerical simulation. The thermal conductivity $\kappa(T(\mathbf{x}, t))$ is defined through a constitutive relation (Fourier's law)[7],

$$\langle \mathbf{J}^e(\mathbf{x}, t) \rangle = -\kappa(T) \nabla T(\mathbf{x}, t). \quad (4.10)$$

The constitutive relation (Eq. 4.10) with the help of Eq. (4.7) gives Fourier's equation (Eq.(1.14)) of heat conduction. In real physical systems $\kappa(T)$ is a finite quantity with a well defined thermodynamic limit. This implies that J^e scales as $1/L$ (using Eq. (4.10)), where L is the size of the system.

The local spin density in the bulk, $m_\alpha(\mathbf{x}, t) = \sum_{\mathbf{r}} S_{\alpha\mathbf{r}} \delta(\mathbf{x} - \mathbf{r})$, also obeys a continuity equation

$$\frac{\partial m_\alpha}{\partial t} + \nabla \cdot \mathbf{J}_\alpha^S = 0, \quad (4.11)$$

with a spin current defined as $\mathbf{J}_\alpha^S(\mathbf{x}, t) = \sum_{\mathbf{r}} \mathbf{j}_{\alpha\mathbf{r}}^S \delta^d(\mathbf{x} - \mathbf{r})$. The form of $\mathbf{j}_{\mathbf{r}}^S$ may be shown to be (see Appendix IVA)

$$\mathbf{j}_{\alpha\mathbf{r}}^S = 2\mathbf{a} J \epsilon_{\alpha\beta\gamma} (S_{\beta\mathbf{r}+\mathbf{a}} - S_{\beta\mathbf{r}-\mathbf{a}}) S_{\gamma\mathbf{r}}. \quad (4.12)$$

As before we may define a spin conductivity κ_S through a constitutive relation

$$\langle \mathbf{J}_\alpha^S(\mathbf{x}, t) \rangle = -\kappa_S \nabla \mu_\alpha, \quad (4.13)$$

under the assumption of LTE. If LTE exists, the local vector chemical potential μ_α in a cell $\Sigma(\mathbf{x})$ can be calculated by exploiting the relation between μ_α and the magnetisation $\langle m_\alpha \rangle$

at equilibrium (the latter may be either determined analytically or numerically). As in the thermal conductivity case, finiteness of κ_S in the thermodynamic limit implies that J^S scales as $1/L$.

Now we proceed to study the dynamics of heat conduction in the conserved model (no spin current in the bulk at steady state) of Heisenberg spins in $d = 1$.

4.2 Conserved Dynamics, $\vec{\mu}_1 = \vec{\mu}_2$

The heat baths 1 and 2 are constructed from Heisenberg spins which are in equilibrium at temperatures T_1 and T_2 respectively. At $t = 0$ the spins (both in the bulk and in the heat baths) are taken from a uniform distribution with zero mean and uncorrelated in space. Inside the heat baths the time evolution of the spins is obtained by solving the dissipative Eq. (4.3) (written, for convenience, in dimensionless form by scaling x , t , η_α and S_α appropriately, see Sect. 2.1),

$$\frac{\partial \mathbf{S}_{b1,2}}{\partial t} = \nabla^2 \mathbf{S}_{b1,2} - \text{sgn}(r) \mathbf{S}_{b1,2} - (\mathbf{S}_{b1,2} \cdot \mathbf{S}_{b1,2}) \mathbf{S}_{b1,2} + g (\mathbf{S}_{b1,2} \times \nabla^2 \mathbf{S}_{b1,2}) + \sqrt{\alpha_{1,2}} \vec{\eta}_{1,2}, \quad (4.14)$$

with the noise correlator

$$\langle \eta_{\alpha 1,2}(\mathbf{x}, t) \eta_{\beta 1,2}(\mathbf{x}', t') \rangle = \delta_{\alpha\beta} \delta(\mathbf{x} - \mathbf{x}') \delta(t - t'), \quad (4.15)$$

using an Euler scheme (Sect. 2.1.1) on a regular 1D lattice. The noise strength $\alpha_{1,2}$ (Eq. 4.14) is chosen appropriate to the bath temperatures $T_{1,2}$. The size of the bath is taken to be much smaller (of the order of a few bulk correlation lengths $\xi(T)$) than the size of the bulk system, so as to ensure that the spins in the heat bath equilibrate within the simulation time. In the bulk the spins evolve according to Eq. (4.2) which we solve numerically using the scheme described in Sect. 3.4. After the spins reach a steady state we calculate the following quantities — (i) energy density $\langle \epsilon_i \rangle$, (ii) energy current $\langle \mathbf{j}_i^e \rangle$, and (iii) equal-time correlation function $C_i(r) = \langle \mathbf{S}_{i+r} \cdot \mathbf{S}_i \rangle$, where $\langle \cdots \rangle$ indicates a time average in the steady state and an average over initial configurations. Note that since spatial translation invariance is explicitly broken when $T_1 \neq T_2$, the equal time correlation function between points i and $i + r$ depends on both the relative separation r and the ‘centre-of-mass’ coordinate.

4.2.1 Dynamics in one dimension

Our numerical simulations are done on a $d = 1$ regular lattice with the bulk size ranging from $N = 20$ to $N = 80$ (the lattice spacing a has been chosen to be 1). The size of the heat bath is taken to be 10. For our Euler discretisation we take $\Delta x = 1$ and $\Delta t = 0.0005$. These parameter values do not give rise to any instability in the numerical simulation and our results are unchanged on slight variations of Δx and Δt . All quantities are measured in units of Δx and Δt . The energy scale J is taken to be equal to 0.2 in all our simulations.

(A) Case $T_1 = T_2$

The heat baths (1 and 2) are kept at equal temperatures, $T_1 = T_2 \equiv T$. One might expect this boundary condition to eventually lead to thermal equilibrium at a temperature T . We study this dynamics at two different values of the heat bath temperature ($T = T_l$ (low temperature) corresponding to a heat bath noise strength $\alpha_l = 0.1$ ($\sim 0.5J$ when $J = 0.2$) and $T = T_h$ (high temperature) which corresponds to $\alpha_h = 5 \sim 25J$). By monitoring the total energy density $E/N = N^{-1} \sum_i \epsilon_i$, we have ensured that the system reaches a steady state after time $t_s \sim 10^7$ (Fig. (4.2)).

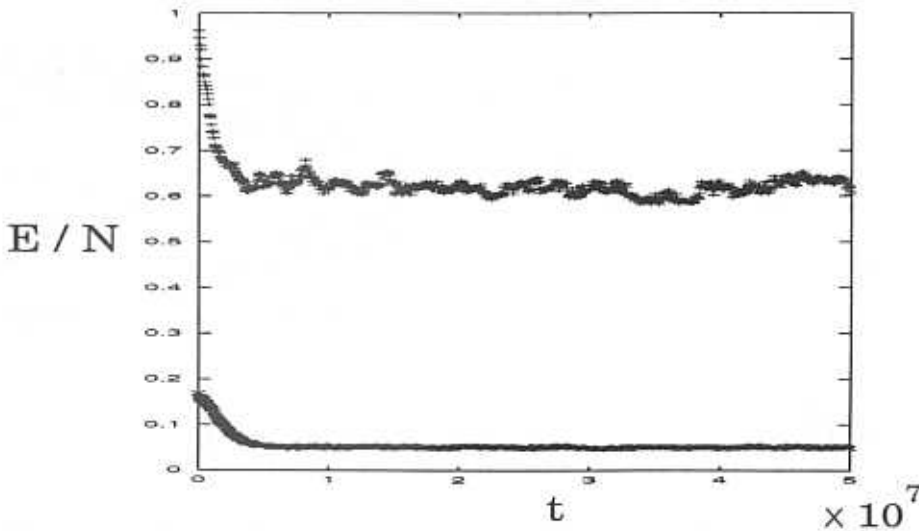


Figure 4.2: Plot of E/N vs time t when $N = 40$ for temperatures $T_l(\times)$ and $T_h(+)$. A steady state is obtained at times $t > 6 \times 10^6$.

To study the nature of the steady state we first check for local thermal equilibrium. At equilibrium the form of the correlation function $C(r) = \langle \mathbf{S}_{i+r}(t) \cdot \mathbf{S}_i(t) \rangle$ is known exactly [6],

$$C(r) = u(T)^r = C(1)^r = e^{r \ln(u(T))}, \quad (4.16)$$

where $u(T) = \coth(J/k_B T) - k_B T/J$ is the form of the equilibrium energy density. If LTE were to exist such a relation should hold locally when coarse-grained over a cell $\Sigma(\mathbf{x})$. We compute the correlation function $C_i(r)$ within a cell of size $r \leq 3$ centered at $i + 3/2$. All quantities are averaged over a time interval of 10^6 in the steady state region and further averaged over 20 uncorrelated initial configurations.

Figure (4.3a) shows plots of $C_i(1)$, $C_i(2)$ and $C_i(3)$ versus i in the steady state when the bath temperatures are set at $T = T_l$ (low temperature). This clearly shows a violation of Eq. (4.16), and we conclude that at these low bath temperatures local thermal equilibrium does not hold (indeed global thermal equilibrium also does not hold) ! However when the bath temperatures are raised to $T = T_h \gg T_l$, we find that the correlators obey Eq. (4.16) locally (Fig. (4.3a)), suggesting that LTE exists at higher bath temperatures.

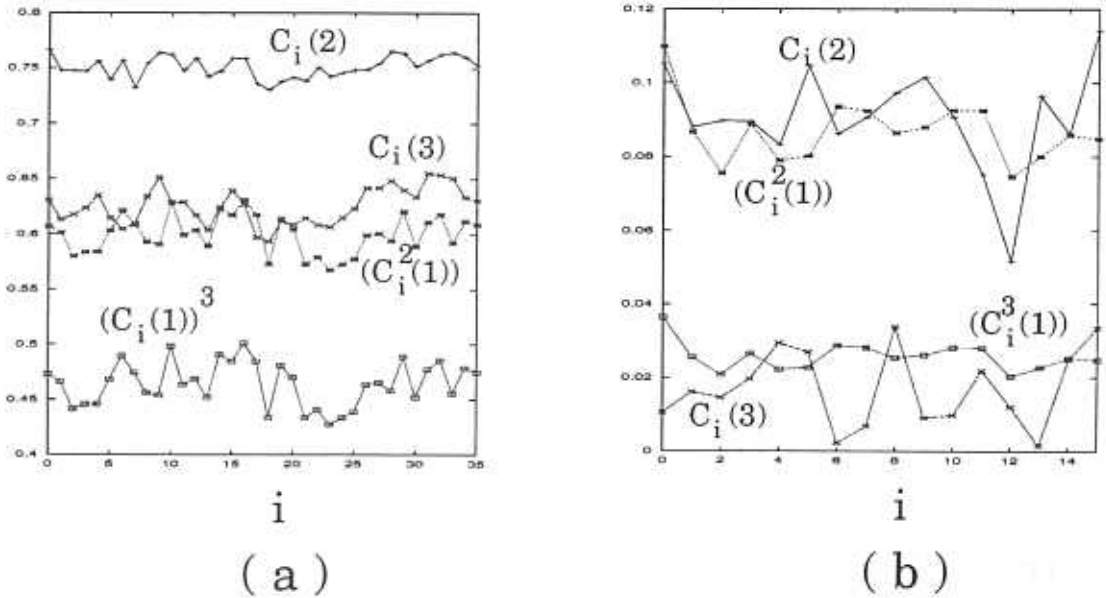


Figure 4.3: Plot of $C_i(2)(+)$, $C_i(3)(\times)$ vs i for $N = 40$. (a) A comparison of $C_i(2)$, $C_i(3)$ with $(C_i(1))^2(*)$ and $(C_i(1))^3(\square)$ shows that Eq. (4.16) does not hold in the bulk, implying the absence of LTE at low temperatures T_l . (b) A similar comparison at high temperatures T_h , shows that Eq. (4.16) is obeyed locally, suggesting the existence of LTE.

We offer a tentative understanding of our numerical findings. The dynamics Eq. (4.2) in $d = 1$ (in the absence of any heat baths) admits soliton solutions [8] and possesses an infinite number of conserved quantities [9] apart from the total energy. This extensive number of conserved quantities breaks up the constant energy surface into distinct sectors each labelled by the values that these conserved quantities take. The conservation laws prevent the system from moving from one sector to another — the motion is therefore not ergodic. Introducing the boundary heat bath as a source of dissipation and noise breaks these conservation laws. One might imagine that this would allow the system to ‘tunnel’ from one sector to another, thereby restoring ergodicity and equilibrium. The time required to reach equilibrium would in general depend on (a) the boundary temperature T and (b) the system size N . At high temperatures T_h , the boundary dissipation is large, the breakdown of conservation laws is strong, and the system approaches equilibrium in a reasonable time. At low temperatures T_l the breakdown of the conservation laws is weaker, and the system does not reach equilibrium in any reasonable time. An intriguing possibility is that this finite temperature ergodicity breaking is a true transition in the thermodynamic limit, but a lot more work is needed to establish this claim. This scenario is very similar to the behaviour of the Fermi-Pasta-Ulam (FPU) system [10] which exhibits ergodicity and approach to equilibrium if the energy density is above a threshold $\epsilon_c(N) \sim 1/N^2$, while it shows trapping (apparent breakdown of ergodicity) below this threshold [11].

(B) Case $T_1 > T_2$

In this case the difference in temperatures of the boundary heat baths drives a thermal current across the bulk. We study the system for two sets of (T_1, T_2) , related to the strength of the noise correlators at the baths — Set (i) : low temperatures ($\alpha_1 = 1, \alpha_2 = 0.1$) and Set (ii) : high temperatures ($\alpha_1 = 5, \alpha_2 = 2$). We check for both the existence of LTE and the validity of Fourier’s law.

We will see that LTE is violated at low temperatures (Set (i)), making it meaningless to define a local temperature. LTE is however restored at high temperatures (Set (ii)). This is

what one might have expected based on our analysis of the (earlier) Case (A). This implies that at high temperatures we may define a local temperature field and hence a thermal conductivity. We have not done a systematic study of the scale dependence of the thermal conductivity to check the validity of Fourier's law, but we hope to do this in the future. A similar scenario was shown to occur in a lattice model of rigid rotors in $d = 1$, where normal heat transport was restored above a threshold temperature [12].

We again monitor the time dependence of the total energy density E/N to ensure that the system approaches a steady state. We find an approach to the steady state for times $t > 5 \times 10^6$ (Fig. (4.4)) when the temperatures are low (Set(i)). In the steady state all physical quantities are averaged over a time interval of 10^6 in addition to being averaged over 20 uncorrelated initial configurations.

As before we test for LTE by computing 2-point correlators $C_i(r)$ coarse-grained over a cell of size r centered at $i + 3/2$. For our computations we have chosen $r = 3$; plots of $C_i(1)$, $C_i(2)$ and $C_i(3)$ versus i (Fig. (4.5)) for low temperatures (Set (i)) clearly show that they do not obey Eq. (4.16) suggesting that LTE does not exist.

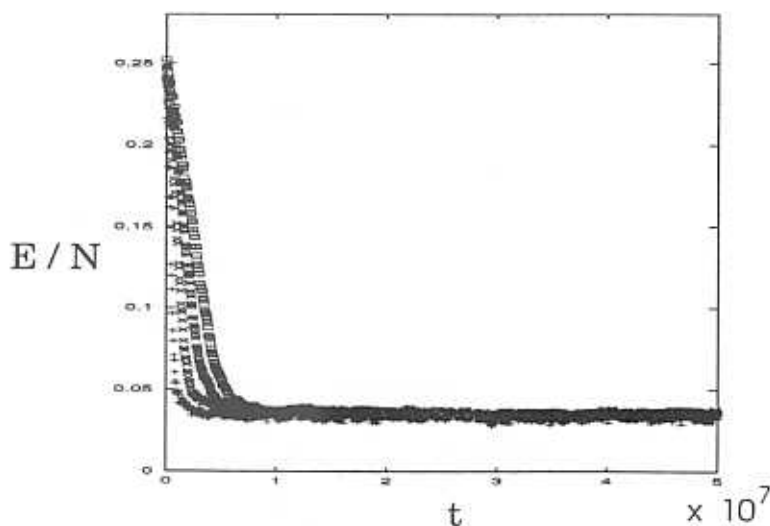


Figure 4.4: Time dependence of total energy for $L = 20(+)$, $40(\times)$, $60(*)$ and $80(\square)$ for low temperatures. This shows that the system enters a steady state after times $t > 5 \times 10^6$.

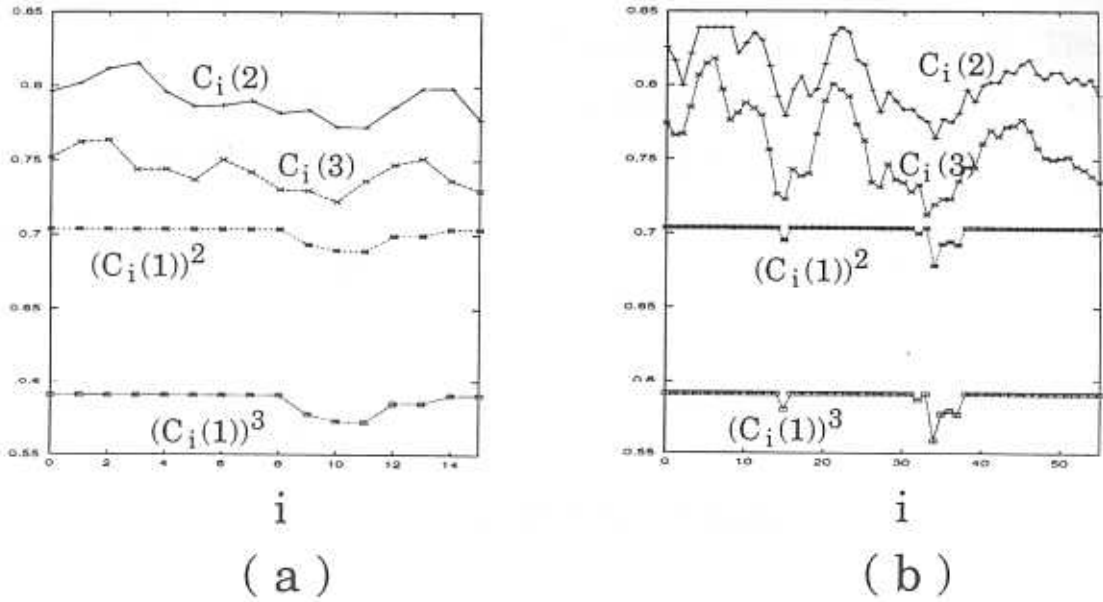


Figure 4.5: (a) Plot of $C_i(2)(+)$, $C_i(3)(\times)$ vs i for $N = 20$ at low temperatures. A comparison of $C_i(2)$, $C_i(3)$ with $(C_i(1))^2(*)$ and $(C_i(1))^3(\square)$ shows that Eq. (4.16) does not hold in the bulk, implying the absence of LTE. (b) Same as (a) for $N = 60$.

Since local equilibrium is absent at low temperatures, one cannot define a local temperature field; we therefore study the local energy density profile $\langle \epsilon_i(t) \rangle$ in the bulk at steady state. The energy density (Fig. (4.6)), changes exponentially fast from its value at the boundaries (equal to the corresponding bath temperature) to a constant, uniform profile in the bulk. The length scale over which the energy density changes is around 4 bulk lattice spacings in our simulations and depends on the size of the system (larger the system size, steeper is the change) and the temperature of the adjacent heat bath. The energy density profile in the bulk does not seem to have an appreciable system size dependence.

The scaling of the corresponding energy current J^ϵ with system size N is shown in Fig. (4.7); the scale independence of the energy current implies (as discussed in Sect. 1.3) that the thermal conductivity diverges as N .

Divergent heat conductivity (scaling as N^α) and a flat energy density profile with a discontinuous jump near the boundaries characterise the anomalous heat transport of a few 1D model systems such as a system of hard spheres and a linear chain of simple harmonic oscillators [4, 1]. In both these examples, the uniform profile of the energy density in the

bulk is due to the presence of localised non-interacting modes in the system. These non-interacting modes do not allow for a transfer of energy in the bulk, resulting in a uniform energy density profile and hence a divergent heat conductivity.

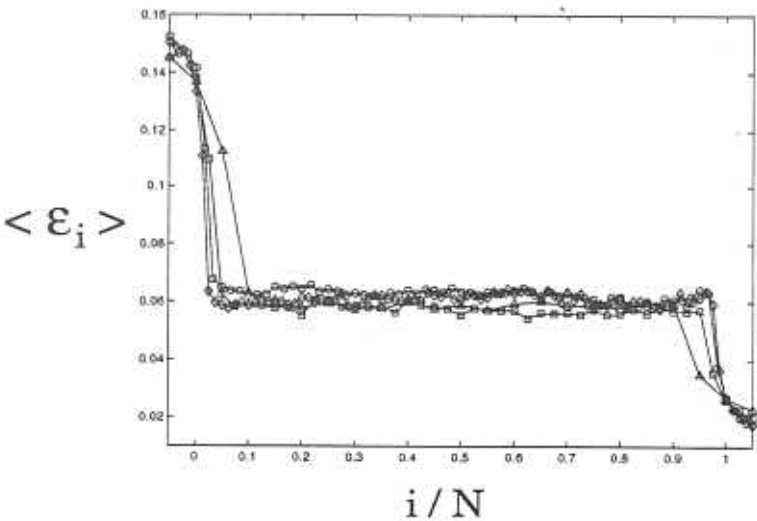


Figure 4.6: Plot energy density for $N = 20(\triangle)$, $40(\square)$, $60(\circ)$ and $80(\diamond)$ with respect to i/N for low temperatures. The bulk profile does not scale with i/N and after a rapid exponential change near the boundaries (becoming steeper with N) attains a uniform value.

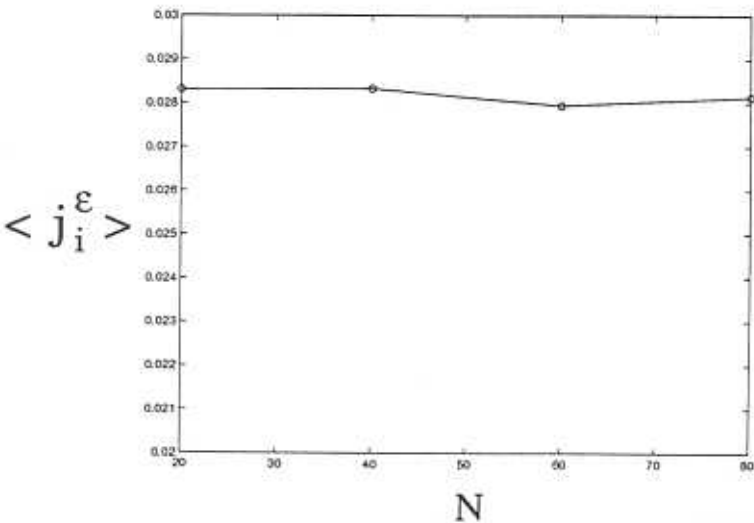


Figure 4.7: Scale independence of the energy current. A plot for $N = 20, 40, 60$ and 80 shows that it is almost constant (≈ 0.0285), implying a divergent heat conductivity $\kappa \sim N$.

At higher temperatures (Set (ii)), LTE is restored as can be seen from Fig. (4.8), where the steady state values of $C_i(1)$, $C_i(2)$ and $C_i(3)$ are related by Eq. (4.16). This implies that LTE exists at higher temperatures, allowing us to define a local temperature field.

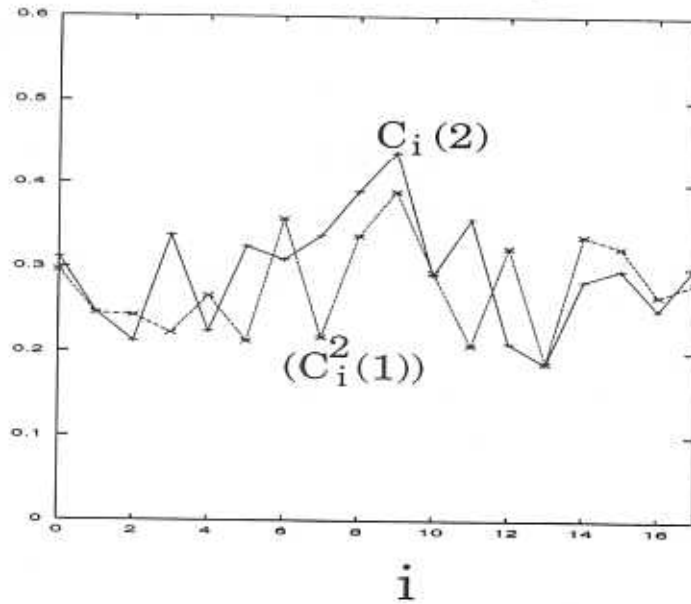


Figure 4.8: (a) Plot of $C_i(2)(+)$, $C_i(3)(\times)$ vs i for $N = 20$. A comparison of $C_i(2)$, $C_i(3)$ with $(C_i(1))^2(*)$ and $(C_i(1))^3(\square)$ shows that Eq. (4.16) holds in the bulk, implying the existence of LTE. The statistics may be improved by averaging over more configurations.

We have not been able to compute the scale dependence of the thermal conductivity, since this requires a lot more averaging. We hope to do this in future.

4.3 Conclusions and Future Work

We end this short chapter with our conclusions and suggestions for future work. We have studied the microscopic dynamics of the Heisenberg spins driven by a boundary temperature gradient. Our numerical calculations have been restricted to $d = 1$. We have defined two distinct models – a *conserved model*, which does not allow for a bulk spin current and *nonconserved model* which allows for a bulk spin current. In each of these models we ask for (i) the existence of LTE, and (ii) the validity of Fourier's law.

In the *conserved model* we find that LTE does not hold at low temperatures. The thermal conductivity measured by the ratio of the current to the energy density scales linearly with system size showing that Fourier's law is invalid. At high temperatures LTE is restored. We speculate on a finite temperature ergodicity breaking transition; but more extensive work is needed to establish this.

To study the *nonconserved model*, we may impose a chemical potential gradient across the boundaries. This results in the presence of both an energy current and a spin current which interact with each other. It is likely that the associated conductivities are related, analogous to the Weidmann-Franz law [13], which relates the thermal conductivity to the electrical conductivity. Another intriguing possibility is the emergence of Self Organised Criticality (SOC) in the steady state. The boundary effects may provide a source of a nonconserved noise to the spin conserving dynamics in the bulk (Eq. (4.2)), resulting in power-law spin correlations [14]. These effects will be analysed in the near future.

4.4 Appendix IVA

Here we derive the forms for the energy and spin currents given in Eq.(4.8) and Eq. (4.12) respectively. The Fourier transforms of $\epsilon(\mathbf{x}, t)$ and $\mathbf{m}(\mathbf{x}, t)$ are defined as

$$\epsilon_{\mathbf{k}}(t) = \int d^d x \epsilon(\mathbf{x}, t) e^{-i\mathbf{k} \cdot \mathbf{x}}, \quad (4.17)$$

and

$$\mathbf{m}_{\mathbf{k}}(t) = \int d^d x \mathbf{m}(\mathbf{x}, t) e^{-i\mathbf{k} \cdot \mathbf{x}}. \quad (4.18)$$

Taking the Fourier transforms of Eq. (4.7) we get

$$\begin{aligned} & \frac{\partial \epsilon_{\mathbf{k}}(t)}{\partial t} + i\mathbf{k} \cdot \mathbf{J}_{\mathbf{k}}^{\epsilon} = 0 \\ \Rightarrow & \sum_{\mathbf{r}} \left(\frac{\partial \mathbf{S}_{\mathbf{r}}}{\partial t} \cdot \mathbf{h}_{\mathbf{r}} + \mathbf{S}_{\mathbf{r}} \cdot \frac{\partial \mathbf{h}_{\mathbf{r}}}{\partial t} \right) e^{i\mathbf{k} \cdot \mathbf{r}} + i\mathbf{k} \mathbf{J}_{\mathbf{k}}^{\epsilon} = 0 \\ \Rightarrow & \sum_{\mathbf{r}, \mathbf{a}} \mathbf{S}_{\mathbf{r}} \cdot \left(\frac{\partial \mathbf{S}_{\mathbf{r}+\mathbf{a}}}{\partial t} + \frac{\partial \mathbf{S}_{\mathbf{r}-\mathbf{a}}}{\partial t} \right) e^{i\mathbf{k} \cdot \mathbf{r}} + i\mathbf{k} \mathbf{J}_{\mathbf{k}}^{\epsilon} = 0 \\ \Rightarrow & -J \sum_{\mathbf{r}, \mathbf{a}} \frac{\partial \mathbf{S}_{\mathbf{r}}}{\partial t} \cdot \left(\mathbf{S}_{\mathbf{r}+\mathbf{a}} e^{i\mathbf{k} \cdot (\mathbf{r}+\mathbf{a})} + \mathbf{S}_{\mathbf{r}-\mathbf{a}} e^{i\mathbf{k} \cdot (\mathbf{r}-\mathbf{a})} \right) + i\mathbf{k} \mathbf{J}_{\mathbf{k}}^{\epsilon} = 0 \\ \Rightarrow & -J \sum_{\mathbf{r}, \mathbf{a}} \left(\mathbf{S}_{\mathbf{r}} \times \mathbf{S}_{\mathbf{r}-\mathbf{a}} \right) \cdot \mathbf{S}_{\mathbf{r}+\mathbf{a}} e^{i\mathbf{k} \cdot \mathbf{r}} \left(e^{i\mathbf{k} \cdot \mathbf{a}} - e^{-i\mathbf{k} \cdot \mathbf{a}} \right) + i\mathbf{k} \mathbf{J}_{\mathbf{k}}^{\epsilon} = 0. \end{aligned} \quad (4.19)$$

In the long wave-length limit ($k \rightarrow 0$), to the lowest order in \mathbf{k} , we obtain Eq. (4.8), *viz.*,

$$\mathbf{j}_{\mathbf{r}}^{\epsilon} = 2Ja \left(\mathbf{S}_{\mathbf{r}} \times \mathbf{S}_{\mathbf{r}-\mathbf{a}} \right) \cdot \mathbf{S}_{\mathbf{r}+\mathbf{a}}. \quad (4.20)$$

Likewise, Fourier transforming the Eq. (4.11)

$$\begin{aligned} & \frac{\partial \mathbf{m}_{\mathbf{k}}(t)}{\partial t} + i\mathbf{k} \cdot \mathbf{J}_{\mathbf{k}}^S = 0 \\ \Rightarrow & -J \sum_{\mathbf{r}, \mathbf{a}} \mathbf{S}_{\mathbf{r}} \times \left(\mathbf{S}_{\mathbf{r}+\mathbf{a}} - \mathbf{S}_{\mathbf{r}-\mathbf{a}} \right) e^{i\mathbf{k} \cdot \mathbf{r}} \left(e^{i\mathbf{k} \cdot \mathbf{a}} - e^{-i\mathbf{k} \cdot \mathbf{a}} \right) + i\mathbf{k} \cdot \mathbf{J}_{\mathbf{k}}^S = 0. \end{aligned} \quad (4.21)$$

As before in the hydrodynamic limit we get Eq. (4.12).

Bibliography

- [1] F. Bonetto, J. L. Lebowitz and L. Rey-Bellet, math-ph/0002052 (2000).
- [2] H. J. Kreuzer in *Nonequilibrium Thermodynamics and its Statistical Foundations* (Clarendon Press, London, 1981).
- [3] A. Dhar and D. Dhar, Phys. Rev. Lett. **82**, 480 (1999).
- [4] Z. Reider, J. L. Lebowitz and E. Lieb, J. Math. Phys. **8**, 1073 (1967).
- [5] P. M. Chaikin and T. C. Lubensky in *Principles of Condensed Matter Physics* (Cambridge University Press, Cambridge, 1995).
- [6] C. J. Thompson in *Phase Transitions and Critical Phenomena*, eds. C. Domb and M. S. Green (Academic Press, London, 1972).
- [7] D. Forster in *Hydrodynamic Fluctuations, Broken Symmetry and Correlation Functions* (W. A. Benjamin Inc., London, 1975).
- [8] J. Tjon and J. Wright, Phys. Rev. B **15**, 3470 (1977).
- [9] H. C. Fogedby, J. Phys. A **13**, 1476 (1980).
- [10] E. Fermi, J. Pasta and S. Ulam, Los Alamos Report LA-1940 (1950) (unpublished) ; in *Collected Papers of Enrico Fermi*, ed. E. Segré, Vol. 2 (University of Chicago, Chicago, 1965).
- [11] L. Casetti, M. Cerruti-Sola, M. Pettini and E. G. D. Cohen, Phys. Rev. E **55**, 6566 (1997).

- [12] O. V. Gendelman and A. V. Savin, Phys. Rev. Lett. **84**, 2381 (2000).
- [13] N. W. Ashcroft and N. D. Mermin in *Solid State Physics* (Holt-Saunders International Ed., Philadelphia, 1981).
- [14] G. Grinstein, D. -H. Lee and S. Sachdev, Phys. Rev. Lett. **64**, 1927 (1990).